UNIVERSIDADE FEDERAL DO RIO DE JANEIRO

INSTITUTO DE FÍSICA

Optical Tweezers with structured light and applications

Arthur Luna da Fonseca

Tese de Doutorado apresentada ao Programa de Pós-Graduação em Física do Instituto de Física da Universidade Federal do Rio de Janeiro - UFRJ, como parte dos requisitos necessários à obtenção do título de Doutor em Ciências (Física).

Orientador: Paulo Américo Maia Neto

Coorientador: Nathan Bessa Viana

Rio de Janeiro

Abril de 2025

Optical Tweezers with structured light and applications

Arthur Luna da Fonseca

Orientador: Paulo Américo Maia Neto

Coorientador: Nathan Bessa Viana

Tese de Doutorado submetida ao Programa de Pós-Graduação em Física, Instituto de Física, da Universidade Federal do Rio de Janeiro – UFRJ, como parte dos requisitos necessários à obtenção do título de Doutor em Ciências (Física).

Aprovada por:

....

Prof. Dr. Paulo Américo Maia Neto, IF-UFRJ
(Presidente e Orientador)

....

Prof. Dr. Nathan Bessa Viana, IF-UFRJ
(Coorientador)

....

Prof. Dr. Felipe Arruda de Araújo Pinheiro, IF-UFRJ

....

Prof. Dr. Cláudio Lenz Cesar, IF-UFRJ

....

Prof. Dr. Antonio Zelaquett Khoury, UFF

....

Prof. Dr. Thiago Barbosa dos Santos Guerreiro, PUC-Rio

....

Prof. Dr. François Michel Claude Impens, IF-UFRJ

Rio de Janeiro, RJ - Brasil

Abril de 2025

Fonseca, Arthur Luna da
F676o Optical Tweezers with structured light and applications/ Arthur Luna da Fonseca. - - Rio de Janeiro, 2025.
126 f.

Orientador: Paulo Américo Maia Neto.
Coorientador: Nathan Bessa Viana.
Tese (doutorado) - Universidade Federal do Rio de Janeiro, Instituto de Física, Programa de Pós-Graduação em Física, 2025.

1. Optical Tweezers. 2. Structured light. 3. Optical angular momentum. 4. Brownian motion. 5. Optical chirality. I. Neto, Paulo Américo Maia, orient. II. Viana, Nathan Bessa, coorient. III. Título.

Resumo

Optical Tweezers with structured light and applications

Arthur Luna da Fonseca

Orientador: Paulo Américo Maia Neto

Coorientador: Nathan Bessa Viana

Resumo da Tese de Doutorado apresentada ao Programa de Pós-Graduação em Física do Instituto de Física da Universidade Federal do Rio de Janeiro - UFRJ, como parte dos requisitos necessários à obtenção do título de Doutor em Ciências (Física).

Essa tese é um trabalho sobre Pinças Ópticas com luz estruturada e suas aplicações em estudos sobre a dinâmica e as interações luz-matéria de partículas coloidais em nano e micro-escalas. Pinças ópticas são ferramentas de alto valor científico usadas para aprisionar partículas microscópicas e consistiam originalmente de um feixe laser fortemente focalizado que exerce uma força de gradiente em um objeto polarizável. Por esse motivo, pinças ópticas são chamadas alternativamente de armadilhas de força de gradiente com feixe único.

Luz estruturada é um termo genérico usado para designar feixes luminosos que carregam estruturas espaciais de fase e polarização. Nessa tese discutiremos as aplicações de feixes vórtices no estudo da dinâmica de partículas submetidas a um potencial óptico biestável e apresentaremos os resultados teóricos, experimentais e numéricos desse projeto. Feixes vórtice são campos de luz estruturada que carregam momento angular orbital, que é caracterizado por uma estrutura de fase helicoidal em torno do eixo óptico e que possui uma carga topológica associada. O potencial biestável que apresentaremos é uma configuração nova para sistemas de aprisionamento óptico usando feixes vórtice. Essa configuração biestável de aprisionamento foi inicialmente prevista por meio de análises numéricas e posteriormente confirmada experimentalmente.

Adicionalmente, apresentaremos nessa tese a teoria para forças ópticas de sistemas de aprisionamento usando feixes estruturados exóticos. Esses feixes são compostos por uma combinação de um par de modos vórtice com cargas topológicas e helicidade com sinais invertidos, o que resulta em um híbrido entre feixes vetorial cilíndrico (estrutura de polarização) e vórtice (estrutura de fase). Discutimos a aplicação desses feixes no estudo da interação entre luz quiral e matéria quiral, e apresentamos um proposta promissora de um sistema para separação enantiomérica de partículas Mie e dipolares, baseado unicamente em forças ópticas. O sistema proposto é baseado no controle independente, por meio de ajustes nos parâmetros experimentalmente acessíveis do feixe paraxial incidente, de diferentes graus de liberdade dos campos eletromagnéticos resultantes desses feixes híbridos ao serem fortemente focalizados.

Palavras-chave: Pinças Ópticas, Feixes Vórtice, Luz estruturada, óptica não-paraxial, Momento angular óptico, Interação spin-orbita, Movimento Browniano, Quiralidade óptica.

Abstract

Optical Tweezers with structured light and applications

Arthur Luna da Fonseca

Orientador: Paulo Américo Maia Neto

Coorientador: Nathan Bessa Viana

Abstract da Tese de Doutorado apresentada ao Programa de Pós-Graduação em Física do Instituto de Física da Universidade Federal do Rio de Janeiro - UFRJ, como parte dos requisitos necessários à obtenção do título de Doutor em Ciências (Física).

This thesis is a work about Optical Tweezers with structured light and their applications in the study of the dynamics and light-matter interactions of nano- and micro-scale colloidal particles. Optical Tweezers are invaluable scientific tools used to trap microscopic particles and originally consisted of a tightly focused laser beam exerting a gradient force on a polarizable object, hence the alternative name single-beam gradient force trap.

Structured light is a generic term for light beams carrying a spatial structure of phase and polarization. In this thesis, we discuss the applications of vortex beams to study the dynamics of a particle embedded in a bistable potential, presenting a project that involved theoretical, experimental, and numerical results. Vortex beams are structured light fields that carry orbital angular momentum, which is encoded in a helical phase structure characterized by a topological charge. The bistable potential we present is a novel configuration for optical trapping systems employing vortex beam modes, and was first obtained from a numerical analysis and later confirmed experimentally.

Additionally, we present the theory for optical forces using exotic beams composed of

a combination of vortex modes, which results in a hybrid cylindrical vector and vortex beam. We discuss its application to the study of chiral light-chiral matter interactions and present a promising proposal for optical enantioseparation of Mie or dipolar particles using vector beams. The proposal is based on the fact that tightly focusing this family of exotic modes allows us to independently control different degrees of freedom of the field distribution by tweaking the input paraxial beam parameters.

Keywords: Optical Tweezers, Vortex beams, Structured light, non-paraxial optics, Optical angular momentum, Spin-orbit interaction, Brownian motion, Optical chirality.

Agradecimentos

Essa tese de doutorado é o resultado de um esforço duradouro e coletivo, em que familiares, amigos e instituições contribuíram para que eu pudesse focar meus esforços e produzir os trabalhos científicos que serão apresentados a seguir. Por isso queria começar os agradecimentos mencionando meus familiares e amigos mais próximos. Agradeço aos meus pais, João Ricardo e Izamaria, ao meu irmão Henrique, à minha parceira Cássia Nascimento, aos meus avós Eucy, Eunice, Zildo e João Rafael, meus mais profundos agradecimentos pela criação, companhia e pelo amor. Aos meus queridos amigos, que muitas vezes considero como parte da minha família, Vinicius Henning, Kainã Diniz, Diney Ether, José Hugo Elsas e Guilherme Costa. Também agradeço aos amigos Vitor Costa, Felipe Affonso, Pedro Foster, Benjamin Spreng e Lucas Lima pela companhia, pelas conversas e por todos os ótimos cafés que compartilhamos tantas vezes.

Além disso, agradeço a todo o corpo docente, colegas e funcionários que participaram construtivamente da minha jornada de formação. Agradeço ao meu orientador Paulo Américo por toda a paciência, pelos ensinamentos, pela cooperação que vêm desde o fim da minha graduação e também (mais uma vez) por todos os inesquecíveis cafés que compartilhamos todos esses anos ao longo das nossas longas discussões. Ao meu coorientador Nathan Bessa pelo incentivo e apoio em desenvolver toda a parte de pesquisa experimental, que enriqueceu tanto minha formação quanto os resultados dos trabalhos da tese. Ao meu coorientador de mestrado Rafael Dutra, que continuou a colaborar ativamente tanto nos projetos do meu doutorado quanto diretamente na minha formação como pesquisador. Aos amigos e colegas do laboratório de pinças ópticas, em especial ao Guilherme Moura e ao Kainã (novamente) por todas as discussões e troca de conhecimentos. Agradeço também aos funcionários do Instituto de Física, em especial ao Igor de Souza e à Aninha, por toda ajuda e suporte prestados todos esses anos.

Quero agradecer também ao grupo de Interações Luz-Matéria em Sistemas Complexos no Instituto de Ciências e de Engenharia Supramolecular (ISIS, Institut de Sciences et d'Ingénierie Supramoléculaires), ligado a Universidade de Estrasburgo na França. Em especial ao Professor Cyriaque Genet por ter aceitado me receber para fazer meu doutorado sanduíche em seu grupo sob sua supervisão. Esses foram seis meses que nunca me esquecerei na minha vida. Agradeço também ao Luís Pires, que me recebeu em Estrasburgo e me ajudou tanto na adaptação à cidade quanto à rotina de pesquisa do grupo; ao Professor Thomas E., bem como aos seus alunos, pelo acolhimento e pelo apoio aos projetos em que me envolvi; e aos amigos Bruno Vidigal, Kelton, Bianca e Rémi pela companhia e pelos bons momentos que vivi ao longo desse período. Por último, agradeço à Coordenação de Aperfeiçoamento de Pessoal de Nível Superior (CAPES) por possibilitar essa experiência me fornecendo a bolsa CAPES-Print de doutorado sanduíche.

Finalmente, quero agradecer aos membros da banca por todos os comentários sobre a minha tese, que foram extremamente construtivos e estimulantes; e também ao Conselho Nacional de Desenvolvimento Científico e Tecnológico (CNPq) pelo financiamento da minha pesquisa por meio da bolsa de doutorado.

Contents

List of Figures

Chapter 1

Introduction

The development of Optical Tweezers dates back to 1969, when Arthur Ashkin (1922-2020) was conducting his initial work on the effect of radiation pressure from laser beams on microscopic objects. Over the next years, until around 1986, Ashkin and colleagues published seminal works about optical trapping of atoms and dielectric microscopic particles, as well as optical levitation of particles in high vacuum. His discoveries led to a series of revolutions in different scientific fields, beginning with the possibility of trapping biological particles (like cells and bacteria, for instance). Today, the technique has become quite popular, and in some cases even essential, in many other areas, such as nano-optics, plasmonics, and photonics, to name a few. The numerous possibilities that this wonderful invention—the optical tweezers—brought us led to Arthur Ashkin's award of the Nobel Prize in 2018.

Initially, the theoretical models for Optical Tweezers systems relied on approximations that limited the validity of the description for most systems. Typically, the approximations attempted to simplify the description of either the light scattering by the trapped object (*e.g.* by using the dipole approximation or the geometric optics limit) or the strongly focused beam by a microscope objective lens (*e.g.* by using paraxial optics). The first approximation-free model was proposed in 2000 by Professors Paulo Américo Maia Neto and Herch Moysés Nussenzveig. They used the Richards-Wolf model for the non-paraxial trapping beam and Mie scattering theory to describe the interaction between the beam and a trapped dielectric sphere, both of which are exact, *ab initio* robust theories. The model for optical forces was named Mie-Debye (MD), and it became a fundamental cornerstone for various theses within the Optical Tweezers Laboratory group (*Laboratório de Pinças Ópticas* in Portuguese, or simply LPO), founded by Professor Nussenzveig.

Indeed, modeling an Optical Tweezers system is not a trivial task. Artifacts such as optical aberrations, instabilities, and imperfections in the laser beam, particle samples, or even the optical system make it inefficient to compare theoretical models with experimental data. This fact raises the question of how useful an exact model for the optical force is in exploring or predicting the behaviors of such a complex physical system. A 2019 study from the LPO group demonstrated such utility by showing the emergence of negative torque in an optical tweezers experiment, which included a robust numerical analysis that corroborated the presence of this effect. My master's thesis project was based on this same system; however, we focused on characterizing the system's optical aberrations by performing nonlinear regression of the experimental data using only the Mie-Debye model, a technique that proved to be quite successful.

Over time, the LPO group produced extensions of the MD model for various cases, aiming to describe an increasingly broader range of Optical Tweezers systems. Among the projects addressed in this thesis is a new occurrence of a physical effect that we observe both in experiments and in numerical data derived from theory: bistability in Optical Tweezers with Vortex Beams. Furthermore, we also present a theoretical project that discusses a scheme for enantioselective optical manipulation and characterization of individual chiral particles using a family of exotic beams related to vortex modes. Both the topics of Vortex Beams and optical chirality were addressed by the group in other projects in which I participated, and they will also be presented and discussed despite being the subjects of theses by other group members.

Another application where Optical Tweezers are extremely useful is in the reproduction of stochastic systems. For example, in the bistability experiment, we observe the coexistence of two states with distinct stochastic dynamics. The first state corresponds to the usual case of a particle confined in 3 dimensions, while the second corresponds to a canonical example of a non-equilibrium steady state (NESS), where the particle is pushed along an orbit in which energy is constantly dissipated.

Finally, we will list the chapters and their contents. In Chapter 2, we will present some basic concepts and theories involved in a typical Optical Tweezers system. This chapter aims to serve as a foundation for understanding all subsequent chapters. Its content covers the description of the paraxial Vortex Beam, a brief presentation and discussion of the Richards-Wolf and MD models for a tightly focused Vortex Beam, and an introduction to the Langevin equation, which describes the Brownian dynamics of confined particles in optical traps. In Chapter 3, we discuss the optical bistability experiment in detail and perform a numerical analysis based on experimental parameters using MD theory. In Chapter 4, we present a theoretical model for optical forces using exotic beams, which result from combining a pair of Vortex Beams with opposite helicity (circular polarization) and topological charge states. We demonstrate that we can combine the two Vortex Beams with different relative amplitudes and phases to create a family of states with different properties and applications in the characterization and sorting of chiral particles. Appendix A discusses two projects in which I participated as a co-author. In the first project, the MD model for vortex beams is used to characterize experimental system parameters, particularly the radius of the trapped microsphere, through nonlinear regression of experimental optical torque angle data. In the second project, the MD model for vortex beams is again used to propose a method for measuring the chirality parameter of a microsphere. It was shown that the rotation period of a microsphere trapped in orbit in the Vortex Beam trap strongly depends on the chirality parameter of the microsphere material. Appendix B presents details of the MDSA force models that were omitted during the thesis. We discuss the derivation of the Debye potentials, used in the theory formulation, and present the MDSA theory expressions for three different optical trapping systems. Finally, Chapter 5 presents the final perspectives of the projects presented in the thesis and concludes the discussions we addressed in each chapter.

Chapter 2

Elemental theory topics on Optical Tweezers

We begin the content of this thesis by presenting the tools that will be used in all subsequent chapters. These tools include the Richards-Wolf model for the non-paraxial tightly-focused laser beam and the Mie-Debye spherical aberration theory for the optical force in optical tweezers. It also includes guidelines for the operation and stability characterization of an Optical Tweezers system using vortex beams, as well as an introduction to the Langevin equation, which describes the Brownian dynamics of the trapped colloidal particle.

The first topic in this chapter is the strongly focused field model, developed by Richards and Wolf [1], which we extend in order to account for a vortex beam at the input of an objective lens. Our first goal is to discuss how the laser beam fills the objective back focal plane. For this, we will define some parameters of the paraxial and strongly focused fields. One of the most relevant aspects for an adequate comparison between the theoretical model and the experiment is the presence of spherical aberration introduced by refraction at the glass-water interface when employing oil-immersion objectives. The effect of this aberration will also be discussed in the first section.

In the following section, we present the model for optical forces on a spherical (Mie) particle exerted by an incident field described by the Richards-Wolf model, presented in the preceding section. In the first subsection, we present the Debye potentials related to the strongly focused incident fields and scattered fields, the latter given in terms of the Mie scattering coefficients [2]. From the Debye potentials for the incident and scattered fields, we obtain the expressions of the Mie-Debye model for the optical force, which are discussed and presented in the final part of the section.

From the radial component of the optical force, we can analyze the stability of the optical trap. In the third section, we characterize the possible stability arrangements present in the trap using vortex beams. One of the possible stability states consists of an optical bistable force field, which is of special interest for this thesis since we were the first to discover and demonstrate it. This topic will be discussed in more detail in chapter 3.

Finally, we will present the Langevin equation and some quantities derived from the position's time series, which will be used in the analysis of the results contained in this thesis. Additionally, we will discuss a numerical method to simulate Brownian dynamics from the so-called Ornstein-Uhlenbeck process [3, 4, 5], which corresponds to a possible realization of the time-discrete Langevin equation.

2.1 Richards-Wolf model for tightly focused vortex beams

Optical beams are typically modeled using the paraxial approximation due to its simplicity. For the description of the paraxial optics model to be valid, the beam must satisfy the small-angle condition. This means that the more collimated the beam is, the better the description provided by the paraxial optics model. Furthermore, the expressions for optical beams provided by the paraxial equation are not, in general, solutions of the Helmholtz equation (a straightforward exception would be the plane-wave limit). Therefore, beams focused by objective lenses with high NA should not be accurately described by the paraxial model.

As we will see in this section, the Richards-Wolf model solves both problems mentioned above. In contrast to the paraxial optics approach, the Richards-Wolf model provides expressions that are solutions of the Helmholtz equation and are valid for any aperture angle (bounded by the numerical aperture (NA) of the objective). The operation of an optical tweezers with a single trapping beam employs large NA objectives so as to produce the required intensity gradients. Thus, it is important to describe the trapping beam using the non-paraxial Richards-Wolf model. However, the incident beam at the objective lens entrance is well described by the paraxial model as its waist is much larger than the wavelength.

Therefore, we begin this section by describing the paraxial mode that illuminates the objective lens's back focal plane. The paraxial mode in question is a (left) circularly polarized vortex beam, which exhibits a series of properties that will be explored in the following subsection.

2.1.1 Paraxial Laguerre-Gaussian modes

Vortex beam (VB) is the generic term used to refer to light beams that carry orbital angular momentum (OAM). The presence of OAM is characterized by a helical phase distribution $\exp(i\ell\phi)$, where ℓ is the topological charge and ϕ is the azimuthal coordinate. The topological charge is the integer number of 'helices' the wavefront possesses, *i.e.* the number of times the helical transversal phase goes from 0 to 2π over the azimuthal coordinate of the beam transverse plane. It can be directly interpreted as the amount of OAM each photon on the beam carries ($\ell\hbar$ per photon). Therefore, the total angular momentum will be determined by the topological charge along with the polarization of the beam, with the latter contributing with $\pm\hbar$ per photon if it is left $(+)$ or right $(-)$ circularly polarized.

Every VB exhibits a phase singularity on its optical axis, which is responsible for the characteristic annular shape of the transverse intensity profile. While it is possible to create VBs with a wide variety of transverse modes for the same topological charge ℓ, the Laguerre-Gaussian (LG) modes ($\mathrm{LG}_{p,\ell}$) stand out as an orthogonal set of solutions of the paraxial equation. This means that one can easily describe the optical field of a given LG mode with only a few paraxial parameters such as the beam waist w_0, the Rayleigh length z_R, and the curvature radius $R(z)$.

For simplicity, we neglect astigmatism and model the paraxial beam entering the objective back aperture as a circularly polarized Laguerre-Gaussian ($\mathrm{LG}_{0\ell}$) mode with radial order $p = 0$. The symmetries of such system lead us to use cylindrical coordinates, where the corresponding electric field reads

$$\mathbf{E}_{\mathrm{p}}(\rho, \phi, z) = E_0 \left(\frac{\sqrt{2}\rho}{w_0} \right)^{|\ell|} e^{-\frac{\rho^2}{w_0^2}} e^{i\ell\phi} e^{ik_0 z} \hat{\boldsymbol{\epsilon}}_\sigma. \tag{2.1}$$

Here, $k_0 = 2\pi/\lambda_0$ is the laser wavenumber, $\hat{\boldsymbol{\epsilon}}_\sigma = (\hat{\mathbf{x}} + i\sigma\hat{\mathbf{y}})/\sqrt{2}$ are the unit vectors for left-handed ($\sigma = 1$) and right-handed ($\sigma = -1$) circular polarizations, ρ is the radial distance from the optical axis and w_0 is the beam waist. For a circularly polarized beam, the magnetic field reads:

$$\mathbf{H}_{\mathrm{p}}(\rho, \phi, z) = -i\sigma\sqrt{\frac{\epsilon}{\mu_0}} \mathbf{E}_{\mathrm{p}}(\rho, \phi, z), \tag{2.2}$$

where ϵ is the medium electric permittivity and μ_0 is the vacuum magnetic permeability.

Typical optical tweezers setups employ fundamental Gaussian modes as the input laser beams, meaning that w_0 is normally used to characterize the transverse intensity profile. While the size of the Gaussian mode intensity profile is directly related to w_0 through a radial Gaussian distribution ($\exp(-2\rho^2/w_0^2)$), $\mathrm{LG}_{0\ell}$ modes are ring-shaped and axially localized, and the larger the topological charge ℓ, the larger and thinner the annular intensity profile is for the same waist w_0. This implies that the size of a $\mathrm{LG}_{0\ell}$ mode intensity profile should be characterized otherwise. We can take the derivative of $|E_{\mathrm{p}}|^2$ with respect to ρ to obtain the radial coordinate of peak intensity r_ℓ from eq. 2.1:

$$r_\ell = w_0\sqrt{\frac{|\ell|}{2}}, \tag{2.3}$$

which is a more suitable parameter to characterize the annular beam size instead of the usual waist w_0.

Indeed, the beam waist w_0 will still be used as the input parameter in the model we will discuss next, but since r_ℓ possesses more physical meaning and a clear geometrical appeal, all discussions regarding beam size will be done with it.

In the next subsection, we'll present the Richards-Wolf model for a strongly focused vortex beam, where the expressions for the electric field and energy density will be derived. From these quantities, we'll establish one of the criteria for ensuring the incident beam's efficiency in the optical trapping of particles. To accomplish this, we'll define a quantity using the maximum intensity radius of the vortex beam r_ℓ, defined above, and the aperture radius of the objective lens' back focal plane. This quantity will be the main control parameter of what we call the filling criterion.

2.1.2 Tight focusing and spherical aberration

The paraxial optics model used in the last subsection employs small angle approximations on the angular spectrum of the field, making it unsuitable to provide an adequate description of the fields in optical systems possessing a high numerical aperture parameter. Microscope objective lenses with high NA are one such example, which demands a theoretical modeling that incorporates the non-paraxiality of the tightly focused optical beam.

The Richards-Wolf (RW) model is a vector diffraction model that describes the focusing by an aplanatic objective lens. An objective lens is called aplanatic when it is designed to be aberration-free (or stigmatic) and to obey the Abbe sine condition. A detailed description of this model can be found in the references [1, 6], and the model extension for $\mathrm{LG}_{0\ell}$ modes is well discussed in reference [7]. In this subsection, we present the derivation of the RW model and the resulting expressions for the focal field in terms of the incident $\mathrm{LG}_{0\ell}$ mode. Special attention is dedicated to some intricate passages in the theory development, as they might clarify future discussions involving the focal electromagnetic fields and the Mie-Debye model expressions for the optical force.

We begin considering a paraxial beam given by eq. 2.1 illuminating the aperture of an objective lens of numerical aperture NA. The strongly focused non-paraxial beam after the objective is represented as a Debye-type (Fourier) superposition of plane waves with wavevectors $\mathbf{k}(\theta, \varphi)$ spanning the angular sector defined by the conditions $0 \leq \varphi < 2\pi$ and $0 \leq \theta \leq \theta_0 = \sin^{-1}\left(\frac{\mathrm{NA}}{n_i}\right)$, where n_i is the refractive index of the objective immersion medium. In contrast with the paraxial optics approach, the RW model represents the focused field as a linear sum of solutions of the Helmholtz equation. On top of that, the paraxial approximation requirement that the angles between the wavevector and the optical axis be small ($\theta \ll 1$) is not imposed in the RW model. All Fourier components satisfy $|\mathbf{k}(\theta, \varphi)| = n_i k_0$.

In order to reach high NA values, some objective lenses require an immersion media with a high refractive index. In our experimental setup, we employ the optical trap with an oil-immersion objective, where the immersion oil refractive index is chosen to match the one of glass (of the microscope slide in the sample chamber), whilst mismatching the sample aqueous medium refractive index n_1. This index mismatch causes the focused beam to be further refracted at the glass-water interface, which has an important effect on the optical force as it degrades the focal region by introducing spherical aberration. For each Fourier component, the resulting spherical aberration phase scales with the distance L between the objective focal plane and the slide [8]:

$$\Phi(\theta) = kL\left(-\frac{\cos\theta}{N_a} + N_a\,\cos\theta_1\right), \tag{2.4}$$

where θ_1 is the refraction angle in the sample chamber, and $N_a = n_1/n_i$ is the relative refractive index of host and immersion media; in our case, water with respect to oil and glass. Each Fourier component will also be attenuated by the Fresnel complex amplitude transmission coefficient:

$$T(\theta) = \frac{2\cos\theta}{\cos\theta + N_a\cos\theta_1}\,. \tag{2.5}$$

For high-NA objectives, the part of the angular spectrum corresponding to $\theta >$

$\sin^{-1}(N_a)$ gives rise to evanescent waves in the sample chamber. In a usual experimental setup, we assume that the trapped particle is a few wavelengths away from the glass slide at the bottom of the sample region, allowing us to neglect the contribution of the evanescent sector as well as the effect of optical reverberation between particle and glass slide [9]. The contribution from the evanescent sector is discarded by taking $\theta_0 = \sin^{-1}(N_a)$ when NA $> n_1$.

The resulting electric field in the sample region is given by:

$$\begin{aligned}\mathbf{E}_\ell^{(\sigma)}(\mathbf{r}) &= \left(\frac{-ikfe^{-ikf}}{2\pi}\right) E_0(-\sqrt{2}\gamma)^{|\ell|} \\ &\times \int_0^{2\pi} d\varphi\, e^{i\ell\varphi} \int_0^{\theta_0} d\theta\, (\sin\theta)^{1+|\ell|} \sqrt{\cos\theta} e^{-\gamma^2 \sin^2\theta} T(\theta) e^{i\Phi(\theta)} e^{i\mathbf{k}_1(\theta_1,\varphi)\cdot\mathbf{r}} \hat{\boldsymbol{\epsilon}}'_\sigma(\theta_1,\varphi)\,, \end{aligned} \tag{2.6}$$

where $\gamma = f/w_0$ is the ratio between the objective focal length and the beam waist and $\mathbf{k}_1$ is the wavevector in the aqueous medium, satisfying $|\mathbf{k}_1| = n_1 k_0$. The wavevector spherical coordinates (θ, φ) are related to the input paraxial fields cylindrical coordinates (ρ, ϕ) through the Abbe sine condition $\rho = f\sin\theta$ and $\phi = \varphi + \pi$.

The expression in eq. 2.6 can be simplified by solving the integral with respect to φ. In order to do this, we should first clarify how the focusing process transforms the polarization vectors $\hat{\boldsymbol{\epsilon}}_\sigma$ defining our paraxial state into the unit vector $\hat{\boldsymbol{\epsilon}}'_\sigma$ in eq. 2.6. Additionally, we should explicitly write the exponential term $\exp\{i\mathbf{k}_1(\theta,\varphi)\cdot\mathbf{r}\}$ as it also depends on the azimuth coordinate φ. The symmetry of the objective lens will transform the radial and azimuthal ($\hat{\rho}$ and $\hat{\phi}$) vector components of the paraxial field in cylindrical coordinates into polar and azimuthal ($\hat{\theta}$ and $\hat{\varphi}$) components of the focal field, respectively [6][1]. The decomposition of $\hat{\rho}$, $\hat{\phi}$, $\hat{\theta}$ and $\hat{\varphi}$ into unit vectors in Cartesian coordinates $(\hat{x}, \hat{y}, \hat{z})$ is as

[1]For an in-depth explanation and visualization of the tight-focusing process, see sections 3.5-3.7 of ref. [6], where the discussions on the transformation of the polarization vectors and the power transmittance of the light field are made using diagrams (Figs. 3.6 and 3.7) together with a careful development of the respective diffraction model.

follows:

$$\hat{\rho} = \cos\phi\,\hat{x} + \sin\phi\,\hat{y}\,,$$
$$\hat{\phi} = -\sin\phi\,\hat{x} + \cos\phi\,\hat{y}\,,$$
$$\hat{\theta} = \cos\theta\,\cos\varphi\,\hat{x} + \cos\theta\,\sin\varphi\,\hat{y} - \sin\theta\,\hat{z}\,,$$
$$\hat{\varphi} = -\sin\varphi\,\hat{x} + \cos\varphi\,\hat{y}\,. \tag{2.7}$$

For a Therefore, the unit vector $\hat{\boldsymbol{\epsilon}}'_\sigma$ defining the polarization state of the focused field can be written in Cartesian coordinates as[2]:

$$\begin{aligned}\hat{\boldsymbol{\epsilon}}'_\sigma(\theta,\varphi) &= (\hat{\boldsymbol{\epsilon}}_\sigma\cdot\hat{\rho})\,\hat{\theta} \;+\; (\hat{\boldsymbol{\epsilon}}_\sigma\cdot\hat{\phi})\,\hat{\varphi} \;= \\ &\frac{1}{2}\Big\{\sin^2(\theta/2)\Big[(\sigma-1)e^{-i2\varphi} \;-\; (\sigma+1)e^{i2\varphi}\Big] \;+\; 2\,\cos^2(\theta/2)\Big\}\,\hat{x}\;+ \\ &\frac{i}{2}\Big\{\sin^2(\theta/2)\Big[(\sigma-1)e^{-i2\varphi} \;+\; (\sigma+1)e^{i2\varphi}\Big] \;+\; 2\sigma\cos^2(\theta/2)\Big\}\,\hat{y}\;+ \\ &\frac{1}{2}\Big\{\sin\theta\Big[(\sigma-1)e^{-i\varphi} \;-\; (\sigma+1)e^{i\varphi}\Big]\Big\}\,\hat{z}.\end{aligned} \tag{2.8}$$

We proceed by writing the product $(\mathbf{k}(\theta,\varphi)\cdot\mathbf{r})$ as:

$$\begin{aligned}&\mathbf{k}(\theta,\varphi)\cdot\mathbf{r} = \\ &k(\sin\theta\,\cos\varphi\,\hat{x} + \sin\theta\,\sin\varphi\,\hat{y} + \cos\theta\,\hat{z})\cdot(\rho\,\cos\phi\,\hat{x} + \rho\,\sin\phi\,\hat{y} + z\hat{z}) = \\ &k\,z\,\cos\theta \;+\; k\,\rho\,\sin\theta\,\cos(\varphi-\phi)\,,\end{aligned} \tag{2.9}$$

which finally leads to the following azimuthal integral:

$$\int_0^{2\pi} d\varphi\, e^{i\ell\varphi} e^{ik\,\rho\,\sin\theta\,\cos(\varphi-\phi)}\hat{\boldsymbol{\epsilon}}'_\sigma(\theta,\varphi)\,. \tag{2.10}$$

When substituting $\hat{\boldsymbol{\epsilon}}'_\sigma$ into eq. 2.10, only five different integrands will occur. Indeed, for any of the possible integrands, the resulting integral in eq. 2.10 has the following solution [10]:

$$\int_0^{2\pi} d\varphi\, e^{iM\varphi} e^{i\xi\cos(\varphi-\phi)} \;=\; 2\pi(i)^M J_M(\xi)\, e^{iM\phi}\,, \tag{2.11}$$

[2]This expression was obtained from the relations in eq. 2.7 and the definition of the circular polarization unit vector. Additionally, the following trigonometric properties were used in the next two equations: $(1-\cos\theta) = 2\sin^2(\theta/2)$, $\cos\theta = \cos^2(\theta/2) - \sin^2(\theta/2)$, $\sin\varphi\,\cos\varphi = (1/2)\sin(2\varphi)$, $\sin^2\varphi = (1/2)(1-\cos(2\varphi)$ and $\cos\phi\,\cos\varphi + \sin\phi\,\sin\varphi = \cos(\varphi-\phi)$.

where $J_M(\xi)$ is the cylindrical Bessel function of order M. From eqs. 2.8 and 2.10, we can observe that M can only have the values $M = \{\ell \pm 2,\, \ell \pm 1,\, \ell\}$. By substituting them into eq. 2.6, we can define the function $I_m^{(\ell)}$:

$$I_m^{(\ell)}(\rho, z) = (\sqrt{2}\,\gamma)^{|\ell|} \int_0^{\theta_0} d\theta\, (\sin\theta)^{1+|\ell|} \sqrt{\cos\theta}\, e^{-\gamma^2 \sin^2\theta}\, T(\theta)\, e^{i\Phi(\theta)} \\ \times f_{|m|}(\theta)\, J_{\ell+m}(k_1\,\rho\,\sin\theta_1) e^{i\,k_1\,z\,\cos\theta_1}\,, \tag{2.12}$$

where $f_m(\theta)$ is the angular function, defined for $m = \{0,\, 1,\, 2\}$:

$$f_m(\theta) = \begin{cases} 2\,\cos^2(\theta/2) & \text{if } \; m = 0\,, \\ \sin\theta & \text{if } \; m = 1\,, \\ 2\,\sin^2(\theta/2) & \text{if } \; m = 2\,. \end{cases} \tag{2.13}$$

Finally, we are able to write the solution for the tightly focused electric field components in Cartesian coordinates:

$$\begin{aligned} E_x^{(\sigma,\ell)}(\mathbf{r}) \;&=\; (-i)^{\ell+1} \left(\frac{k\,\gamma\,w_0\,E_0}{2}\right) \left(e^{i\ell\phi}\, I_0^{(\ell)} \;+\; e^{i(\ell+2\sigma)\phi}\, I_{2\sigma}^{(\ell)}\right), \\ E_y^{(\sigma,\ell)}(\mathbf{r}) \;&=\; \sigma(-i)^{\ell} \left(\frac{k\,\gamma\,w_0\,E_0}{2}\right) \left(e^{i\ell\phi}\, I_0^{(\ell)} \;-\; e^{i(\ell+2\sigma)\phi}\, I_{2\sigma}^{(\ell)}\right), \\ E_z^{(\sigma,\ell)}(\mathbf{r}) \;&=\; -2\sigma(-i)^{\ell} \left(\frac{k\,\gamma\,w_0\,E_0}{2}\right) \left(e^{i(\ell+\sigma)\phi}\, I_{\sigma}^{(\ell)}\right). \end{aligned} \tag{2.14}$$

Therefore, the respective time-averaged electric energy density distribution $W_E^{(\sigma,\ell)}(\mathbf{r})$ in the focal region is:

$$W_E^{(\sigma,\ell)}(\mathbf{r}) \;=\; \left(\frac{\varepsilon_1}{4}\right)|\mathbf{E}|^2 \;=\; \left(\frac{k\,\gamma\,w_0\,E_0}{2}\right)^2 \left(\frac{\varepsilon_1}{2}\right) \left(|I_0^{(\ell)}|^2 \;+\; 2|I_\sigma^{(\ell)}|^2 \;+\; |I_{2\sigma}^{(\ell)}|^2\right). \tag{2.15}$$

Next, we'll use the result contained in eq. 2.15 to discuss the diffraction limit of strongly focused vortex beams. The focusing process with a high-NA lens causes the field in the focal region to be confined, depending on the parameters that characterize the paraxial beam at the back focal plane of the objective lens. The more confined the field, the greater the intensity gradient in the focal region and, therefore, the greater the gradient force the incident field is able to exert.

In the next section, we'll explore the behavior of the field intensity distribution in the focal region, given by eq. 2.15, and seek the configuration that maximizes trapping efficiency, *i.e.* that maximizes the intensity gradient of the incident field. In parallel, we'll present a quantity that quantifies the beam power that is lost during passage through the objective lens to the focal region. Taking both these discussions into account simultaneously, we'll define the so-called "filling criteria" for Optical Tweezers systems employing vortex beams.

2.1.3 Diffraction limit and filling fraction of tightly focused vortex beams

The tightly focused field intensity will be azimuthally symmetric for an aberration-free circularly polarized input VB, which is expected, as the focusing process has no mechanism to break the initial paraxial azimuthal symmetry. This wouldn't be the case for linearly polarized input paraxial beams or beams with aberrations like astigmatism and coma, which change their axis direction under rotations. The intensity distribution of the tightly focused field will be annular shaped, meaning its size can be characterized in a similar fashion as the paraxial $LG_{0\ell}$ mode, *i.e.* by the radial coordinate of the maximum intensity ring $\tilde{r}_\ell$. Here, the tilde indicates that this parameter refers to the non-paraxial focal field. The parameter $\tilde{r}_\ell$ will play an important role in defining the stability criteria for a VB OT. As mentioned earlier in this chapter, an overall rule that OTs obey to ensure efficient trapping is the "overfilling condition".

In paraxial optics, the size relation between the fields in the front and back focal planes of a lens is given by the properties of the Fourier-Bessel transform. The Fourier-Bessel transform is a 2 dimensional Fourier transform with azimuthal symmetry, which arises naturally when describing focusing with the Fresnel diffraction formula. This property of ideal thin and infinite lenses is the foundation of what is known as Fourier Optics [11]. The same logic can be used with high numerical aperture objectives to understand the overfilling condition principle: the larger the input field is, the more localized the focused field becomes, providing a higher intensity gradient around the focus. Therefore, the overfilling condition requires that the tightly focused fields are diffraction-limited in order to provide a more stable trap for a set amount of laser power arriving at the sample.

In order to obtain the focal field ring radius $\tilde{r}_\ell$, we have to evaluate eq. 2.15 numerically, yielding the field's spatial intensity distribution, from which we can obtain its peak radial position. By increasing the filling ratio r_ℓ/R_p, *i.e.* the ratio between the paraxial VB ring size r_ℓ and the objective lens aperture radius R_p, we observe that $\tilde{r}_\ell$ decreases until it converges to a minimum value, which is what we consider to be the diffraction-limited field size $\tilde{r}_\ell$. This behavior is depicted in fig. 2.1.

An interesting characteristic of the diffraction-limited $\tilde{r}_\ell$ is that it grows linearly with the topological charge ℓ, unlike its paraxial counterpart r_ℓ, which grows with $\sqrt{|\ell|}$ as shown in eq. 2.3. Additionally, $\tilde{r}_\ell$ also depends on the relative sign between ℓ and σ as a result of the spin-orbit coupling effect introduced by the strong focusing process [7]. In other words, if the orbital angular momentum (per photon/ number) $\ell\hbar$ of the paraxial input beam has the same sign as the spin angular momentum (per photon/ number) $\sigma\hbar$, then $\tilde{r}_\ell$ will be slightly bigger than in the case where the signs are opposite. This means that $\tilde{r}_\ell$ scales with the amount of total angular momentum of the input paraxial vortex beam.

One can assume that increasing the filling ratio as much as possible is sufficient to always obtain a diffraction-limited focal spot. However, this can't be the case, as choosing values of the filling ratio close to unity means that a significant part of the incident beam will be located outside the objective entrance, causing some laser power to be lost. This effect is accounted for by the filling fraction. We define it as the fraction of power transmitted from the input paraxial beam to the focal region inside the sample chamber. In addition to the loss caused by the finite objective aperture, we also consider the refraction due to the presence of an interface with mismatched refraction indices between the objective immersion and sample chamber media.

The power density before the interface is related to the Poynting vector $\mathbf{S} = \mathrm{Re}\frac{1}{2}(\mathbf{E} \times \mathbf{H}^*)$

as $\mathrm{d}P = (\mathbf{S}\cdot\hat{z})\,\mathrm{d}A$, where $\hat{z}$ is the Cartesian unitary vector, $\mathrm{d}A = 2\pi\,\rho\,\mathrm{d}\rho$ is the infinitesimal area of a ring coaxial with the objective lens. Using eqs. 2.1 and 2.2 to calculate the Poynting vector, we obtain the expression for the infinitesimal power before the interface:

$$\mathrm{d}P = \frac{\pi\,E_0^2\,n_i}{\mu_0\,c}\left(\frac{\sqrt{2}}{w_0}\right)^{2|\ell|} e^{-\frac{2\rho^2}{w_0^2}}\rho^{2|\ell|+1}\mathrm{d}\rho. \tag{2.16}$$

Using the Abbe sine condition $\rho = f\sin\theta$, one can obtain the infinitesimal power transmitted through the interface as a function of the incidence angle θ and given in terms of the square of the Fresnel transmission coefficient in eq. 2.5:

$$\begin{aligned} \mathrm{d}P_1 &= \frac{n_1\cos\theta_1}{n_i\cos\theta}\,[T(\theta)]^2\,\mathrm{d}P = \\ &= \frac{\pi\,f^2\,E_0^2\,n_1}{\mu_0\,c}\left(\frac{\sqrt{2}f}{w_0}\right)^{2|\ell|} e^{-\frac{2f^2\sin^2\theta}{w_0^2}}(\sin\theta)^{2|\ell|+1}\,\cos\theta_1\,[T(\theta)]^2\,\mathrm{d}\theta. \end{aligned} \tag{2.17}$$

Using the definition of $\gamma = f/w_0$ and integrating over θ, we obtain the total power that reaches the sample chamber:

$$P_1 = \frac{\pi\,f^2\,E_0^2\,n_1}{\mu_0\,c}\left(\sqrt{2}\gamma\right)^{2|\ell|}\int_0^{\theta_0} e^{-2\gamma^2\sin^2\theta}(\sin\theta)^{2|\ell|+1}\,\cos\theta_1\,[T(\theta)]^2\,\mathrm{d}\theta\,. \tag{2.18}$$

Now we take a few steps to simplify this expression. Using the Snell law, we can obtain two useful relations: $\sin\theta_1 = \sin\theta/N_a$ and $\cos\theta_1 = \sqrt{1-(\sin\theta/N_a)^2}$. Making the substitution $s = \sin\theta$ in the expression for $T(\theta)$, we obtain:

$$P_1 = \frac{2\pi\,n_i\,E_0^2\,w_0^2}{\mu_0\,c}\left(2\gamma^2\right)^{|\ell|+1}\int_0^{\sin\theta_0} e^{-2\gamma^2\,s^2}\,s^{2|\ell|+1}\frac{\sqrt{N_a-s^2}\,\sqrt{1-s^2}}{(\sqrt{N_a-s^2}\,+\,\sqrt{1-s^2})^2}\,\mathrm{d}s\,. \tag{2.19}$$

Now, a similar procedure can be used to obtain the total power of the paraxial beam:

$$P = \frac{\pi\,n_i\,E_0^2\,w_0^2}{2\,\mu_0\,c}\int_0^{\infty} e^{-2\gamma^2\,s^2}\,(\sqrt{2}\gamma s)^{2|\ell|+1}\sqrt{2}\gamma\,\mathrm{d}s\,. \tag{2.20}$$

Taking $t = \sqrt{2}\gamma s$, one can identify the integral definition of the Gamma function:

$$\Gamma(z+1) = 2\int_0^{\infty} e^{-t^2}\,t^{2z+1}\,\mathrm{d}t = z\,!\,. \tag{2.21}$$

The appearance of the Gamma function here is a direct consequence of how we normalized the $\mathrm{LG}_{0\ell}$ mode in eq. 2.1, where we omitted the pre-factors that would make the integral in eq. 2.20 be equal to unity.

The ratio between both powers quantifies the amount of laser power that is not lost due to the finite lens aperture size and the refraction at the immersion medium to the sample chamber medium interface. We identify this quantity as the filling fraction A_ℓ:

$$A_\ell = \frac{P_1}{P} = \frac{8(2\gamma^2)^{|\ell|+1}}{|\ell|!} \int_0^{\sin\theta_0} e^{-2\gamma^2 s^2}\, s^{2|\ell|+1} \frac{\sqrt{N_a^2 - s^2}\,\sqrt{1-s^2}}{(\sqrt{N_a^2 - s^2} + \sqrt{1-s^2})^2}\, \mathrm{d}s\,. \tag{2.22}$$

During the derivation of the MDSA expressions for the optical forces exerted by a tightly focused $\mathrm{LG}_{0\ell}$ mode, it will be useful to rewrite eq. 2.19 in terms of A_ℓ:

$$P_1 = \frac{\pi\, n_1\, E_0^2\, w_0^2}{4\, N_a\, \mu_0\, c}\, |\ell|!\, A_\ell\,. \tag{2.23}$$

Finally, we can evaluate the filling fraction and discuss its behavior in order to complete the discussion of the filling criteria. In Fig. 2.1, we illustrate how the A_ℓ function behaves as a function of the filling ratio r_ℓ/R_p for various values of ℓ. As we can see, the focal field

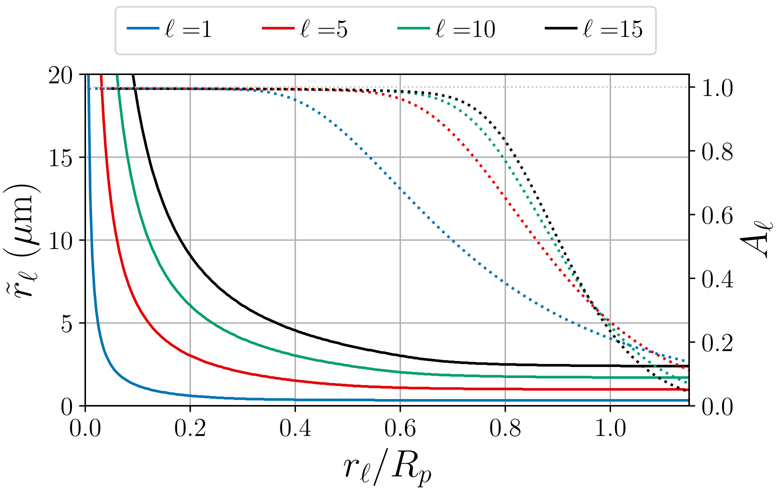

Figure 2.1: Radius $\tilde{r}_\ell$ of the focal annular spot (solid curves, left axis) and filling factor A_ℓ representing the fraction of total power transmitted to the sample chamber (dotted curves, right axis) as functions of the radius r_ℓ of the paraxial vortex beam (in units of the objective entrance radius $R_p = 2.8\,\mathrm{mm}$). The topological charges are $\ell = 1, 5, 10, 15$. We consider an oil-immersion objective lens with numerical aperture NA $= 1.4$.

maximum intensity ring radius $\tilde{r}_\ell$ converges to a diffraction-limited size at different values of the filling ratio r_ℓ/R_p for different topological charges. Smaller topological charge ℓ values (in modulus) reach diffraction-limited annular sizes at smaller values of r_ℓ/R_p.

For values of topological charges up to $\ell = 15$, Fig. 2.1 indicates that the diffraction-limited $\tilde{r}_\ell$ size is always reached for the filling ratio value of $r_\ell/R_p = 0.8$. However, smaller topological charge values show a faster power loss as r_ℓ/R_p increases, as we can explicitly see in the plots of A_ℓ for $\ell = \{1, 5\}$. This implies that modes with smaller topological charges should employ smaller filling ratios to minimize power loss. Therefore, we define the filling criteria as the set of two conditions that should be met simultaneously, *i.e.* $\tilde{r}_\ell$ must be diffraction-limited while keeping the filling fraction A_ℓ as close to unity as possible.

On the other hand, the filling ratio value $r_\ell/R_p = 0.8$ still exhibits a significant amount of power reaching the focal region for smaller topological charges. As an example, the case $\ell = 1$ still presents a filling fraction value of $A_\ell \approx 0.4$ for the filling ratio value above. Therefore, for practical reasons, we chose to employ the filling ratio value of $r_\ell/R_p = 0.8$ in our numerical analysis throughout the following sections and chapters (unless we state otherwise), as this condition can be set equally to every $\mathrm{LG}_{0\ell}$ mode, independently of the topological charge. Additionally, setting a fixed filling ratio value implies that the Fourier (plane-wave) component with the highest amplitude will always have the same incidence angle θ.

In the next section, we present the MDSA theory for the optical force, including the expressions for the efficiency factor (dimensionless optical force). Following the next section, we reach a point where all the topics we presented so far (regarding the filling criteria, the focal field intensity distribution, and the optical forces) will converge on the topic of characterization of different stability configurations in an Optical Tweezers system employing vortex beams.

2.2 Mie-Debye theory for vortex beams

In the previous section, we explored the non-paraxial model for the optical field produced by focusing a laser beam with an objective lens. We now proceed to the discussion of optical forces. We consider that a spherical particle scatters the incident optical field, resulting in the exchange of linear and angular momenta between the light and the scatterer. The scattering problem of an incident electromagnetic plane wave by a spherical dielectric object was solved in the early 1900s by L. Lorenz and G. Mie, providing two names for the resulting theory: Lorenz-Mie or simply Mie scattering theory.

The Mie-Debye theory, developed by H. M. Nussenzveig and P. A. M. Neto [12, 13], was the first theoretical formalism describing forces on OTs which employs the RW model for the incident field [14]. The scattered field is provided by the aforementioned Mie theory, which describes the EM scattering by a homogeneous sphere. In this formulation, the incident plane wave is decomposed into two scalar fields representing the transverse electric (TE) and transverse magnetic (TM) polarization modes. Then, each polarization component is expanded as spherical partial waves, also called electric (TM) and magnetic (TE) multipole waves, which form a solution basis of the Helmholtz equation in spherical coordinates. The partial waves are also eigenfunctions of the Mie scattering process and are indexed by an integer number j denoting the total angular momentum. The resulting scalar fields are called Debye potentials, and the scattering amplitudes, also called Mie coefficients, a_j and b_j, are obtained by solving the boundary conditions for the TM and TE components, respectively, on the sphere surface. The EM force in the Mie-Debye formalism is obtained by calculating the flux of the Maxwell stress tensor through a surface containing the scattering sphere, using both the incident and scattered fields.

This expansion can be done for each plane wave component in the RW model field. The composition of the beam is achieved by rotating the partial wave components using the Wigner D-matrix [15] while the field amplitude and phase of each component are weighted by the input paraxial field. The derivation of the Debye potentials of the incident and scattered fields and the corresponding optical forces has been done for quite a few experimental scenarios. Therefore, it is beyond the scope of this section to present the intricate details of such calculation. As such, it is sufficient to present the Debye potentials for the incident and scattered fields for our case, as well as the novel analytical expressions used throughout the projects.

2.2.1 Debye potentials and Mie scattering

In this subsection we will present the Debye potentials for the incident tightly focused vortex beam, as well as the resulting scattered field. In order to construct a Debye potential equivalent to the Debye-type integral representation for the Richards-Wolf model presented in sec. 2.1.2, we begin with a single circular polarized plane wave propagating along the $\hat{z}$ direction:

$$\mathbf{E} = E_0\, e^{ikz}\, e^{-i\omega t}\, \hat{\boldsymbol{\epsilon}}_\sigma, \tag{2.24}$$

where $\hat{\boldsymbol{\epsilon}}_\sigma(\hat{x} + i\sigma\hat{y})/\sqrt{2}$ is the unit vector defining the polarization state. For a circularly polarized wave, the magnetic field $\mathbf{H}$ is related to $\mathbf{E}$ as:

$$\mathbf{H} = \frac{-i\, n_i}{\mu_0\, c}\sigma\mathbf{E} \tag{2.25}$$

The Debye potentials are defined in terms of $\mathbf{E}$ and $\mathbf{H}$ as a sum of partial waves indexed by j:

$$\Pi^{\mathrm{E}} = \sum_{j=1}^{\infty} \frac{(\mathbf{r}\cdot\mathbf{E})_j}{j(j+1)}\,, \qquad \Pi^{\mathrm{M}} = \sum_{j=1}^{\infty} \frac{(\mathbf{r}\cdot\mathbf{H})_j}{j(j+1)}\,. \tag{2.26}$$

Therefore, the electric Debye potential for a single plane wave propagating along the $\hat{z}$ direction in the spherical partial wave basis is:

$$\Pi^{\mathrm{E}}_{\mathrm{pw}} = \left(\frac{\sigma\, E_0\, e^{-i\omega t}}{\sqrt{2}\, k}\right) \sum_{j=1}^{\infty} (i)^{j+1} \sqrt{\frac{4\pi\,(2j+1)}{j(j+1)}}\; j_j(kr)\, Y_j^{\sigma}(\theta,\phi)\,, \tag{2.27}$$

where $j_j(x)$ are the spherical Bessel functions of the first kind and $Y_j^m(\theta,\phi)$ are the spherical harmonics.

Each circularly polarized plane wave composing the incident tightly focused field will possess a phase and relative strength, according to eq. 2.6. Therefore, we can construct the Debye potentials for an incident field described by the Richards-Wolf model by rotating and combining the Debye potentials of a single plane-wave, given by eq. 2.27. A detailed description of the process to obtain the Debye potentials for the field in eq. 2.6 is presented in appendix B. A more detailed discussion can be found in [16].

In a general case, the Debye potential $\Pi^{\mathrm{E}}_{\mathrm{IN}}$ of any (Debye-type) superposition of circularly polarized plane-waves can be written in the following simple form:

$$\Pi^{\mathrm{E}}_{\mathrm{IN}} = \sigma\, C^{\mathrm{E}} \sum_{j,m} \Big(\Gamma^{\sigma}_{jm\ell}\, j_j(kr)\, Y^{\sigma}_j(\theta,\phi) \Big)\,, \tag{2.28}$$

where $\sigma = \pm 1$ identifies the polarization handedness (where $+$ and $-$ means left and right circularly polarized, respectively), C^{E} is a pre-factor (independent of j, m, ℓ, and σ), and $\Gamma^{\sigma}_{jm\ell}$ is called the multipole expansion coefficients, which carries the dependencies on the sum indices j and m, as well as σ and in our specific case, ℓ. Note that the integer m denotes the $z-$component of the total angular momentum. Additionally, we used the following compact notation for the sum over j and m:

$$\sum_{j,m} = \sum_{j=1}^{\infty} \sum_{m=-j}^{j}\,.$$

The expressions for $\Gamma^{\sigma}_{jm\ell}$ and C^{E} are also presented in appendix B.

We can also define the coefficient C^{M}, which is useful to simplify the expression for the magnetic Debye potential $\Pi^{\mathrm{M}}_{\mathrm{IN}}$. The latter can be obtained with eq. 2.25 and the electric Debye potential definition in eq. B.8, yielding the relation with $\Pi^{\mathrm{E}}_{\mathrm{IN}}$:

$$\Pi^{\mathrm{M}}_{\mathrm{IN}} = \frac{-i\, n_i}{\mu_0\, c}\,\sigma\, \Pi^{\mathrm{E}}_{\mathrm{IN}} = C^{\mathrm{M}} \sum_{j,m} \Big(\Gamma^{\sigma}_{jm\ell}\, j_j(kr)\, Y^{\sigma}_j(\theta,\phi) \Big)\,, \tag{2.29}$$

Possessing both the electric and magnetic Debye potentials for the incident field, the Debye potentials for the scattered fields are directly obtained using the Mie scattering theory. As the Mie coefficients $(-a_j)$ and $(-b_j)$ are the eigenvalues of the scattering process in the multipole partial waves basis, the scattered potentials are given by:

$$
\begin{aligned}
\Pi_{\mathrm{S}}^{\mathrm{E}} &= \sum_{j,m}(-a_j)\left(\Pi_{\mathrm{IN}}^{\mathrm{E}}\right)_{j,m} = \sigma\, C^{\mathrm{E}} \sum_{j,m}(-a_j)\left(\Gamma_{jm\ell}^{\sigma}\, j_j(kr)\, Y_j^{\sigma}(\theta,\phi)\right), \\
\Pi_{\mathrm{S}}^{\mathrm{M}} &= \sum_{j,m}(-b_j)\left(\Pi_{\mathrm{IN}}^{\mathrm{M}}\right)_{j,m} = C^{\mathrm{M}} \sum_{j,m}(-b_j)\left(\Gamma_{jm\ell}^{\sigma}\, j_j(kr)\, Y_j^{\sigma}(\theta,\phi)\right),
\end{aligned} \tag{2.30}
$$

Numerous textbooks and theses present the full derivation of the Mie scattering problem (see for instance [2, 16, 17, 18]). The first step for obtaining the Mie coefficients is to recover the electric and magnetic fields from the Debye potentials using two vector operators that commute with ∇^2 : $\mathbf{L} = -i\mathbf{r} \times \nabla$ and $\nabla \times \mathbf{L}$. The boundary conditions on the surface of the sphere require that the tangential components of both the electric $\mathbf{E}$ and magnetic $\mathbf{H}$ fields must be continuous. The Mie coefficients for the scattered and internal fields are then obtained by solving a linear system resulting from those boundary conditions. However, our interests reside in the scattered field coefficients only, which are given by:

$$
\begin{aligned}
a_j &= \frac{n_2\, \psi_j'(k_1\, a)\, \psi_j(k_2\, a) \;-\; n_1\, \psi_j(k_1\, a)\, \psi_j'(k_2\, a)}{n_2\, \zeta_j^{(1)\prime}(k_1\, a)\, \psi_j(k_2\, a) \;-\; n_1\, \zeta_j^{(1)}(k_1\, a)\, \psi_j'(k_2\, a)}, \\
b_j &= \frac{n_2\, \psi_j(k_1\, a)\, \psi_j'(k_2\, a) \;-\; n_1\, \psi_j'(k_1\, a)\, \psi_j(k_2\, a)}{n_2\, \zeta_j^{(1)}(k_1\, a)\, \psi_j'(k_2\, a) \;-\; n_1\, \zeta_j^{(1)\prime}(k_1\, a)\, \psi_j(k_2\, a)},
\end{aligned} \tag{2.31}
$$

where n_1 and n_2 are the refractive indices of the host medium and the sphere, respectively. The size parameters k_1a and k_2a are given in terms of the sphere radius a and the wavenumbers in the host medium ($k_1 = n_1\, k_0$) and in the sphere ($k_2 = n_2\, k_0$). The Ricatti-Bessel functions $\psi_j(x) = x\; j_j(x)$ and $\zeta_j^{(1)}(x) = x\; h_j^{(1)}(x)$ are given in terms of the spherical Bessel ($j_j(x)$) and Hankel ($h_j^{(1)}(x)$) functions of the first kind, while the prime symbol denotes their derivatives with respect to the argument (*i.e.* the size parameters k_1a and k_2a).

Now, in possession of the expressions for the Debye potentials of the incident and scattered fields, we can finally proceed to the topic of the Mie-Debye model for the optical forces. The method to obtain the efficiency factor expressions for a tightly focused vortex beam does not differ from the usual cases (optical trapping with circularly polarized Gaussian modes) discussed in full detail in references [12, 13, 16]. Therefore, the force calculations will be omitted to avoid redundancy.

However, we should still present the interpretation of each term composing the efficiency factor expressions. This will be the subject of the following subsection and will be the last topic before we discuss the characterization of the equilibrium configurations present in a vortex beam trap.

2.2.2 MDSA expressions for the optical force

The MDSA expressions for the optical forces are labeled according to physical characteristics of each term. The optical force is given by the flux of the Maxwell stress tensor, which itself is composed of terms proportional to the square of the total field written as the sum of the incident and scattered contributions: $\mathbf{E} = \mathbf{E}_{\mathrm{IN}}+\mathbf{E}_{\mathrm{S}}$.

Therefore, the MDSA expressions will have terms proportional to $(\mathbf{E}_{\mathrm{IN}} \cdot \mathbf{E}^*_{\mathrm{IN}})$, $(\mathbf{E}_{\mathrm{S}} \cdot \mathbf{E}^*_{\mathrm{S}})$ and $(\mathbf{E}_{\mathrm{IN}} \cdot \mathbf{E}^*_{\mathrm{S}})$. The incident-incident term $(\mathbf{E}_{\mathrm{IN}} \cdot \mathbf{E}^*_{\mathrm{IN}})$ does not contribute to the flux as expected. The incident-scattered $(\mathbf{E}_{\mathrm{IN}} \cdot \mathbf{E}^*_{\mathrm{S}})$ and scattered-scattered $(\mathbf{E}_{\mathrm{S}} \cdot \mathbf{E}^*_{\mathrm{S}})$ terms will contribute to the extinction and scattering components of the optical force, respectively.

The extinction force component $\mathbf{F}_e$ is the linear momentum transfer rate from the incident field to the system composed of the scattered field and the microsphere ($-\dot{\mathbf{p}}_{\mathrm{in}}$, with the upper dot denoting a time derivative), while the scattering force component $\mathbf{F}_s$ is minus the rate at which the scattered field gains linear momentum ($-\dot{\mathbf{p}}_{\mathrm{s}}$). This is neatly illustrated in fig. 2.2, where we note that the total linear momentum of the system is conserved, yielding a resulting optical force that obeys:

$$\mathbf{F} \;=\; \mathbf{F}_e + \mathbf{F}_s \;=\; -\dot{\mathbf{p}}_{\mathrm{in}} - \dot{\mathbf{p}}_{\mathrm{s}} \;=\; \dot{\mathbf{p}}_{\mathrm{s}} + \dot{\mathbf{p}}_{\mathrm{sphere}} - \dot{\mathbf{p}}_{\mathrm{s}} \;=\; \dot{\mathbf{p}}_{\mathrm{sphere}}\,, \tag{2.32}$$

where $\dot{\mathbf{p}}_{\mathrm{sphere}}$ is the time derivative of the linear momentum transfer rate to the microsphere.

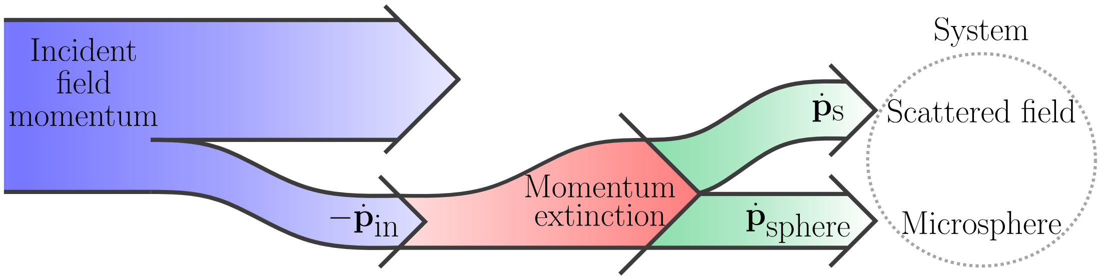

Figure 2.2: Schematic illustration of the momentum transfer balance. The momentum extinction rate (red filled arrow) is the rate of momentum removal from the incident field (blue filled arrow) to the system, composed of the scattered field and the scattering microsphere (green filled arrows).

It is useful to define the optical force in terms of the efficiency factor, which is a dimensionless quantity independent of the trapping beam power: As the optical force is proportional to the field power P at the sample, it's useful to define the dimensionless force [19] $\mathbf{Q}$, which is also called efficiency factor:

$$\mathbf{Q} = \frac{\mathbf{F}}{n_1 \, P/c} = \mathbf{Q}_s + \mathbf{Q}_e \,, \tag{2.33}$$

where c is the speed of light in vacuum. The vector fields $\mathbf{Q}_e$ and $\mathbf{Q}_s$ can be derived from the results for the scattered field obtained in the previous sub-sections as detailed in [16]. The radial extinction component of the efficiency factor in cylindrical coordinates is:

$$Q_{e\rho} = \frac{(2\gamma^2)^{|\ell|+1}}{|\ell|! \, A_\ell \, N_a} \sum_{jm} \mathrm{Im}\Big[(2j+1)(a_j+b_j)G_{j,m}\left(G^{(-)}_{j,m+1} - G^{(+)}_{j,m-1}\right)^*\Big] \,, \tag{2.34}$$

while the radial scattering component is:

$$\begin{aligned} Q_{s\rho} = & \frac{2(2\gamma^2)^{|\ell|+1}}{|\ell|! \, A_\ell \, N_a} \sum_{jm} \Bigg[\frac{\sqrt{j(j+2)(j+m+1)(j+m+2)}}{(j+1)} \times \\ & \times \mathrm{Im}\left((a_j a^*_{j+1} + b_j b^*_{j+1}) \left(G_{j,m} G^*_{j+1,m+1} + G_{j,-m} G^*_{j+1,-m-1} \right) \right) - \\ & -2\sigma \frac{(2j+1)}{j(j+1)} \sqrt{(j-m)(j+m+1)} \; \mathrm{Re}(a_j b^*_j) \; \mathrm{Im}\left(G_{j,m} G^*_{j,m+1} \right) \Bigg] \,. \end{aligned} \tag{2.35}$$

The efficiency factor components are written in terms of the multipole coefficients $G_{j,m}$,

$G'_{j,m}$, and $G^{(\pm)}_{j,m}$. The expression for $G_{j,m}$ is:

$$G_{jm} = \int_0^{\theta_0} d\theta (\sin\theta)^{|\ell|+1} \sqrt{\cos\theta}\, T(\theta)\, d^j_{m,\sigma}(\theta_1) \times \\ J_{m-\sigma-\ell}(k_1 \rho \sin\theta_1) e^{i(\Phi(\theta) + k_1 \cos\theta_1 z) - \gamma^2 \sin^2\theta}, \tag{2.36}$$

where $J_m(x)$ are the cylindrical Bessel functions of integer order [20].

The azimuthal and axial components of the extinction and scattering factors $Q_{e\phi}$, $Q_{s\phi}$, Q_{ez}, and Q_{sz}, as well as the remaining multipole coefficients $G'_{j,m}$, and $G^{(\pm)}_{j,m}$, are given in appendix B.

In the following section, we will discuss the stability characterization of optical traps with vortex beams. We chose to display the radial force components in the present section instead of the appendix to emphasize that this component will be slightly more important than the remaining for the discussions in the next section. Indeed, the entire stability characterization process will be carried out using the radial force component alone, as the field's annular shape will heavily influence the stability configuration on the transverse (xy) plane. Meanwhile, we will present arguments to justify our assumption that axial equilibrium (along the $z-$direction) is always achieved and that the azimuthal force component won't exhibit any equilibrium configuration by the symmetry of the system.

2.3 Stability characterization with aberration-free theory

In classical mechanics, an equilibrium position in a force field is the coordinate for which the force equals zero. Stable equilibrium has the extra requirement that each of the force components derivatives at the equilibrium position have to be negative. Throughout the rest of the thesis, we might use the term stable equilibrium position for one force component alone, and though this isn't strictly accurate, it greatly facilitates the discussion of optical forces of OTs with $\mathrm{LG}_{0\ell}$ input modes.

In section 2.1, we discussed the azimuthal symmetry present in the expressions for the intensity distribution of a tightly focused circular polarized $\mathrm{LG}_{0\ell}$ mode. Likewise, the resulting optical force also exhibits azimuthal symmetry, *i.e.* its expressions do not depend on the cylindrical azimuth coordinate ϕ as they lack any mechanism to break this rotation symmetry. Therefore, instead of numerically calculating $\mathbf{Q}$ in the 3-dimensional space, it suffices to calculate each component in the (ρz) plane.

In this section, we will explore different stability configurations in an optical trap setup that employs vortex beams. Two trapping states regimes are expected when comparing the trapping beam maximum intensity radius $\tilde{r}_\ell$ and the microsphere radius a [21, 22, 23]: when $a \ll \tilde{r}_\ell$, the particle is trapped near the ring of maximum energy density while being driven by the optical torque [24, 25] (called orbital trapping); and when $a \gg \tilde{r}_\ell$, the microsphere is too big to resolve the spatial variation of the annular focal spot and is trapped on the optical axis. An intuitive way to understand the case $a \ll \tilde{r}_\ell$ is from the Rayleigh picture, where a gradient (therefore conservative) force pulls the small spheres into the maximum intensity ring and the orbital motion arises from the non-conservative azimuthal force component due to the presence of light orbital angular momentum [26, 27]. In the opposite scenario $a \gg \tilde{r}_\ell$, the microsphere will be trapped on the optical axis as it will probe the entire annular field at once, neglecting intensity variations of length scales smaller than its own.

For clarity and didactic purposes, throughout this section we will consider an aberration-free trap, which can be experimentally implemented with a water-immersion objective. The aberration-free Mie-Debye theory is recovered by taking $N_a = 1$ in eq. 2.4 leading to a vanishing spherical aberration phase $\Phi(\theta) = 0$. Therefore, the absence of spherical aberration exempt us to deal with the additional parameter L, which greatly simplify the calculations and analysis. Indeed, our aberration-free MD results confirm the existence of these two trapping regimes, which were already quite explored throughout the literature. More importantly than such confirmation is that we find intermediate particle sizes $a \sim \tilde{r}_\ell$

where the two stable trapping states (axial and orbital) co-exist. We refer to this case as a bistable trap configuration, as the particle might randomly hop between the on-axis and the orbital states by thermal activation alone, provided that the laser beam power is sufficiently low.

2.3.1 Axial and orbital trapping and the critical radii

When considering an aberration-free beam, we know that the peak intensity point will be situated at the focal plane $z = 0$. Therefore, we expect that the axial equilibrium position z_{eq} will be near the focal plane, excluding the necessity to calculate z_{eq} numerically for every simulation point. On top of the optical axis ($\rho = 0$), both Q_ρ and Q_ϕ will be equal to zero. The radial component Q_ρ is expected to be linear near $\rho = 0$, allowing us to define the transverse trap stiffness κ_ρ as:

$$\kappa_\rho = -\frac{n_1 P}{c}\left(\frac{\partial Q_\rho}{\partial \rho}\right)\bigg|_{\rho=0}, \tag{2.37}$$

where P is the laser power. Therefore, by the definition above, on-axis trapping requires a positive transverse trap stiffness $\kappa_\rho > 0$.

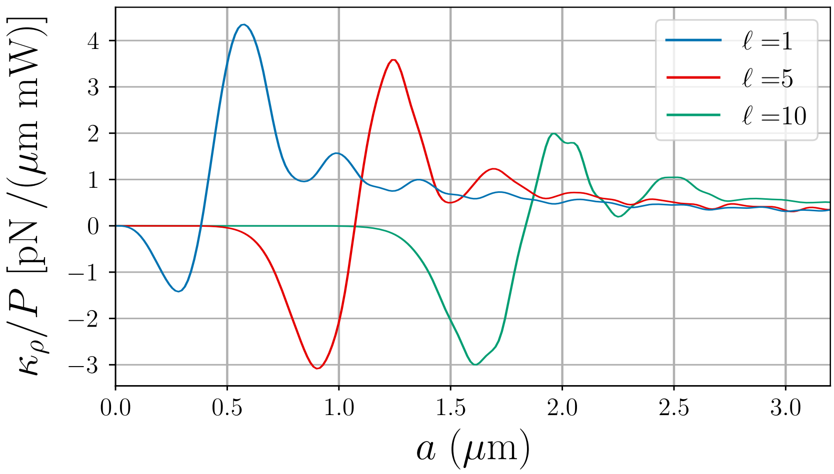

Figure 2.3: Transverse trap stiffness per unit power κ_ρ/P as a function of the sphere radius for topological charges $\ell = 1$ (blue), 5 (red) and 10 (green). We consider an aberration-free trapping beam. As the particle size increases, κ_ρ changes sign from negative to positive at the critical radius R_{on}.

In Fig. 2.3 we plot κ_ρ/P as a function of the trapped sphere radius a for three distinct topological charges ℓ. As explained in section 2.1.3, the diffraction-limited trapping beam maximum intensity radius $\tilde{r}_\ell$ scales linearly with ℓ for $\ell \gg 1$ [7, 25], also making the hole around the optical axis bigger. The straightforward consequence is that spheres much smaller than the hole will not probe any field on the optical axis. This explains the zero value line at the beginning of each κ_ρ/P curve, where the larger the topological charge ℓ the longer the curve stays on zero. As the radius a grows and begins to probe the field, the radial gradient force component will pull the sphere outwards, rendering a negative κ_ρ and therefore an unstable trap on the axis.

The sphere radius for which κ_ρ flips sign from negative to positive is a critical sphere radius R_{on} that also increases with ℓ. Thus, on-axis trapping is excluded for sphere radii smaller than R_{on} and only orbital trapping may occur. For any positive value of ℓ, we find a critical sphere radius R_{on} that increases with ℓ. In line with the above qualitative discussion, R_{on} is comparable to the focal spot annular radius $\tilde{r}_\ell$, as is shown in Fig. 2.4. The plot shows the characteristic radii of the field and the critical radii of trapped spheres as functions of ℓ, where we can see that R_{on} (green) is slightly smaller than $\tilde{r}_\ell$ (orange circles).

Now, if we search for a similar condition for off-axis trapping, we'll find a second critical radius R_{off}. Similarly to the last case, if $a > R_{\text{off}}$ then off-axis trapping is no longer possible since the only stable equilibrium position of $Q_\rho(\rho, z = 0) = 0$ is at $\rho = 0$, with $\kappa_\rho(\rho = 0, z = 0) > 0$. We also plot R_{off} as a function of ℓ in Fig. 2.4, where we note that R_{off} is very close to $\tilde{r}_\ell$ and R_{on} for small values of ℓ, and then becomes increasingly larger than both as ℓ increases.

On-axis and off-axis stable equilibria co-exist in between the two exclusion zones shown in Fig. 2.4, corresponding to microsphere radii in the (colored) stripe defined by $R_{\text{on}} < a < R_{\text{off}}$. Depending on the optical potential landscape, which scales with the laser beam power, a bistable trap might be demonstrated in this case by measuring the thermally-

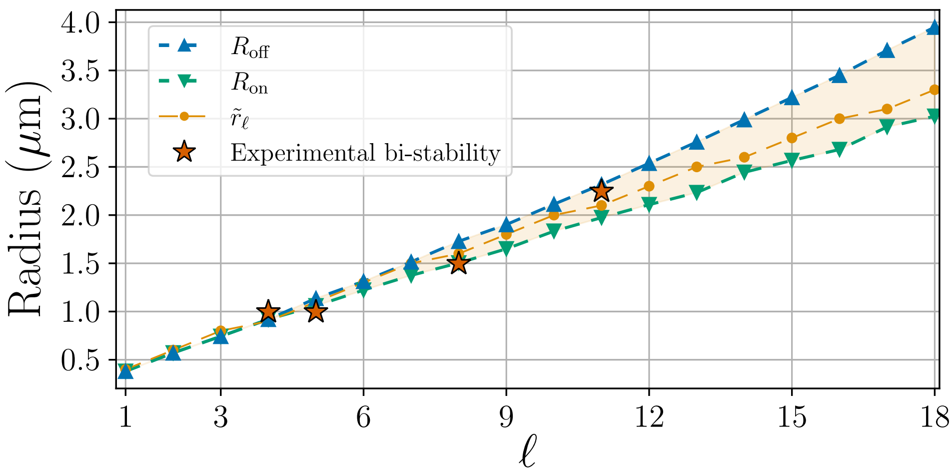

Figure 2.4: For an aberration-free trapping beam, the parameter space spanned by the microsphere radius and the topological charge ℓ is divided into three different regions. For radii smaller than the critical radius $R_{\rm on}(\ell)$ (green), on-axis trapping is excluded and the particle rotates around the optical axis along a circular trajectory (orbital trapping). For radii larger than the critical radius $R_{\rm off}(\ell)$ (blue), orbital trapping is excluded and the particle is trapped at a position along the optical axis. On-axis and orbital states co-exist in the (colored) bistable stripe bounded by the plots of $R_{\rm on}(\ell)$ and $R_{\rm off}(\ell)$. Such region corresponds to radii close to the maximum of electric energy density $\tilde{r}_\ell$ (circle). When an oil-immersion objective is employed, the spherical aberration introduced by refraction at the glass slide opens the way to switch between trapping regimes by changing the height L of the objective focal plane. However, we still find an overall qualitative agreement between the simplified aberration-free prediction and experimental realizations of bistability (star) provided that we fine tune the height L.

activated hopping between the two mesostates.

As an illustration of the different trapping regimes, we plot $Q_\rho(\rho, z = 0)$ versus ρ in Fig. 2.5 for three different microsphere radii: $a = 1.5\,\mu$m (blue), $2.25\,\mu$m (red) and $3.5\,\mu$m (green), taking $\ell = 11$ in all cases. We find the values for the critical radii to be $R_{\rm on} = 2.0\,\mu$m and $R_{\rm off} = 2.3\,\mu$m. Thus, the three radii considered in Fig. 2.5 illustrate the three trapping regimes shown in Fig 2.4. For the smallest size, Fig. 2.5 shows that the axial equilibrium position is unstable, as expected from Fig. 2.3, whereas the other root of $Q_\rho(\rho = 2.0\mu\text{m}) = 0$ corresponds to the orbital trapping state. For the largest particle, the only radial stable equilibrium position is at $\rho = 0$, whereas for the intermediate size, two stable equilibria are exhibited.

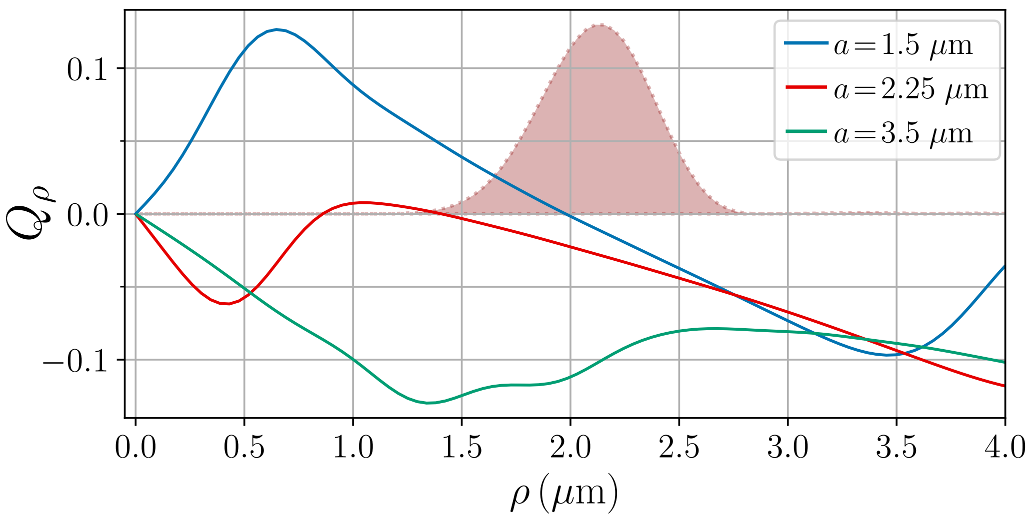

Figure 2.5: Radial optical force component Q_ρ as a function of radial position ρ for $\ell = 11$ and radii $a = 1.5\ \mu$m (blue), $a = 2.25\ \mu$m (red) and $a = 3.5\ \mu$m (green). The fill plot indicates the electric energy density variation with distance to the optical axis. Its maximum is located at $\tilde{r}_\ell = 2.1\ \mu$m.

For further insight, we also show in Fig. 2.5 the electric energy density as a function of ρ (fill plot). The edge of a microsphere with $a = 1.5\,\mu$m is located near the inner tail of the electric energy density distribution when its center is aligned along the axis. As it would sit almost entirely on the dark central part of the annular spot, stable on-axis equilibrium is indeed not possible in this case. On the other hand, a microsphere with $a = 3.5\,\mu$m encompasses the entire bright annulus when placed on-axis, which is consistent with stable on-axis trapping. Finally, the intermediate size microsphere ($a = 2.25\,\mu$m), for which a bistable behavior is predicted, is such that its edge nearly coincides with the energy density peak at $\rho = \tilde{r}_\ell$. Such discussion indicates that the width of the bistable stripe in the parameter space of Fig. 2.4 scales with the width of the focal spot annular region. As the latter increases with ℓ, we expect the bistable stripe to become wider as ℓ increases, which is indeed in agreement with the results shown in Fig. 2.4.

In this section, we presented only the aberration-free theory results, as it renders simpler and more didactic discussions. In the next chapter, we will present the experimental realization of a bistable trap and the theoretical comparison, using experimental parameters as numerical inputs. To model the experiment reliably, spherical aberration has to be accounted for. In the next chapter, we will show the importance of SA to "tune" the bistable configuration, first experimentally (Sec. 3.1) and then theoretically (Sec. 3.3).

In the bistable system, the sphere hops between each of the equilibrium states by thermal fluctuations alone. Additionally, the analysis of the experimental data requires an understanding of the dynamics of a colloidal particle. In the following section, we provide an introduction to the Langevin equation, which describes the stochastic dynamics of the particle in the trap, to facilitate the experimental data analysis in the next chapter. Discussions are made for systems in 1 dimension, while the extension to the 3-dimensional case is only discussed at the end. Lastly, a useful computational method to simulate the particle's Brownian dynamics is presented. The same computational method is used in the next chapter to simulate and provide further validation of our bistable system.

2.4 Langevin dynamics and experimental observables

Until this point we have discussed the physics of the deterministic optical force present in an OT. However, the microspheres used in the majority of OT experiments belong to a length scale where Brownian motion is an important part of the resulting dynamics. This characteristic random motion is explained by the interaction between the microscopic particle and the molecules of the media surrounding it. The dynamics of particles undergoing Brownian motion are described by the Langevin equation, which employs a stochastic force term representing the molecular collision interaction and a dissipative term accounting for the particle's kinetic energy loss due to drag. Interestingly, this is a signature of the fluctuation-dissipation theorem, where the drag exerted by the fluid converts the particle's kinetic energy to heat and the associated thermal fluctuation is responsible for the stochastic force.

We initiate the discussion by addressing the Langevin equation that describes our system and the necessary approximation we have to take to obtain it. From the 1-

dimensional case, we define the quantities of interest for a system embedded in a harmonic optical potential $U(z) = \frac{\kappa z^2}{2}$, which can be later generalized for higher dimensions and for arbitrary force fields.

The 1-dimensional Langevin equation describing the microsphere motion in the z direction reads:

$$m\frac{d^2 z}{dt^2} = -\frac{dU(z)}{dz} - \beta\frac{dz}{dt} + \sqrt{2\beta k_B T}\,\xi_t\,, \tag{2.38}$$

where m is the microsphere mass, $z = z(t)$ is the axial position as a function of the time t, β is the Stokes drag coefficient, k_B is the Boltzmann constant, T is the system temperature and ξ_t is the stochastic term (white noise) which has zero mean and is completely decorrelated for any $t' \neq t$, yielding:

$$\langle \xi_t \rangle = 0\,, \qquad \langle \xi_t \xi_{t+t'} \rangle = \delta(t')\,. \tag{2.39}$$

We chose the notation using a subscript t instead of $\xi(t)$ to denote that ξ_t is an element of a stochastic process (which will be properly defined at the end of this section) indexed by t, with dimension of $(t^{-1/2})$.

The Stokes drag coefficient β for a spherical particle embedded in a fluid and distant from any surface is given by the Stokes law:

$$\beta = 6\pi\eta a\,, \tag{2.40}$$

where η is the fluid viscosity and a is the radius of the sphere. A common situation in OT experiments is to trap microspheres near the sample chamber glass slide. The Faxén's correction to the Stokes law [28, 29] describes the drag coefficient β as a function of the height of the microsphere center with respect to the plane surface h:

$$\beta = \frac{6\pi\eta a}{1 - \frac{9}{16}\left(\frac{a}{h}\right) + \frac{1}{8}\left(\frac{a}{h}\right)^3 - \frac{45}{256}\left(\frac{a}{h}\right)^4 - \frac{1}{16}\left(\frac{a}{h}\right)^5}\,. \tag{2.41}$$

It is clear that we recover the Stokes law by taking $h \to \infty$ in eq. 2.41.

The first term in the r.h.s. of eq. 2.38 can be identified as the harmonic optical force $(-dU(z)/dz = (-\kappa z))$, and $(\frac{dz}{dt}) = \dot{z} = v$ as the particle velocity. A particle trajectory $z(t)$

and associated velocity $\dot{z}(t)$ obeying eq. 2.38 are called position and velocity time series, respectively. From each time series we can compute the corresponding auto-correlation function (ACF) $\mathcal{C}_f(t)$:

$$\mathcal{C}_z(t) = \langle z(t_0+t)z(t_0)\rangle \,,$$
$$\mathcal{C}_{\dot{z}}(t) = \langle \dot{z}(t_0+t)\dot{z}(t_0)\rangle \,. \tag{2.42}$$

The ACF of the position $\mathcal{C}_z(t)$ and velocity $\mathcal{C}_{\dot{z}}(t)$ provides two characteristic times: the position relaxation time $\tau = \beta/\kappa$ (also called the trap characteristic time) and the momentum relaxation time $\tau_m = m/\beta$ [30]. This is clearly illustrated by the position ACF of a particle trapped in a harmonic potential $U(z) = \frac{\kappa z^2}{2}$:

$$\mathcal{C}_z(t) \;=\; \frac{k_B T}{\kappa} e^{-|t|/\tau} \,. \tag{2.43}$$

From eq. 2.43, we can see that the position relaxation time τ can also be understood as the average time the particle takes to *'forget'* its initial position, *i.e.* the characteristic decay time of the position ACF. Therefore, the characteristic time τ divides the time scales of the diffusive regime, where $\delta t \ll \tau$, and the trap confinement regime, where $\delta t \gg \tau$. This is the reason why τ can also be understood as the trap characteristic time, since it is the time scale in which the harmonic optical force acts on the particle dynamics.

For the cases of our interest, the velocity relaxation time τ_m is orders of magnitude smaller than τ.[3] This ensures that any fluctuation of the particle velocity (which is directly related to its temperature) decays back to its initial value (or simply thermalizes) in the diffusive or confinement time scales $\delta t \gg \tau \gg \tau_m$. Therefore, the particle position evolves as a succession of equilibrium states, allowing us to define a Boltzmann probability distribution for the position z for each moment in time t. Also, the inertial term in eq. 2.38 ($m(\frac{d^2 z}{dt^2})$, receiving its name as it is proportional to the particle's mass) has a much smaller contribution than any of the remaining factors of the equation. If we drop the inertial

[3] Additionally, the momentum relaxation time divides the time scales of the ballistic ($\delta t \ll \tau_m$) and diffusive ($\delta t \gg \tau_m$) regimes.

term, we obtain the so-called overdamped Langevin equation:

$$\frac{dz}{dt} = -\frac{1}{\beta}\frac{dU(z)}{dz} + \sqrt{\frac{2k_BT}{\beta}}\,\xi_t\,. \tag{2.44}$$

As the system is in thermal equilibrium, we can define the position probability distribution (or probability density function, PDF) following the Maxwell-Boltzmann distribution for any given potential $U(z)$:

$$p(z) \;=\; Z^{-1}e^{-\frac{U(z)}{2k_BT}} \tag{2.45}$$

where $Z^{-1} = p_0$ is the normalization constant in terms of the partition function $Z = \int_{-\infty}^{\infty} dz\, e^{-U(z)/(2k_BT)}$. From a given PDF, we can also solve eq. 2.45 for the potential $U(z)$ by taking the natural logarithm of both sides, obtaining:

$$U(z) \;=\; -k_BT\,\log(p(z)) + U_0\,. \tag{2.46}$$

Note that this relation is valid for any potential $U(z)$, as the only condition we mentioned is that the system is in thermal equilibrium.

Assuming the potential in eq. 2.45 is harmonic, we can obtain a useful relation between the system temperature T, the harmonic trap stiffness κ and the position variance $s = \langle z^2\rangle$ (assuming the mean position to be $\langle z\rangle = 0$). The equipartition theorem states that each degree of freedom of a system in thermal equilibrium will possess an average energy of $(k_BT/2)$. Taking the position average of $U(z)$ and using the equipartition theorem, we obtain:

$$\langle U(z)\rangle \;=\; \frac{\kappa}{2}\langle z^2\rangle \;=\; \frac{1}{2}\,\kappa s \;=\; \frac{1}{2}\,k_BT\,, \tag{2.47}$$

meaning that $s = k_BT/\kappa$. Substituting eq. 2.47 into eq. 2.45, we obtain a PDF with the shape of a Gaussian function:

$$p(z) \;=\; p_0\,\exp\!\left(-\frac{\kappa\,z^2}{2k_BT}\right) \;=\; \frac{1}{\sqrt{2\pi s}}\,\exp\!\left(-\frac{z^2}{2s}\right), \tag{2.48}$$

where it is straight forward to identify the position variance as the width of the Gaussian distribution.

Now, we introduce the power spectral density (PSD) of the position time series as the Fourier transform (FT) of the ACF, defined in eq. 2.42. The Wiener–Khinchin theorem [31] allows us to calculate the PSD of a stationary stochastic process (which is not square-integrable) as the FT of the series ACF. It follows from the convolution theorem that the FT of the position ACF is given by:

$$\hat{\mathcal{C}}_z(t) \;=\; \hat{z}(f)\,\hat{z}(-f) \;=\; |\hat{z}(f)|^2\,, \tag{2.49}$$

where the symbol $(\hat{\ })$ denotes the FT of the quantities $\mathcal{C}_z(t)$ and $z(t)$.

An alternative approach to obtain the PSD is by directly taking the FT of the overdamped Langevin equation, which is specially useful for the harmonic potential case. Defining the the trap characteristic frequency (also called corner frequency) $f_c = 1/(2\pi\tau) = \kappa/(2\pi\beta)$, substituting into eq. 2.44 and taking its FT, we obtain:

$$2\pi\,(f_c - if)\,\hat{z}(f) \;=\; \sqrt{\frac{2k_BT}{\beta}}\;\hat{\xi}(f)\,. \tag{2.50}$$

We proceed by isolating $\hat{z}(f)$ and taking the square of its modulus. Using once again the Wiener–Khinchin theorem and the second relation in eq. 2.39, we find that $|\hat{\xi}(f)|^2 = 1$ and obtain the resulting position PSD $P_z(f)$:

$$P_z(f) \;=\; |\hat{z}(f)|^2 \;=\; \left(\frac{k_BT}{(2\pi^2)\beta}\right)\frac{1}{(f_c^2 + f^2)}\,, \tag{2.51}$$

which means that the PSD has the form of a Lorentzian function if the particle is inside a harmonic potential.

As a final topic of this section, we will briefly introduce the Ornstein-Uhlenbeck process along with its relation to the overdamped Langevin equation and the numerical method used to simulate the Langevin dynamics. A stochastic process is a collection of random variables indexed by a set, where each process is categorized according to its specific properties. An example with physical meaning is the white noise presented in eq. 2.38, which is modeled to have a Gaussian amplitude PDF and therefore is said to be a Gaussian process. It is modeled this way because the thermal force term arises from the molecular collisions with the particle within the fluid. As the molecules' velocities follow the Maxwell-Boltzmann distribution and the elastic collision force should be proportional to the molecular velocity, the thermal force should also follow a Gaussian distribution.

The overdamped Langevin equation 2.44 corresponds to the Ornstein-Uhlenbeck process:

$$dz_t \;=\; -\frac{\kappa}{\beta}\, z_t\, dt \;+\; \sqrt{\frac{2k_BT}{\beta}}\, \xi_t\, dt\,. \tag{2.52}$$

which is both a continuous-time Markov (*i.e.* "memoryless") and a Gaussian process, hence classified as a Gauss-Markov process. This means that the Ornstein-Uhlenbeck process PDF is given by a Gaussian function and the corresponding position time series z_t can be statistically characterized solely by a mean value $\bar{z}$ (usually set to zero) and a variance $s = \frac{k_BT}{\kappa}$. Therefore, it is useful to write z_t using the notation for Gaussian processes as $z_t \sim \mathcal{N}(\bar{z}, s)$.

The computational model used to simulate the related overdamped Langevin equation requires a discretization of the Ornstein-Uhlenbeck process in eq. 2.52, where the index t is turned into an integer and the time differential dt becomes a finite time interval Δt. However, the discretization of the white noise term is not a straightforward procedure, as the averages present in eq. 2.39 should be sums instead of integrals in time. Additionally, the new noise term w_t should have zero mean, unit variance and be delta correlated ($\langle w_t w_{t'}\rangle = \delta_{t,t'}$, where $\delta_{t,t'}$ is the Kronecker delta) for an arbitrary time interval Δt, where the operation $\langle\ \rangle$ denotes a sum over the time index set instead of an integral in time (representing the ensemble average). Therefore, we should substitute ξ_t by $w_t/\sqrt{\Delta t}$ to satisfy these conditions and obtain the discrete version of the Ornstein-Uhlenbeck process, given in terms of the position increment Δz_t:

$$\Delta z_t \;=\; z_{t+1} - z_t \;=\; -\frac{\kappa\,\Delta t}{\beta}\, z_t \;+\; \sqrt{\frac{2k_BT\,\Delta t}{\beta}}\, w_t\,. \tag{2.53}$$

According to this equation, the position time series z_t can be obtained recursively from the white noise process $w_i \sim \mathcal{N}(0,1)$ and an initial position state z_0, since $z_{t+1} = z_t + \Delta z_t$. Alternatively, one can rewrite eq. 2.53 using the Wiener increment ΔW_t, defined as:

$$\Delta W_t = w_{t+\Delta t} - w_t \sim \mathcal{N}(0, \Delta t)\,, \tag{2.54}$$

and are related to the white noise process as follows:

$$\Delta W_t = \sqrt{\Delta t}\; w_t\,. \tag{2.55}$$

Therefore, we can substitute eq. 2.55 into eq. 2.53, which leads to another quite common way of expressing the Ornstein-Uhlenbeck process:

$$\Delta z_t \;=\; -\frac{\kappa\,\Delta t}{\beta}\, z_t \;+\; \sqrt{\frac{2k_BT}{\beta}}\;\Delta W_t\,. \tag{2.56}$$

Finally, a few important remarks should be made to conclude this section. A straightforward implementation of eq. 2.53 is referred to as the Euler-Maruyama scheme, which is the most simple and intuitive way of solving stochastic differential equations like the Langevin equation. Numerical simulations based on this algorithm should employ time steps respecting $\Delta t \ll \tau$, which ensures that the simulated thermal force (proportional to w_i) is indeed uncorrelated for time intervals much smaller than the trap characteristic time.

Additionally, the Langevin equation 2.38 can be viewed simply as the second Newton's law with an stochastic thermal force term. This means that the optical force field we have assumed to be harmonic can actually take any form, like the force field of a bistable trap for example[4]. As force fields become more complicated, different solution schemes can be used to improve either the restrictions on the time step Δt or the convergence of the time series PDF. As an example, the class of the stochastic Runge-Kutta (explicit strong)

[4]If this is the case, the resulting stochastic process is not necessarily an Ornstein-Uhlenbeck process anymore, as the resulting position PDF may no longer be a normal distribution (*i.e.* Gaussian).

schemes [32] gained a lot of popularity due to their gain in overall time performance and therefore in relative computational cost. In ref. [32] an in-depth discussion on the mathematics of stochastic differential equations can be found (including introductions to Stochastic processes and Itô stochastic calculus), together with a full descriptions of the aforementioned solution schemes (Euler-Maruyama and Runge-Kutta of different convergence orders and dimensionalities) as well as others.

Lastly, the 1-dimensional Brownian dynamics we discussed in this section can be directly extended to 3-dimensions by considering a system of 3 independent Langevin equations, one for each Cartesian direction. As long as the thermal force intensity in each Cartesian component is normally distributed, the resulting 3-dimensional thermal force vector will exhibit an isotropic angular distribution[5]. Additionally, its intensity will be given by a chi-squared distribution with 3 degrees of freedom with variance equal to $\sqrt{6\,k_B T \Delta t/\beta}$ [33].

[5]For any other PDF distribution (other than Gaussian) of each individual thermal force component intensity, this angular isotropy is not guaranteed. Then, angular isotropy would have to be enforced while redefining the vector intensity distribution accordingly.

Chapter 3

Optical bistability on optical tweezers employing vortex beams

In the previous chapter, we presented fundamental topics on Optical Tweezers theory, optical trapping with vortex beams, and Brownian dynamics. Those topics are essential tools for the study of Optical Tweezers, and we shall summon them as needed throughout the next chapters.

In this chapter, I will discuss the optical bistability experiment made at the Optical Tweezers Lab at UFRJ and compare the theoretical and numerical results with the experimental data. The key difference from the system discussed in the last chapter is the presence of spherical aberration in the experimental system (see Fig. 3.1), introduced by the use of an oil immersion objective lens. This choice was not without reason: oil immersion objectives possess a significantly higher numerical aperture, which provides an overall better stability for the optical trap.

The spherical aberration phase in Eq. 2.4 arises from the refraction at the glass-water interface and is a function of the height L of the focal plane. This additional parameter enhances our control over the trapping field distribution and, thus, the optical force landscape. Indeed, the parameter L can be fine-tuned to switch between each of the three regions on the parameter space in Fig. 2.4 when the values of the microsphere radius a and topological charge ℓ fall within the bistability stripe.

The bistable trap system presented here exhibited great potential as a platform for demonstrating interesting aspects of stochastic thermodynamics [34, 35], such as non-equilibrium steady states (NESS), spontaneous symmetry breaking, and optical bistability. Another hot topic in stochastic thermodynamics is the search for protocols providing optimal shortcuts to thermalization in colloidal Brownian dynamics. Between September 2022 and March 2023, I was at the Institut de Science et d'Ingénierie Supramoléculaires (ISIS, located in Strasbourg, France) as a CAPES-Print fellow. There, I took part in a project involving the computer simulation and experimental demonstration of optimal finite-time thermalization protocols of colloidal single-particle systems[36]. Engaging in this project was a pivotal point in understanding the applications and possibilities that the bistable trap system provides to the area of stochastic thermodynamics.

We begin the discussions of this chapter by presenting the experimental realization of the bistable trapping system. Then, we present the experimental results and a theoretical comparison of the data using numerical analysis of the optical force landscape. Lastly, we present a simulation of the dynamics of a Brownian particle embedded in a bistable trap, which qualitatively agrees with the experimental observation.

3.1 Experimental setup and procedure

In this section, I'll present the experimental setup and the relevant elements and procedures present in the bistable trap project. As shown in Fig. 2.4, we found 4 cases of optical bistability experimentally. We will present the setup with all cases in mind, though we will later focus on the case with $\ell = 8$ and sphere radius $a = 1.5\mu$m.

3.1.1 Experimental setup

The main objective of the experimental setup we are about to discuss is to produce a vortex beam with a chosen topological charge ℓ and circular polarization state defined by σ that overfills an objective lens and thus creates an optical trap. During the description of the setup we will present and discuss each of the relevant optical elements used to build the trap.

The first step to creating the vortex beam is to steer a TEM_{00} laser beam onto a spatial light modulator (SLM). The laser is a diode-pumped Ytterbium fiber laser IPG photonics, model YLR-5-1064LP, which produces a linearly polarized collimated Gaussian mode with waist $w_0 = (2.2 \pm 0.2)\,\mathrm{mm}$ and wavelength $\lambda_0 = 1064\,\mathrm{nm}$. The SLM is a phase-only spatial light modulator made by Holoeye Photonics, model AG Pluto, and requires the incident laser beam to be horizontally polarized in order to imprint the phase into it.

An SLM is a liquid crystal display (LCD) in which each pixel can be electronically controlled to change the refraction index inside the cell, imprinting a local phase on the light beam. The added phase of each pixel corresponds to a grayscale 8-bit integer value, and the data array for every pixel on the display can be encoded in one color channel of an image file, which is called a phase mask.

We employ the lossless modulation technique [37], in which the SLM displays the overlapped phases of a vortex with topological charge ℓ ($\Phi_{\mathrm{vortex}} = \ell\phi$) and a linear ramp ($\Phi_{\mathrm{ramp}} = A\,x$), where the latter separates the different orders of diffraction. Here, Φ_{vortex} is the resulting vortex phase, ϕ is the angular polar coordinate (in the transverse plane frame) and Φ_{ramp} is the resulting ramp phase corresponding to a triangular prism with its phase slope along the x direction and with angular coefficient A. Each diffraction order corresponds to a number of round trips inside each of the SLM pixels, with $n = 0$ meaning the portion of the initial beam that reflected on the SLM first surface and suffered no phase modulation, $n = 1$ being the portion that got transmitted into each pixel and suffered no internal reflection on the way out, and each consecutive order having suffered an extra internal reflection when exiting the pixel, adding to the number of round trips. The ramp phase tilts each order with a different angle, thus separating them.

Therefore, in order to align an SLM, one should place it on the optical path so that the incident beam is close to normal incidence with the LCD plane (with angle tolerance

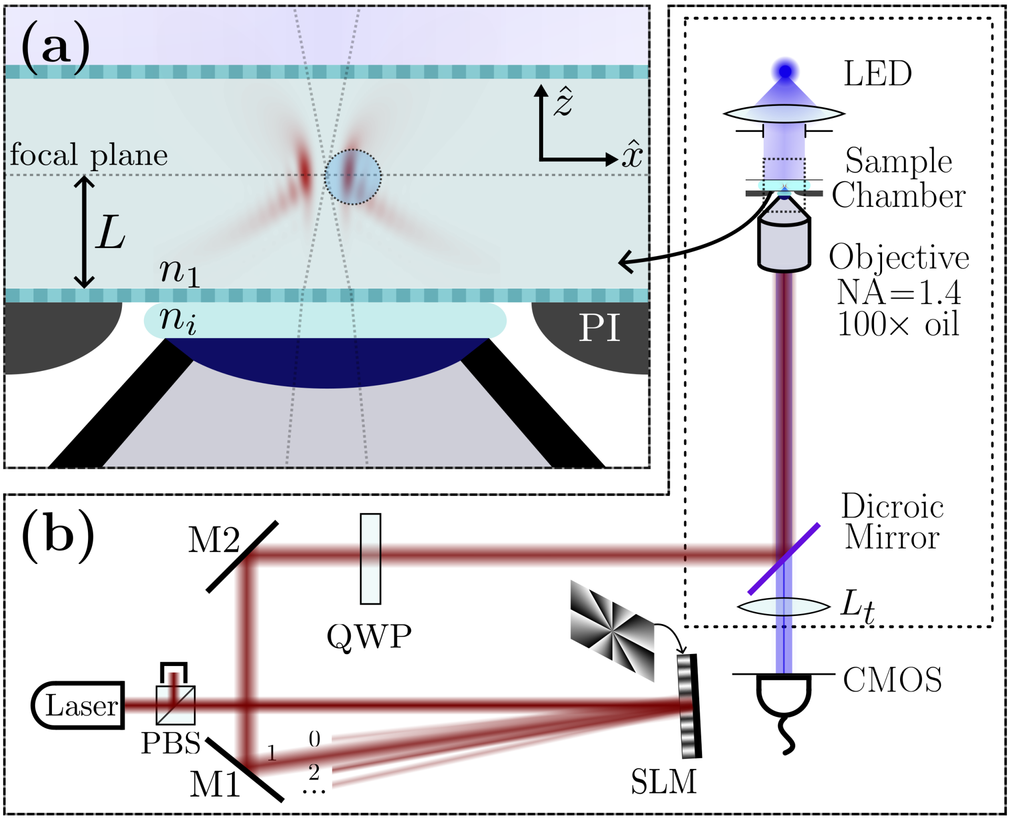

Figure 3.1: Illustration of the experimental setup. The top left panel shows a magnified view of the sample region with the glass slide lying at its bottom. The bottom panel shows the optical setup, in which the laser beam passes through a polarizing beam splitter (PBS) and is directed to the spatial light modulator (SLM). The first order of diffraction propagates through a quarter-wave plate (QWP) and then is steered onto the microscope (dotted frame). Inside the microscope, the beam is reflected by a dichroic mirror (DM) and then focused by an oil-immersion objective (NA $= 1.4$, $100\times$ magnification). Inside the sample chamber, the refractive index mismatch between the glass slide (index n_i) and the aqueous medium filling the chamber (index n_1) leads to the introduction of a spherical aberration phase upon refraction at the interface between the slide and the water. Such phase is proportional to the height L of the objective focal plane with respect to the glass-water interface, whose position is controlled by a piezoelectric nanopositioning stage (PI). The resulting non-paraxial focused beam is indicated by the density plot of the electric energy density for $L = 10\,\mu$m (red), along with a trapped microsphere of refractive index n_2.

or other requirements specified by the SLM manufacturer). The tilt angle is then chosen so that the different diffraction orders can be clearly separated along the following optical path. As shown in Fig. 3.1, we propagate only the first order of diffraction through a quarter-wave plate (QWP) to produce a left-handed circular polarization vortex beam. The circularly polarized vortex beam is then directed to an inverted microscope, where it is reflected by a dichroic mirror into the objective lens (Nikon PLAN APO, 100x, NA = 1.4 with aperture radius $R_p = (2.80 \pm 0.05)\,\mathrm{mm}$). We check the transverse profile of the vortex beam with the help of a scanning-slit beam profiler (Thorlabs BP209-VIS/M) and a non-polarizing beam splitter placed right before the microscope entrance (not depicted). The resulting $\ell = 8$ (also $\ell = 11$) naturally overfills the objective entrance port, while other cases ($\ell = 4$ and $\ell = 5$) require the resulting vortex beam to be expanded with a telescope to properly overfill the objective aperture.

An important aspect of setups that employ SLMs is the effect of reflection on the transverse amplitude and phase profiles of the beam. Upon reflection, the transverse plane coordinate system inverts the coordinate axis parallel to the scattering plane, which, in general, does not affect azimuthally symmetric beams. However, while the transverse field intensity profile is azimuthally symmetric for a vortex beam, the phase profile is not. This means that upon each reflection, the vortex beam topological charge will flip its sign. We account for this effect by adapting the initial sign of ℓ displayed on the SLM, and the resulting charge can be easily verified by examining the reflected image of the non-paraxial beam emerging from the back focal plane of the objective. The reflected image of a left-handed (right-handed) circularly polarized vortex beam will exhibit a larger (smaller) ring radius $\tilde{r}_\ell$ if the sign of ℓ is positive or a smaller (larger) $\tilde{r}_\ell$ if ℓ is negative, in accordance with sec. 2.1.3.

The production of vortex beams with the lossless modulation method results in a mode that differs from the usual $\mathrm{LG}_{0\ell}$ mode we have discussed previously. In order to produce a $\mathrm{LG}_{0\ell}$ mode using the SLM the amplitude modulation method should be employed, where the field amplitude profile of the desired $\mathrm{LG}_{0\ell}$ should be superposed with both the vortex and ramp phases. As the resulting $\mathrm{LG}_{0\ell}$ beam is a solution of the paraxial equation, the usual paraxial parameters and equations define the electromagnetic field. On the other hand, the transverse field intensity and phase profiles of vortex beams produced with lossless modulation depend on the topological charge ℓ and the distance the field propagates. Therefore, the complex electromagnetic field can only be obtained by numerical evaluation of the Fresnel diffraction integral. Nevertheless, the paraxial r_ℓ parameter can be defined for both cases, thus making the whole discussion regarding the filling criteria still valid for vortex beams different from the $LG_{0\ell}$ mode used throughout section 2.1.

Additionally, the alignment of the incident beam optical axis and the modulation mask center is of great importance. A misalignment between an input Gaussian TEM_{00} beam and a phase-only mask (without amplitude modulation) will result in an asymmetrical vortex beam, where the intensity along the direction of the misalignment will be shifted towards the ring section closer to the beam side, forming a lump. The resulting optical trap may not exhibit a proper orbital motion depending on the severity of the misalignment, as the sphere might be locked in the intensity clump due to a gradient force component.

On the other hand, the amplitude modulation method can be designed to expect an arbitrary input field distribution. Amplitude modulation can be easily understood as a mask overlay with values ranging from 0 to 1, where 0 leads to no modulation and 1 to full modulation, superposed with the ramp phase. By setting this overlay to 0.5 everywhere, the output field's first diffraction order will have its total intensity cut in half. This means that this overlay can be set according to the input field at each coordinate point by dividing the overlay value by the relative field amplitude at that point (as long as it is not zero), and the whole overlay should be re-scaled so that its maximum value is 1. Given that the input field spatial distribution is aligned to the overlay, a new range of possibilities arises from this technique (aside from producing $LG_{0\ell}$ modes), such as dislocating the output field optical axis, resizing (diminishing) the beam waist of an input TEM_{00} Gaussian mode and creating multiple beams with controllable sizes and relative strengths.

The amplitude modulation technique plays an important role in other projects contained in this thesis. For example, the project presented in appendix A (Sec. A.1) uses the amplitude modulation technique to provide a better control of the input paraxial beam on the objective lens entrance, which greatly impacts the agreement between the theory and the resulting experimental data [38]. Also, this technique can be used to produce other kinds of structured beams, like cylindrical vector beams, which are discussed in chapter 4. Therefore, it seems appropriate to mention it in the present section due to its context, but for now, we should shift our focus back to the bistability experiment.

For the case ($\ell = 8$, $a = 1.5\mu$m), the overfilling of the objective entrance port of radius is such that the ratio between the maximum intensity and the objective lens aperture radii is $r_\ell/R_p = (0.68 \pm 0.01)$. Though this is not in accordance with the previously established overfilling condition $r_\ell/R_p = 0.8$, one can see in Fig. 2.1 that $\ell = 5$ and $\ell = 10$ are already close to the diffraction-limited size.

The imaging setup we used in the experiment is provided by a high-end Nikon Eclipse microscope, where the data acquisition process is carried out via video microscopy. The microscope employs a Köhler illumination scheme, where an LED source (wavelength 470 nm, depicted in Fig. 3.1), along with a pair of collector and condenser lenses and diaphragms, produces a plane wave on the sample. Light scattered by the microspheres is then collected by the objective and goes through the dichroic mirror and the microscope tube lens L_t. The Köhler illumination and the imaging schemes are discussed thoroughly in references [6, 39, 40]. The resulting images consist of interference patterns formed by the incident and scattered light fields, characterized by concentric contrast rings (see Fig. 3.2 panels (a)-(d)). The images are recorded by a CMOS camera (Hamamatsu Orca-Flash 2.8 C11440-10C) with an acquisition rate varying between 50 fps (for the cases $\ell = 4, 5$) and 30 fps (for the cases $\ell = 8, 11$). Finally, the microsphere center-of-mass position on the (x, y) plane can be obtained for each frame of a video by applying a threshold on the grayscale image.

3.1.2 Experimental procedure

The sample chamber is contained by an O-ring on top of the glass slide and filled with a suspension of polystyrene microspheres (Polysciences, Warrington, PA) in water. By viewing the camera live feed, we can manually steer the sample to place a microsphere near the tightly focused Gaussian beam until trapping occurs. Once a microsphere is trapped, we raise the sample chamber until the sphere 'touches' the glass-water interface. This procedure is useful to estimate the relative distance between the interface and the objective focal plane, as the Gaussian mode has a higher waist w_0 (and therefore the larger Rayleigh length) compared to the resulting vortex modes. This procedure is further explained and motivated in appendixes C and A of reference [41], respectively.

To achieve the bistable trap, we set the topological charge on the SLM to comply with the selected microsphere size, according to the phase diagram in Fig. 2.4. Although the results of Fig. 2.4 were obtained considering an aberration-free system, they still seem to hold true for our experimental setup employing an oil-immersion objective, therefore providing a useful guide for achieving a bistable trap. Indeed, we indicate the experimental implementations of optical bistability as stars in Fig. 2.4, where values of the particle radius a and topological charge ℓ fall inside (or at least very close to) the bistable stripe, but not otherwise. For each case, we are able to experimentally achieve a thermally-activated bistable optical trap by fine-tuning both the focal plane height L and the laser power P_{port} at the objective entrance port. Table 3.1 summarizes the values for the particle radius a, the topological charge ℓ, and the laser power P_{port} used to achieve bistability for each case.

In all of those cases, we start by trapping the microsphere on the axis with the focal plane close to the glass slide. The sample chamber is then lowered by a piezoelectric nanopositioning stage (Digital Piezo Controller E-710, Physik Instrumente), increasing the distance L between the glass slide and the objective focal plane as depicted in Fig. 3.1. As we keep lowering the sample chamber, we reach the bistable region, where the microsphere starts to hop between on-axis and orbital trapping. The bistable regime is present in a finite L range, as if we lower the sample chamber further, on-axis trapping ceases to occur. This indicates that increasing the value of L corresponds to shifting the bistable stripe upwards, as the axial trapping occurs for lower values of L and orbital trapping for greater values of L. For $\ell = 8$ and $a = 1.5\mu$m we observe a sample chamber displacement range of 4μm separating the axial and orbital trapping states, which corresponds to a range for L as $\Delta L = N_a\, 4\mu\text{m} \approx 3.5\mu$m.

3.2 Results for the bistability experiments

In this section, we will discuss the results of the bistability case $\ell = 8$ and $a = 1.5\mu$m with more detail. This particular case was the clearest bistability demonstration we have achieved and also the easiest to analyze among the total four. Additionally, less detailed experimental data of the remaining cases will be presented.

We captured 3 sets of videos for the case $\ell = 8$ and $a = 1.5\mu$m: one video for the intermediate bistable configuration, one for an L value right below, and another right above the bistable L range. The analysis of the bistable trapping video is summarized in Fig. 3.2. The alternation between on and off-axis states over time is depicted in Fig. 3.2 panels (a)-(e). In panel (e) we plot the microsphere radial position ρ versus time, whereas 4 frames of the corresponding video illustrating a 'round trip' of states hoping (axial to orbital and back to axial) are indicated as vertical lines and displayed in panels (a)-(d). The orange dashed outline represents the sphere size and serves as a scale. Along the orbital trajectory, the sphere motion blurs the resulting image along the mean displacement direction (represented as a black arrow in panels (b) and (c)). The diffraction rings composing the sphere image also depend on the relative height to the focal plane, and the clear difference between the image patterns (a) and (d) for on-axis trapping and (b) and (c) for orbital motion indicates [42] that each state corresponds to

ℓ	$a\,(\mu\mathrm{m})$	$\rho_{\mathrm{theo}}\,(\mu\mathrm{m})$	$\rho_{\mathrm{exp}}\,(\mu\mathrm{m})$	$T_{\mathrm{exp}}\,(\mathrm{s})$
4	1.0	–	0.6 ± 0.1	0.24 ± 0.02
5	1.0	0.69 ± 0.01	0.7 ± 0.2	0.20 ± 0.01
8	1.5	1.07 ± 0.01	1.0 ± 0.2	0.55 ± 0.03
11	2.25	1.2 ± 0.1	1.9 ± 0.3	5 ± 1

Table 3.1: Experimental values for the radius ρ_{exp} and period T_{exp} of the orbit state in the bistable regime. The theoretical values for the orbit's radius ρ_{theo} (to be discussed in the next subsection) are in good agreement with the experimental data for $\ell = 5$ and $\ell = 8$, but for $\ell = 4$ only on-axis trapping is predicted by the model.

a different height.

From the radial time series in panel (e), we also determine the radius of the orbit ρ_{exp} from the average (horizontal dashed line) and the standard error of ρ in the orbital state. We represent the resulting measured values of ρ_{exp} for $\ell = 8$ as well as for the other values of ℓ in Table 3.1.

In panel (f) of Fig. 3.2 we show the energy distribution $U(x, y)$ in the xy plane in terms of the position probability distribution $p(x, y)$, following the Mawell-Boltzman definition of the optical potential $U(x, y)/(k_{\mathrm{B}}T) = \ln p(0, 0) - \ln p(x, y)$, as discussed in Sec. 2.4. The position probability distribution $p(x, y)$ is obtained by taking bins of area $\Delta x \Delta y = 1.35 \times 10^{-3}\,\mu\mathrm{m}^2$ from the total 4000 frames of the video (which corresponds to a total elapsed time of 133 s at 30fps).

and with different widths as determined by the total time elapsed in each orbital motion before hopping back to the axial trapping position. The period T_{exp} is then obtained from the peak of the PSD as indicated in Fig. 3.2(g). The resulting measured values of T_{exp} are shown in Table 3.1, with the error bars derived from the half width at half maximum.

In addition to the probability distribution, we also analyze the PSD for each coordinate of the microsphere position. Since both x and y coordinates provide very similar results, only the first is depicted in Fig. 3.2(g). The PSD has the form of a superposition of squared sinc functions centered at the orbital frequency $f_{\mathrm{exp}} = 1/T_{\mathrm{exp}}$, where T_{exp} is the

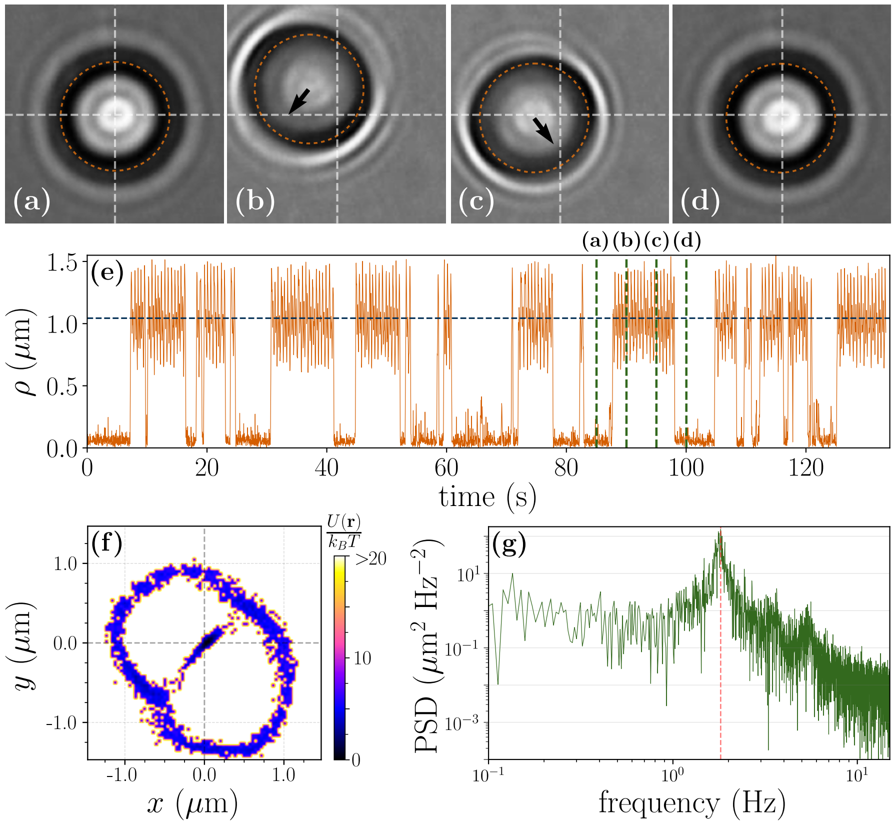

Figure 3.2: Experimental data corresponding to the realization of bistability with a polystyrene microsphere of radius $a = 1.5\,\mu$m and a vortex beam with $\ell = 8$. Panels (a)-(d) show frames of the trapped microsphere at times $t_{(\mathrm{a})} = 85\,$s, $t_{(\mathrm{b})} = 90\,$s, $t_{(\mathrm{c})} = 95\,$s and $t_{(\mathrm{d})} = 100\,$s. The outline (dash) of the trapped microsphere of diameter $D = 3\,\mu$m is superimposed on each image to represent the scale. When the microsphere hops to an off-axis location (b and c), it circulates around the axis. The black arrows indicate the motion of the microsphere in (b) and (c). The difference between the image patterns (a)-(d) and (b)-(c) indicates that the trapping height changes when hoping from axial equilibrium to orbital motion. Panel (e) shows the time series of the microsphere radial coordinate. The vertical green lines indicate the times corresponding to the frames shown in (a)-(d). The horizontal dashed line in panel (e) represents the mean radial coordinate $\rho_{\mathrm{exp}} = (1.04 \pm 0.05)\,\mu$m for the orbital trapping. Panel (f) shows a color map of the energy distribution $U(x, y)/(k_{\mathrm{B}}T)$ across the xy plane as derived from the position distribution density $p(x, y)$. Panel (g) is the power spectrum density (PSD) of the x coordinate showing a peak at $f = 1.82\,$Hz, which corresponds to an orbital period $T_{\mathrm{exp}} = (0.55 \pm 0.03)\,$s.

period of the orbit. This is easily demonstrated by considering eq. 2.49 for a truncated sine function, *i.e.* the product of a sine function with a square pulse. The FT of a square pulse (denoted by the product of two Heaviside theta functions $\Theta(t)\Theta(t + t')$, with width t') is

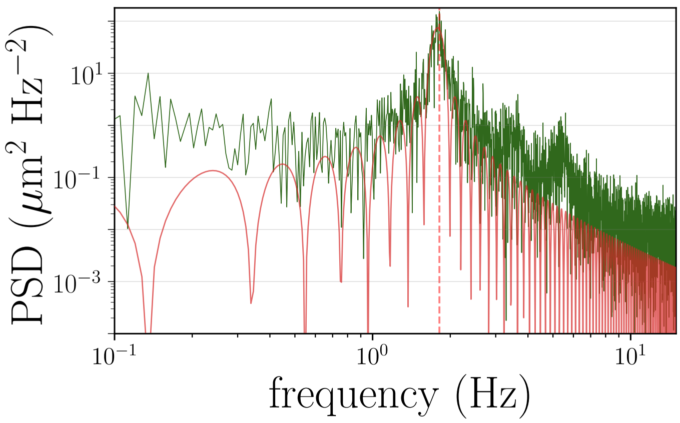

Figure 3.3: Resulting plot of the squared sinc function for one single round trip, depicting the qualitative behavior of a PSD for the bistable trapping case.

the sinc function, while the multiplying sine can be viewed as a translation of the sinc function in the frequency space. Therefore, different widths of the squared sinc functions are determined by the total time t' elapsed in each orbital motion before hopping back to the axial state. The period T_{exp} is obtained from the peak of the PSD, as indicated in Fig. 3.2(g) by the red dashed line, and its measured values are shown in Table 3.1 for each experimental case, with the uncertainty defined as the half width at half maximum of the function. Additionally, the axial trapping contribution to the PSD will be the usual Lorentzian function, which can't be visualized in Fig. 3.3 since the corner frequency is located beyond the Nyquist frequency for the experimental data.

On top of experimentally demonstrating the optical bistability, measurements of the occupation time and hopping probabilities are novel observables that depend on the optical potential and the non-conservative components of the optical forces. This presents yet another way to investigate the physical properties of the system, like the viscosity and drag coefficient of the surrounding fluid and light-matter interactions between the trapped particle and the optical beam, to name a few. Note that the robustness of the theoretical model is key to enabling such investigations, and even if we disregard the effect of astigmatism and other beam imperfections, an overall good agreement is found between the experimental measurements and the numerical simulation of the experiment.

As a final remark concerning our experimental results, we observed that the sense of rotation in every orbital state coincides with the sign of ℓ. Indeed, this is in agreement with a previous experiment of an optical trap employing vortex beams with aqueous colloidal suspensions [25]. However, a negative optical torque, *i.e.* a torque with an opposite sign between ℓ and the rotation handedness (given by the azimuthal force component), was predicted for the orbital motion of a particle suspended in air [43][1]. A negative torque was also demonstrated in a previous experiment by the LPO group, both experimentally and theoretically (using the MDSA formalism), for a particle trapped on-axis by a circularly-polarized Gaussian beam [44]. Likewise, our theoretical description of the optical trap experiment with vortex beams also confirms that the sense of rotation coincides with the sign of the topological charge.

3.3 Numerical results with MDSA theory

In this subsection, we will conduct theoretical and numerical analysis of the experimental results from the bistable system. We begin by demonstrating the role of spherical aberration in the intensity distribution of the field in the focal region. Next, we analyze the force field configurations as a function of the spherical aberration parameter. Finally, we present the results of a Langevin equation simulation for a bistable force field with parameters similar to those in the experimental realization.

3.3.1 The role of spherical aberration on the optical force landscape

When focusing a beam through the glass-water interface, the resulting spherical aberration phase drastically modifies the field distribution and, consequently, the optical force in the focal region. One of the effects is the formation of caustics, which are re-

[1] Additionally, this article also analyses the motion of a particle in the damped regime, where the simulated motion exhibits patterns which strongly depends on the air pressure and the initial conditions of the trapping system.

gions of local intensity maxima formed around the focal region. Experimental trapping results using Gaussian beams demonstrate this beam modification effect by presenting configurations with multiple equilibrium positions along the optical axis [8, 45].

A key point to our discussion is that the spherical aberration phase shows a dependence on theta, resulting in a more intense effect for marginal Fourier components (with larger theta). For this reason, the effect of spherical aberration on vortex beams that satisfy the overfilling condition is expected to be more intense than for beams localized close to the optical axis, such as the fundamental Gaussian mode.

In Fig. 3.4, we can observe the field intensity distribution for different values of L. As the amount of SA (quantified by L) increases, caustics start to form and become increasingly sharp. We can also see the elongation in the z direction of both the innermost (principal) ring as well as each of the caustics (secondary rings). A trivial result from the formation of caustics is that one can expect dipole particles to be trapped in any of the secondary maximum intensity rings, allowing for multi-stability systems.

A more subtle aspect, yet extremely important for controlling the onset of bistability, is the effect of SA on the size of the ring of maximum intensity $\tilde{r}_\ell$. As the amount of SA increases, the diffraction focus begins to occur in progressively lower z planes. When analyzing $\tilde{r}_\ell$ at the diffraction focus, we see that its value increases along with the amount of SA. Given the relationship between the ring radius and bistability control, we can state that this is an important mechanism for controlling its emergence.

3.3.2 Theoretical modeling and numerical results

In this subsection, we will discuss the numerical results related to modeling our experimental system. We used input parameters in the theory obtained from the experiment whenever possible. Discussions regarding the role of SA for optical force and how the parameter that quantifies it can be determined will be emphasized.

In Fig. 3.5(a), we plot the electric energy density (field intensity distribution) and

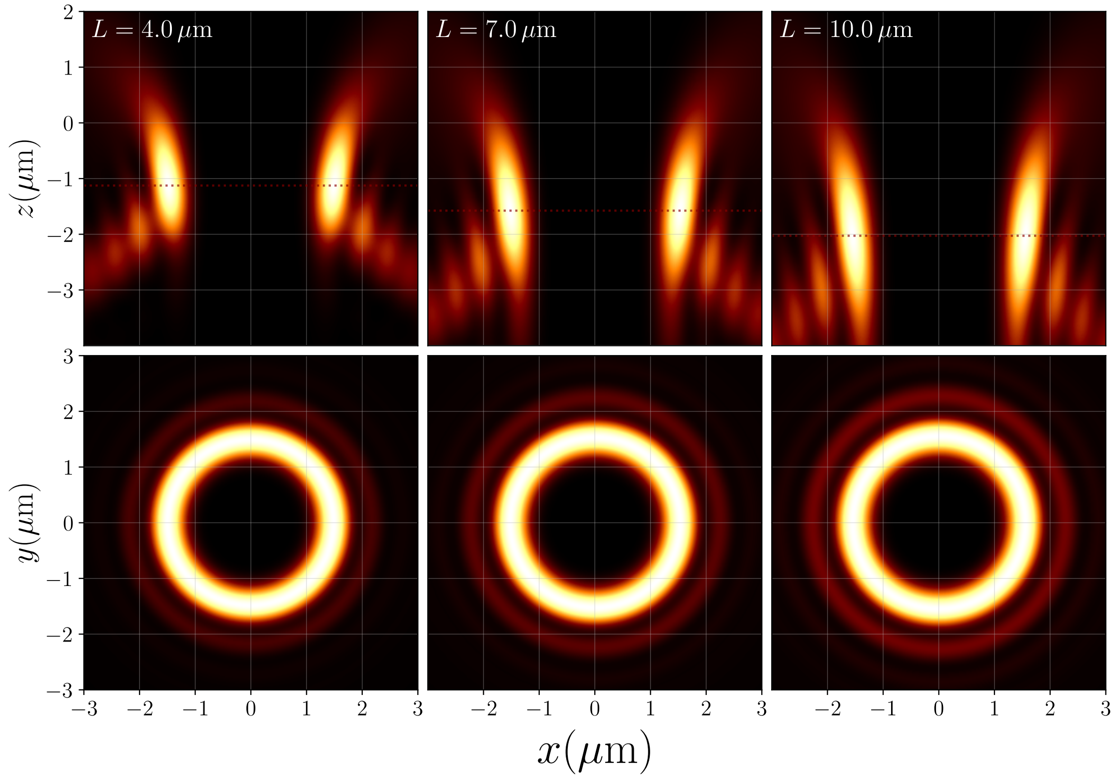

Figure 3.4: Illustration of the effect of the spherical aberration phase on the spatial distribution of the electric field intensity. The paraxial beam at the objective entrance (oil-immersion, NA= 1.4) is left-circularly polarized ($\sigma = 1$), has topological charge $\ell = 8$ and filling ratio $r_\ell/R_p = 0.8$. Each column corresponds to a distinct value of L, indicated in the upper left corner of each plot in the first row. The plane where the global intensity maximum is located is called the diffraction focus, which corresponds to the plots in the xy-plane (bottom row) and which we mark with a red dotted line in the xz-plane plots (top row).

dimensionless optical force components for different values of L, taking again $\ell = 8$ and $a = 1.5\,\mu$m. The values of L were chosen so that the 3 different trapping configurations are seen. The density plots in Fig. 3.5(a) depict the field intensity distribution (E^2, first row) and the axial (Q_z, second row) and radial (Q_ρ, third row) dimensionless optical force (efficiency factor) components in the (ρz) plane of the microsphere coordinate. The columns correspond to the three values of L, which quantifies the amount of spherical aberration of the focal field and increases in value from left to right.

When considering a collimated (aberration-free) input paraxial beam, the value of L (after focusing) corresponds to the position of the objective focal plane with respect to the glass slide. However, the experimental setup allowed the paraxial beam emerging from the SLM to propagate freely while acquiring a finite curvature radius. In other words, the vortex beam entering the objective lens possesses a quadratic diverging phase (defocus). It follows from the displacement theorem [46] that the defocus phase will shift the paraxial focal plane in the forward axial direction, hence decoupling the value of L from the distance between the focal plane and the glass-water interface (see ref. [41] section IV-C for more details).

Each column in Fig. 3.5(a) corresponds to an additional displacement of the focal plane by steps of $\Delta L = N_a d = 1.75\,\mu$m, thus mimicking the experimental procedure described in the previous section (3.1). As stated previously, E^2, Q_z, Q_ρ and $U(\rho)$ (in Fig. 3.5(b)) are independent of ϕ by symmetry.

We can use the density plots of the optical force components to identify the roots $Q_\rho = 0$ and $Q_z = 0$ that lead to stable trapping. Blue- and red-colored values within the maps of Q_z and Q_ρ denote positive and negative signs of the optical force value, respectively. In other words, blue (red) regions on the Q_z and Q_ρ maps indicate that the force component points to the positive (negative) z and ρ directions, respectively. Therefore, blue and green curves on the Q_z and Q_ρ maps represent the stable roots of each force component. Finally, their intersections are the stable equilibrium points in the ρz-plane (independent of ϕ by symmetry) and are plotted on top of the energy (E^2) density plot. Intersections at $\rho = 0$ correspond to axial trapping states, while at $\rho \neq 0$ correspond to orbital trapping states.

The configuration depicted in the first column of Fig. 3.5(a) represents the aberration-free case ($L = 0$), where we can see that both axial and orbital trapping states are present as the blue and green curves intersect twice, on- and off-axis. This is in accordance with the result of Fig. 2.4 since the parameters ($\ell = 8, a = 1.5\,\mu$m) are situated within the bistable stripe. However, experimental results indicate that the axial trapping state will be preferred in that case, while bistability will occur exclusively within a finite range of

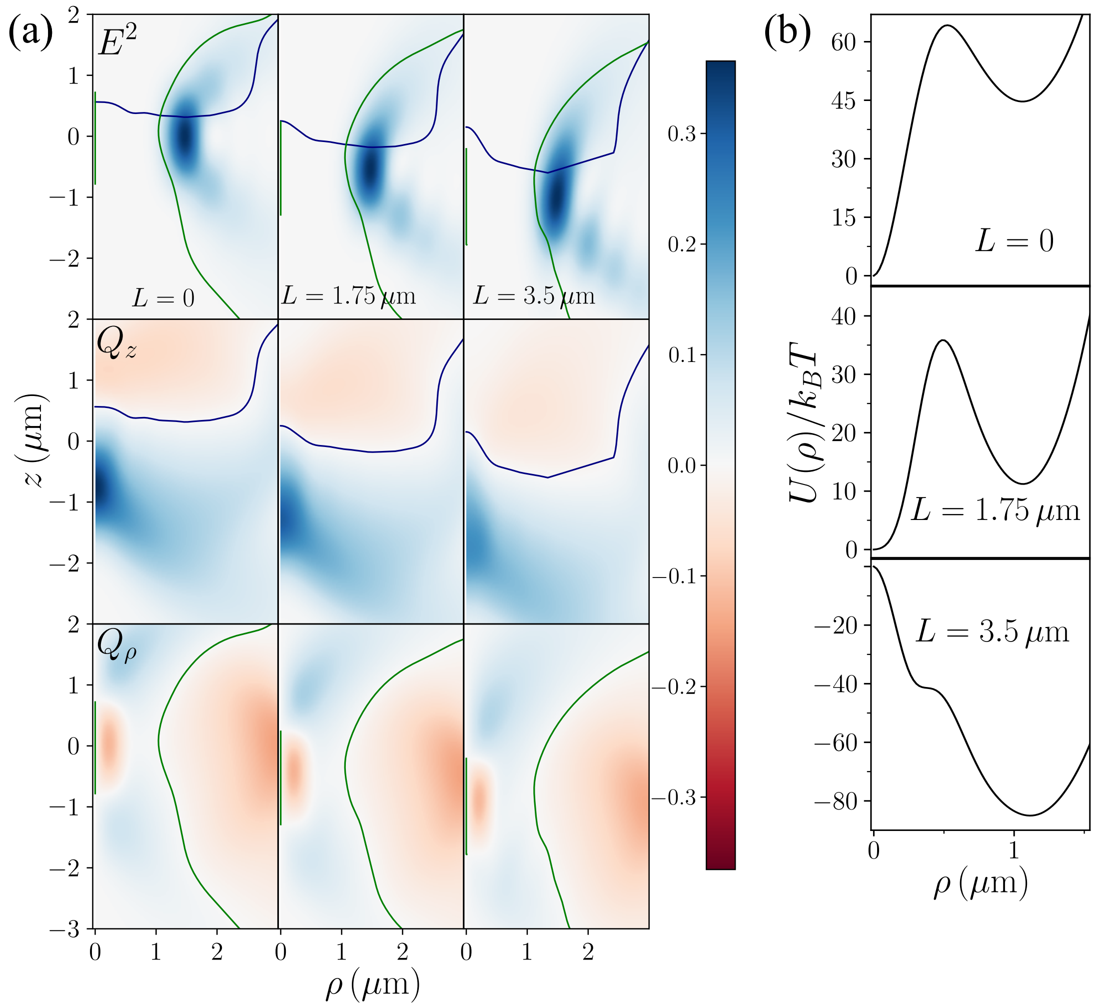

Figure 3.5: Variation of the optical force field with spherical aberration. The distance L between the objective focal plane (for paraxial rays) and the glass slide is increased from left to right, thus enhancing the spherical aberration introduced by refraction at the interface between the slide and the sample. A vortex beam with $\ell = 8$ and left-handed circular polarization ($\sigma = +1$) is focused by an oil-immersion objective so as to trap a polystyrene microsphere with radius $a = 1.5\,\mu$m. (a) From top to bottom, density plots representing the electric energy density E^2, and the axial and radial force components, Q_z and Q_ρ, respectively, on a meridional plane. The force components are normalized by eq. 2.33, and their values are indicated by the color bar. The blue and green lines indicate the roots of $Q_z = 0$ and $Q_\rho = 0$, respectively, that lead to stable 3D trapping when they intersect. (b) Optical potential (in units of the thermal energy k_BT) versus radial distance ρ.

values for L. This behavior can be explained with the aid of the effective optical potential, defined as:

$$U(\rho) \equiv -\int_0^\rho F_\rho(\rho, \bar{z}(\rho))d\rho\,, \tag{3.1}$$

where $\bar{z}(\rho)$ is the stable axial coordinate curve (blue curves in Fig. 3.5(a)). In order to calculate the radial force component F_ρ, we consider the expressions for Q_ρ and Q_ϕ given in subsection 2.2.2 and determine the power at the sample $P = 3.8\,\mathrm{mW}$ from the period of rotation (see sec. A.2 for the derivation of the period, and Appendix C of reference [41] for a detailed guide of the entire procedure).

We plot the effective potential energy in Fig. 3.5(b) for each value of L. Even though two intersections (axial and orbital) are present in the cases $L = 0$ and 1.75μm, the double potential well in each case is drastically different. The case $L = 0$ shows a deeper potential well for the axial trapping state compared to the off-axis minimum. Additionally, a high potential barrier divides the two potential minima, which implies that on-axis trapping will be favored over the orbital state. In case $L = 1.75\mu$m, the lower potential barrier and similar potential energy for axial and orbital trapping allow both mesostates to coexist in this configuration. Finally, the case $L = 3.5\mu$m depicted on the third column of Fig. 3.5(a) and the third line in panel (b) exhibits only orbital trapping, which is also in accordance with our experimental observations.

By comparing the experimental potential distribution shown in Fig. 3.2(f) with the potential for $L = 1.75\mu$m in Fig. 3.5(b) we find that the theory overestimates the relative difference between the potential minima by a factor of ~ 2. Note that the potential energy defined in eq. 3.1 is proportional to the power P_{port} at the entrance port. During the experiments, we observed that the bistable behavior disappeared as the laser power was increased. As a consequence, on-axis trapping was preferred, which is in agreement with the theoretical result that the potential energy minimum at $\rho = 0$ becomes even lower than the off-axis one for $L = 1.75\mu$m as the laser power increases. Cases with L values above the bistable range exhibit exclusive orbital trapping independently of the laser power, which only affects the period of rotation.

The probability density distribution $p(x, y)$ shown in Fig. 3.2(f) exhibits a stretch of both the orbital path and the axis vicinity, each elongating in an orthogonal direction. This symmetry-breaking effect is consistent with astigmatism [47, 48] and can be seen in other traps with different topological charges ℓ. For other cases of ℓ and a sets, the evaluation of the optical force components on the ρz plane allows one to compute the orbital equilibrium position ρ_{theo}. The radial equilibrium position values ρ_{theo} for each of the experimental bistable cases are presented in Table 3.1, which shows a good agreement with the experimental values (ρ_{exp}) despite the presence of astigmatism.

Although our model is able to take astigmatism into account (see appendix B, sec. B.4), we decided to simplify the discussions as we still find good agreement with the experimental data for $\ell = 8$ (as well as other bistable cases). Indeed, imperfections arising from astigmatism should still be of sizes way above the diffraction limit, which means that spheres with radii $a > \lambda_0$ should not probe details on its length-scale [48]. However, optical traps with vortex beams employ the radius of the annular spot $\tilde{r}_\ell > \lambda_0$ as the characteristic size parameter instead of λ_0. Thus, we attribute the agreement between ρ_{exp} and ρ_{theo} mostly to the averaging of the radial position over the orbital ellipsoidal path (along with the Brownian motion over several orbital revolutions), which effectively averages out the eccentricity of the orbit shown in Fig. 3.2(f).

The region that links the two mesostates in Fig. 3.2(f) also suggests that astigmatism plays a crucial role in the hopping process. Indeed, we observe how the ellipse's smaller semi-axis creates a bridge between the axial and orbital states. Our axially symmetric stigmatic MDSA model, together with the unbiased (isotropic) thermal fluctuations, fails to explain the presence of such a bridge, rendering any quantitative comparison between experimental and theoretical potential landscapes unfeasible. In a proper theoretical description of this asymmetric system, the potential barrier between the axial state and the orbital ellipse's smaller semi-axis region should be reduced by astigmatism, enabling easier thermally-activated hops between the mesostates, as seen in the experiments.

3.3.3 Simulation with the Langevin equation

As the final topic of this chapter, we show a simulation of the Brownian dynamics of a microsphere trapped in a bi-stable trap. Through the simulation of the particle dynamics, we can access a broader range of observables, such as the sojourn time in each of the mesostates or the hopping probability, compared to the exclusive analysis of the optical force field. Once again, we use the astigmatism-free MDSA theory since the azimuthal symmetry significantly facilitates the numerical performance of this method.

The 3-dimensional Langevin equation describing our system can be written as:

$$d\vec{r} = \frac{\vec{F}(\vec{r})}{\beta}\, dt + \sqrt{\frac{6k_BT}{\beta}}\, \vec{\xi}_t\, dt$$

where $\vec{\xi_t}$ is vector with modulus ξ_t (where ξ_t obeys all the properties of eq. 2.39) and a random and isotropic orientation in 3 spatial dimensions. A solution can be obtained by the following iteration:

$$\vec{r}_{i+1} = \vec{r}_i + d\vec{r},$$

provided that the initial state $\vec{r}_0$ is given.

The simulation uses pre-computed values of the optical force components and requires the total simulation time, time step (δt), temperature (T), and the laser power reaching the sample as input parameters. Additionally, the temperature value affects the magnitude of thermal force, fluid viscosity (η), and the particle's drag coefficient ($\beta\,(\eta)$). To ensure convergence of the numerical solution, we must satisfy a condition analogous to the characteristic time relationship, but for 3 dimensions. For this, we calculate the maximum value of the optical force field's divergence using the pre-computed maps and choose a time step such that the relation $\delta t \gg \tau = \beta/\max(\nabla\vec{F})$ is obeyed.

By dealing with the full optical force field, we avoid the discussions regarding energy potentials and the Helmholtz decomposition of the optical force into conservative and dissipative components. Therefore, this simulation method allows the study of the collective

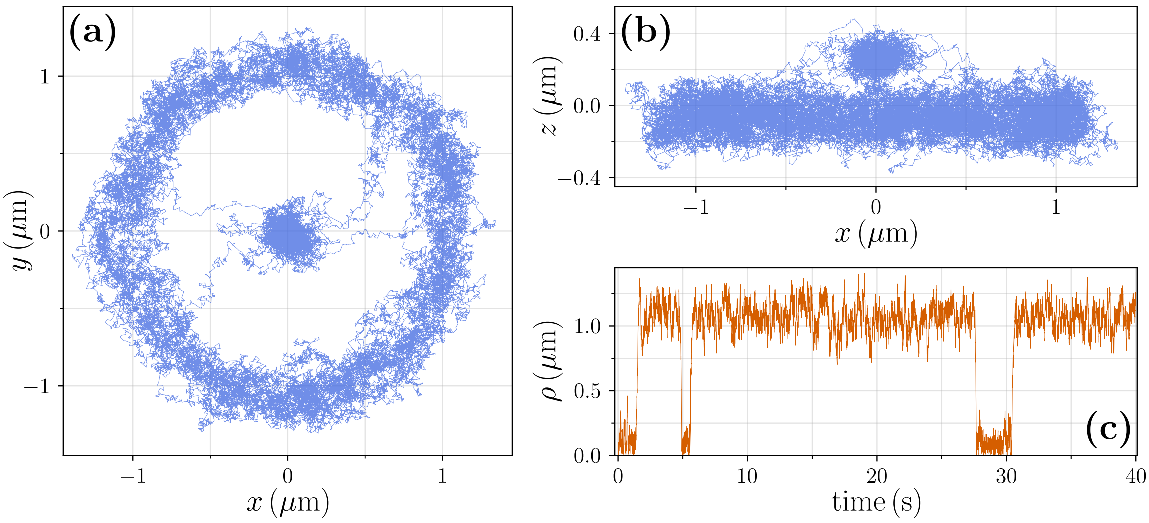

Figure 3.6: Path of a Brownian sphere embedded in a bistable trap. We employed the same parameters used in the previous section, except for $L = 1.46\mu$m. Additionally, the power reaching the sample is $P = 1.5$mW, and the time step is $\delta t = 5 \times 10^{-4}$s. Panels (a) and (b) depict the trajectory projection on the $xy-$ and $xz-$planes, respectively. Panel (c) shows the time series of the radial coordinate ρ, where we can see 5 hops, resulting in two and a half round trips within the total simulation time of 40s.

effect of conservative and dissipative force components in the bistable dynamics within our system. For example, the Kramers escape problem [4] renders a solution that largely overestimates the expected passage time if one considers the potential in Fig.3.5(b). The collective effect mentioned above could be the source of disagreement between the observed hopping rate (either in the experimental or simulation data) and the one predicted by Kramers' transition rate model, as both conservative and non-conservative force components are present in the system and might influence the transition rate expected value.

The simulation approach to describing the bistable system presented in this section enables a whole new range of possibilities to be explored. On one hand, the system described in the simulation method is much more stable and easier to characterize and control when compared to an experimental realization. On the other hand, Brownian simulations are time-consuming and computationally demanding, with increasing costs for higher-dimension systems, as opposed to experimental systems.

Chapter 4

Trapping with hybrid cylindrical vector and vortex beams: theory and applications to optical chirality

In the last two chapters, we discussed optical tweezers using vortex beams, which is an important example of a structured light field. The term structured light is used to describe any optical light field possessing polarization or phase structures along its transverse plane. We begin this chapter by presenting yet another case of structured beams: the cylindrical vector beams (cVBs). The cVBs are paraxial modes similar to vortex beams but carry a polarization helical structure instead of the phase structure present in the vortex beam modes. More specifically, cVBs exhibit a linear polarization state with their orientation varying along the transverse plane azimuth coordinate.

It can be shown that cVB modes can be decomposed into vortex beams with opposite circular polarization states and topological charges with opposite signs as well. This decomposition implies the existence of a continuum of new states in between the pure circularly polarized vortex and cVB states, comprising elliptically polarized modes carrying various different azimuthal structures of helical phases and polarization ellipse orientations (see Fig. 4.1 for an illustration of a few possible paraxial modes for a particular value of ℓ). A proper description of this new family of states is provided by the higher-order Poincaré sphere formalism [49], receiving its name due to its similarity to the canonical

Poincaré sphere representation of the polarization states. Indeed, a general paraxial beam mode described by this formalism is called a higher-order Poincaré beam [50, 51].

However, we are only interested in a subset of this larger family of beams, where the modes can be decomposed as two circularly polarized vortex beams with opposite topological charge signs, but the same absolute value. To avoid confusion, this subset of paraxial modes will be referred to as *hybrid cylindrical vector vortex beams* (hcVVBs). Creating such modes and switching between the continuum of states in this family can be realistically achieved in an experimental scenario in a few different ways [51, 52]. For instance, an SLM can be used to produce two VBs at once, each with a different topological charge, tilt, and relative phase. The two beams can be separately manipulated to create the states with opposite topological charge and polarization handedness, which can then be recombined using a beam splitter. Alternatively, hcVVBs can be produced using the so-called *q-plates* [53], which are single optical elements that act on circular polarization states by inverting the state handedness $\sigma \to -\sigma$ and adding a topological charge with a fixed modulus q and same sign of the incident handedness $\ell = -\sigma\, q$.

The bottom line of this chapter is to explore the interaction of chiral light and chiral matter using hybrid cylindrical vector vortex beams in optical tweezers. The idea, however, is not entirely new. In the last few years, tightly focused cVBs and VBs have been widely used to explore chirality phenomena. For example, Peter Banzer and his group induced a chiral dipole on two achiral spherical nano-particles [54], one of which was made of crystalline silicon and the other consisting of a gold-coated polystyrene sphere. They used a tightly focused "spiral" cVB mode, which is itself also achiral, but due to the field configuration at the focal region and the complex polarizability of the particles, the scattered field indeed carried a non-zero chirality density. The explanation is as follows: the aforementioned focused field exhibited both electric and magnetic field components oscillating in phase (or out of phase, depending on the orientation of the spiral) along the propagation direction z, while the scattering by the particles introduced a phase of approximately $\pi/2$ in either of the components, creating what is called an oscillating σ-dipole. Although this is not a case of chiral light-chiral matter interaction, this illustrates the possibilities enabled by cVBs and the tight focusing process.

A recent project by the LPO group used the MDSA theory to simulate the behavior of chiral spheres in an orbital trapping state using a tightly focused circular polarized vortex beam. In this project, it was shown that the orbital period of the trapped sphere strongly depends on the particle chirality parameter [55]. Additionally, the topological charge is an extra experimental parameter yielding a different orbital period measurement for each value of ℓ and enabling a robust fitting procedure of experimental data. Following this reasoning, using hybrid cylindrical vector vortex modes further increases the accessible experimental parameter space by controlling the relative strength and phase between each vortex beam component, which can be very beneficial in the study of optical chirality.

Therefore, we proceed with the introduction of electromagnetic chirality in the following section. The optical chirality phenomena are presented through the corresponding constitutive relations from which one can derive the expressions for the optical force on the dipolar regime as well as the Mie scattering coefficients for a chiral sphere.

4.1 Introduction to optical chirality

Optical chirality is the branch of optics that studies the interaction between the chirality of light and the chirality of matter. The chirality of light manifests itself via two quantities, which are the electromagnetic chirality density and flux. The chirality density is related to the helicity of the electromagnetic field, *i.e.* the spin angular momentum projection on the momentum direction. In the paraxial regime the momentum state is well-defined ($\mathbf{k} \simeq k\,\hat{z}$), meaning that both helicity and chirality density also correspond to the spin angular momentum component of the electromagnetic field.

The chirality of matter can be expressed in terms of two phenomena, namely circular birefringence and circular dichroism. A chiral medium is able to discriminate the light polarization handedness and exhibit a distinct index of refraction for each state. Circular birefringence is the property that presents a difference between the real parts of each handedness refraction index. This means that a linearly polarized optical field will have its polarization orientation rotated. Hence, this property is also referred to as optical rotatory power. Circular dichroism is the property related to how each field's handedness is absorbed by the chiral medium. This manifests itself as a difference between the imaginary part of the index of refraction of each polarization handedness.

Materials exhibiting chiral optical activity are a particular case of bi-anisotropic media [56, 57]. More specifically, a chiral medium (also called Pasteur medium) has the following set of constitutive relations [55, 58]:

$$\begin{pmatrix} \mathbf{D} \\ \mathbf{B} \end{pmatrix} = \begin{pmatrix} \epsilon & +i\,\kappa\,\sqrt{\epsilon_0\mu_0} \\ -i\,\kappa\,\sqrt{\epsilon_0\mu_0} & \mu \end{pmatrix} \begin{pmatrix} \mathbf{E} \\ \mathbf{H} \end{pmatrix}\,, \tag{4.1}$$

where κ is the (reciprocal) chirality parameter. The chirality property of the matter is most commonly understood as a geometric characteristic of objects that cannot be superimposed on a mirror image of themselves. In other words, geometrically chiral objects break the parity (space inversion) symmetry.

Additionally, the electromagnetic duality symmetry [59] plays an important role on the helicity and chirality conservation on scattering processes [60, 61]. Electromagnetic duality symmetry implies in the invariance of a physical system under the helicity operator:

$$\begin{aligned} \mathbf{E} &\rightarrow \cos\vartheta\,\mathbf{E} - \sin\vartheta\,\mathbf{H} \\ \mathbf{H} &\rightarrow \sin\vartheta\,\mathbf{E} + \cos\vartheta\,\mathbf{H} \end{aligned} \tag{4.2}$$

where ϑ is a real angle. Therefore, the requirement for a system to be dual-symmetric is that the ratio (ϵ_i/μ_i) should be constant everywhere (*i.e.* for any material within the system identified by the index i). According to the Noether's theorem, a general dual-symmetric system must conserve the helicity [62] and therefore the total (or integrated) optical chirality density, for any scattering process, independently of the scatterer geometry [60]. Further discussions on the relationship between optical activity of matter, optical chirality, and symmetry relations and operations can be found in references [63, 64, 65, 66] (and references therein).

In the next sub-sections, we discuss the optical force on objects made of chiral media, following the constitutive relations given by eq. 4.1. We begin with the case of a chiral dipole and describe how it interacts with an electromagnetic field, which is also composed of a chiral and an achiral part. Next, we present the Mie scattering coefficients for a chiral sphere, which is then used in the following section to build the MDSA model for a tightly focused hcVVB.

4.1.1 Optical force on a chiral dipole

We shall address the topic of chiral forces starting from the simple case of a chiral dipole interacting with a chiral field. In the achiral case, the electric and magnetic polarizabilities α and β, respectively, of a spherical dipolar particle are described by the Clausius-Mossotti relation [67, 68]. In the chiral dipolar particle case, there will be an additional polarizability χ due to the mutual electric and magnetic induction, called chiral polarizability. As stated before, a chiral medium will exhibit two distinct indices of refraction, one for each circular polarization handedness. The difference between indices of refraction is quantified by the chirality parameter κ of the material as in $n = \bar{n} + \sigma\kappa$, where $\bar{n}$ is the mean index and $\sigma = \pm 1$ is the field circular polarization handedness.

The set of polarizabilities of a chiral dipole is given by [69]:

$$
\begin{aligned}
\alpha &= 4\pi a^3 \frac{(\epsilon_r - 1)(\mu_r + 2) - \kappa^2}{(\epsilon_r + 2)(\mu_r + 2) - \kappa^2}\,, \\
\beta &= 4\pi a^3 \frac{(\mu_r - 1)(\epsilon_r + 2) - \kappa^2}{(\epsilon_r + 2)(\mu_r + 2) - \kappa^2}\,, \\
\chi &= 12\pi a^3 \frac{\kappa}{(\epsilon_r + 2)(\mu_r + 2) - \kappa^2}\,,
\end{aligned}
\tag{4.3}
$$

where a is the dipole radius, $\epsilon_r = \epsilon/\epsilon_m$ and $\mu_r = \mu/\mu_m$ are the relative permittivity and permeability, respectively, defined in terms of the host medium (ϵ_m and μ_m) and particle (ϵ and μ) electric permittivities and magnetic permeabilities. Therefore, the induced electric ($\mathbf{p}$) and magnetic ($\mathbf{m}$) dipole moments are obtained from the incident fields:

$$\begin{pmatrix} \mathbf{p} \\ \mathbf{m} \end{pmatrix} = \begin{pmatrix} \alpha\,\epsilon_m & i\,\chi\,\sqrt{\epsilon_m\mu_m} \\ -i\,\chi\,\sqrt{\epsilon_m\mu_m} & \beta\,\mu_m \end{pmatrix} \begin{pmatrix} \mathbf{E} \\ \mathbf{H} \end{pmatrix}, \tag{4.4}$$

from which the time-averaged force exerted on the dipole by the field can be calculated. The force is divided into chiral and achiral contributions, as well as dissipative and reactive components [69, 70, 71]. For now, we can consider a non-magnetic particle (thus, the whole system is not dual-symmetric), and drop the magnetic contributions to the force (proportional to the real and imaginary parts of β) in order to make the discussions easier. Henceforth, the achiral reactive and dissipative forces are related to the real and imaginary parts of α, respectively, whilst the reactive contribution depends on the gradient of the (time averaged) electric field energy density $W_E = (\epsilon_m/4)|\mathbf{E}|^2$:

$$\mathbf{F}_\alpha^{\mathrm{reac}}(\mathbf{r}) \;=\; \mathrm{Re}[\alpha]\,\nabla W_E\,, \tag{4.5}$$

and the dissipative component relates to the orbital component of the Poynting vector $\mathbf{\Pi}_{\mathbf{O}}^{(\mathbf{E})}$:

$$\mathbf{F}_\alpha^{\mathrm{diss}}(\mathbf{r}) \;=\; \frac{k^2}{\omega}\,\mathrm{Im}[\alpha]\,\mathbf{\Pi}_{\mathbf{O}}^{(\mathbf{E})}\,, \tag{4.6}$$

where $\mathbf{\Pi}_{\mathbf{O}}^{(\mathbf{E})}$ is defined as follows:

$$\mathbf{\Pi}_{\mathbf{O}}^{(\mathbf{E})}(\mathbf{r}) \;=\; \frac{-\mathrm{Im}\left[(\mathbf{E}\cdot\nabla)\mathbf{E}^* \;+\; \mathbf{E}\times(\nabla\times\mathbf{E}^*)\right]}{2\omega\mu_m}\,. \tag{4.7}$$

The chiral dipole forces are written in terms of 2 new quantities with certain similarities to the electromagnetic energy density and the Poynting vector. Those are the chirality density $K(\mathbf{r})$ and flux $\mathbf{\Phi}(\mathbf{r})$, which follows a conservation rule similar to a continuity equation [71, 72, 73]:

$$\frac{\partial K}{\partial t} \;+\; \nabla\cdot\mathbf{\Phi} \;=\; 0\,.$$

The chirality density and flux can be easily calculated for any field decomposed into the circular polarization basis. Also, for time-harmonic fields, these quantities are independent of time. The first is defined as follows:

$$K(\mathbf{r}) \;=\; \left(\frac{k^2}{2\omega}\right) \mathrm{Im}\big[\mathbf{E}\cdot\mathbf{H}^*\big] \tag{4.8}$$

while the latter is:

$$\mathbf{\Phi}(\mathbf{r}) \;=\; \left(\frac{-\omega}{4}\right) \mathrm{Im}\big[\,\epsilon_1\left(\mathbf{E}\times\mathbf{E}^*\right) \,+\, \mu_0\left(\mathbf{H}\times\mathbf{H}^*\right)\big]\,. \tag{4.9}$$

From the chirality density, we can obtain the chiral reactive component of the force on a dipole:

$$\mathbf{F}_{\chi}^{\mathrm{reac}}(\mathbf{r}) \;=\; \frac{1}{k}\mathrm{Re}[\chi]\,\nabla K\,. \tag{4.10}$$

The dissipative chiral component, however, depends on both the total Poynting vector $\mathbf{\Pi}$ and the chirality flux:

$$\mathbf{F}_{\chi}^{\mathrm{diss}}(\mathbf{r}) \;=\; \frac{2\,k}{\omega}\,\mathrm{Im}[\chi]\left(\mathbf{\Phi} \,-\, \frac{\nabla\times\mathbf{\Pi}}{2}\right). \tag{4.11}$$

The total Poynting vector $\mathbf{\Pi}$ in the expression above can be written as a combination of orbital and spin contributions:

$$\mathbf{\Pi}\,(\mathbf{r}) \;=\; \mathbf{\Pi}_{\mathbf{O}}^{(\mathbf{E})} \,+\, \mathbf{\Pi}_{\mathbf{S}}^{(\mathbf{E})} \;=\; \mathbf{\Pi}_{\mathbf{O}}^{(\mathbf{E})} \,-\, \frac{1}{4\,\omega\,\mu_0}\,\mathrm{Im}\big[\,\nabla\times\left(\mathbf{E}\times\mathbf{E}^*\right)\big]\,, \tag{4.12}$$

where we used the (electric) orbital contribution defined in eq. 4.7.

The model for the optical forces on a chiral dipole we presented in this section will be particularly important when we discuss the MDSA model for a sphere composed of a chiral medium. Although we have included expressions related to the non-conservative components of the optical force (eqs. 4.6, 4.7, 4.9, 4.11, and 4.12), we shall limit our discussion to the reactive terms only. In fact, we only need the conservative component of the optical force to obtain this chapter's main result. However, it is worth mentioning that beyond the dipole limit, non-conservative force components appear even when the imaginary part of χ is zero due to the scattering of higher-order multipoles. Additionally, the dissipative force component in eq. 4.11 can play an important role on probing and characterizing chiral particles on the nano-scale [74, 75].

In the next subsection, we will present the Mie coefficients for a chiral sphere. This is the next step to obtain the more general Mie-Debye force model, which is valid beyond the dipole limit. With the chiral Mie coefficients in hand, we will be able to take the small radius limit (compared to the wavelength) and verify that we qualitatively recover the behavior of the force in the dipole limit. This agreement allows us to infer the resulting behavior of the optical force using the quantities presented in this section, such as the chirality density K and electric field energy density W_E.

4.1.2 Chiral scatterer in the Mie regime

In this section, we present the Mie coefficients for a microsphere of radius a that scatters an incident circularly polarized beam with handedness defined by σ. The Mie coefficients for a chiral sphere are obtained in a similar (yet not identical) way to the conventional case. In sec. 2.2.1, we saw that the boundary conditions that the field must obey at the sphere's surface require the decomposition of the incident field into TE and TM modes, which are locally linearly polarized. In the achiral case, the microsphere's medium does not discriminate the polarization state of the propagating wave, requiring only two Debye potentials for the field inside the microsphere and two more for the scattered field.

However, as we saw at the beginning of sec. 4.1.1, a circularly polarized wave propagates in a chiral medium with a refractive index that depends on its handedness. Therefore, optical fields with an arbitrary polarization state propagating in a chiral medium will exhibit distinct refractive indices for each of their circular polarization components. In the context of Mie scattering, each circular polarization state of the field within the sphere will propagate with a different wave vector $k_\sigma = n_\sigma k_0$.

In the formulation presented below, the chiral Mie coefficients will be defined to extend the definition of conventional coefficients, presented in eq. 2.30 for the scattered field. The new coefficients are indexed by the sign of the circular polarization of the incident beam σ, as follows:

$$a_j^{(\sigma)} = a_j - i\,\sigma\,c_j\,, \tag{4.13}$$

$$b_j^{(\sigma)} = b_j - i\,\sigma\,c_j\,, \tag{4.14}$$

where the coefficients a_j, b_j, and c_j are given by:

$$\begin{aligned}
a_j &= \frac{1}{\Delta_j(k_1\,a)}\left[V_j^{(+)}(k_1\,a)\,A_j^{(-)}(k_1\,a) + V_j^{(-)}(k_1\,a)\,A_j^{(+)}(k_1\,a)\right],\\
b_j &= \frac{1}{\Delta_j(k_1\,a)}\left[W_j^{(+)}(k_1\,a)\,B_j^{(-)}(k_1\,a) + W_j^{(-)}(k_1\,a)\,B_j^{(+)}(k_1\,a)\right],\\
c_j &= \frac{i}{\Delta_j(k_1\,a)}\left[W_j^{(+)}(k_1\,a)\,A_j^{(-)}(k_1\,a) - W_j^{(-)}(k_1\,a)\,A_j^{(+)}(k_1\,a)\right].
\end{aligned} \tag{4.15}$$

The term in the denominator Δ_j as well as the auxiliary functions $W_j^{(\pm)}$, $V_j^{(\pm)}$, $A_j^{(\pm)}$, and $B_j^{(\pm)}$ are defined as:

$$\begin{aligned}
\Delta_j(x) &= W_j^{(-)}(x)V_j^{(+)}(x) + W_j^{(+)}(x)V_j^{(-)}(x)\,,\\
W_j^{(\pm)}(x) &= \overline{N}\psi_j\left(N_\pm x\right)\zeta_j^{(1)\prime}(x) - \zeta_j^{(1)}(x)\,\psi_j'\left(N_\pm x\right)\,,\\
V_j^{(\pm)}(x) &= \psi_j\left(N_\pm x\right)\zeta_j^{(1)\prime}(x) - \overline{N}\zeta_j^{(1)}(x)\,\psi_j'\left(N_\pm x\right)\,,\\
A_j^{(\pm)}(x) &= \overline{N}\psi_j\left(N_\pm x\right)\psi_j'(x) - \psi_j(x)\,\psi_j'\left(N_\pm x\right)\,,\\
B_j^{(\pm)}(x) &= \psi_j\left(N_\pm x\right)\psi_j'(x) - \overline{N}\psi_j(x)\,\psi_j'\left(N_\pm x\right)\,,
\end{aligned} \tag{4.16}$$

where $N_\pm = (n_\pm/n_1)$ are the relative indices of refraction for each circular polarization handedness inside the chiral sphere and $\overline{N}$ is the mean relative index of refraction, defined as the harmonic mean of N_+ and N_-:

$$\overline{N} = \frac{2\,N_+N_-}{N_+ + N_-}\,.$$

Also, the functions $\psi_j(x)$ and $\zeta_j^{(1)}(x)$ are the Ricatti-Bessel functions defined in sec. 2.2.1 after the achiral Mie coefficients in eq. 2.31. Note that we omitted σ in the notation for the indices of refraction of a chiral medium, using $\pm$ instead. This is to avoid confusion, as σ denotes the incident field component handedness, and $\pm$ refers to the handedness of the fields inside the sphere[1]. Therefore, the wavevectors inside the sphere are $N_{\pm}k_1 = (n_{\pm}/n_1)k_1 = k_{\pm}$, where the $+$ and $-$ signs represent left and right-handedness, respectively. In the case where $\kappa = 0$, we obtain $k_{\pm} = k_2$, $c_j = 0$, and both a_j and b_j recover the expressions of eq. 2.31.

As the Debye potentials in eqs. 2.30 already depend on the sign of σ of the incident field, we can directly insert the new coefficients in eqs. 4.13 and 4.14 into eq. 2.30 in order to obtain the Debye potentials for the scattered fields. Finally, those are used to calculate the optical force exerted by tightly focused hcVVBs on a chiral sphere, which is the topic of the next section.

4.2 Chiral MDSA theory with hcVVBs

In this section, we present the expressions for the electromagnetic field and the optical force exerted by a strongly focused hcVVB. We describe the resulting incident field in terms of Richards-Wolf integrals and Debye potentials, therefore extending the results of Chapter 2 to describe a broader range of polarization states.

Due to the linearity of the Helmholtz equation, the results for the Richards-Wolf fields with input circular polarized vortex beam can be easily extended for the case of hcVVBs, only requiring a proper paraxial mode decomposition. The hcVVB beams are superpositions of vortex beams with opposite polarization and topological charge, and therefore the expressions for the fields and Debye potentials are given as sums of the respective pure circular polarization projection components.

We shall introduce the topic of hcVVB beams with the simple case where the circular polarization components are equal, and the topological charge associated with the left

[1] Recall that the scattering process does not conserve the helicity, and a pure circularly polarized incident field will produce fields with the opposite polarization both outside (scattered) and inside the sphere, whether chiral or not.

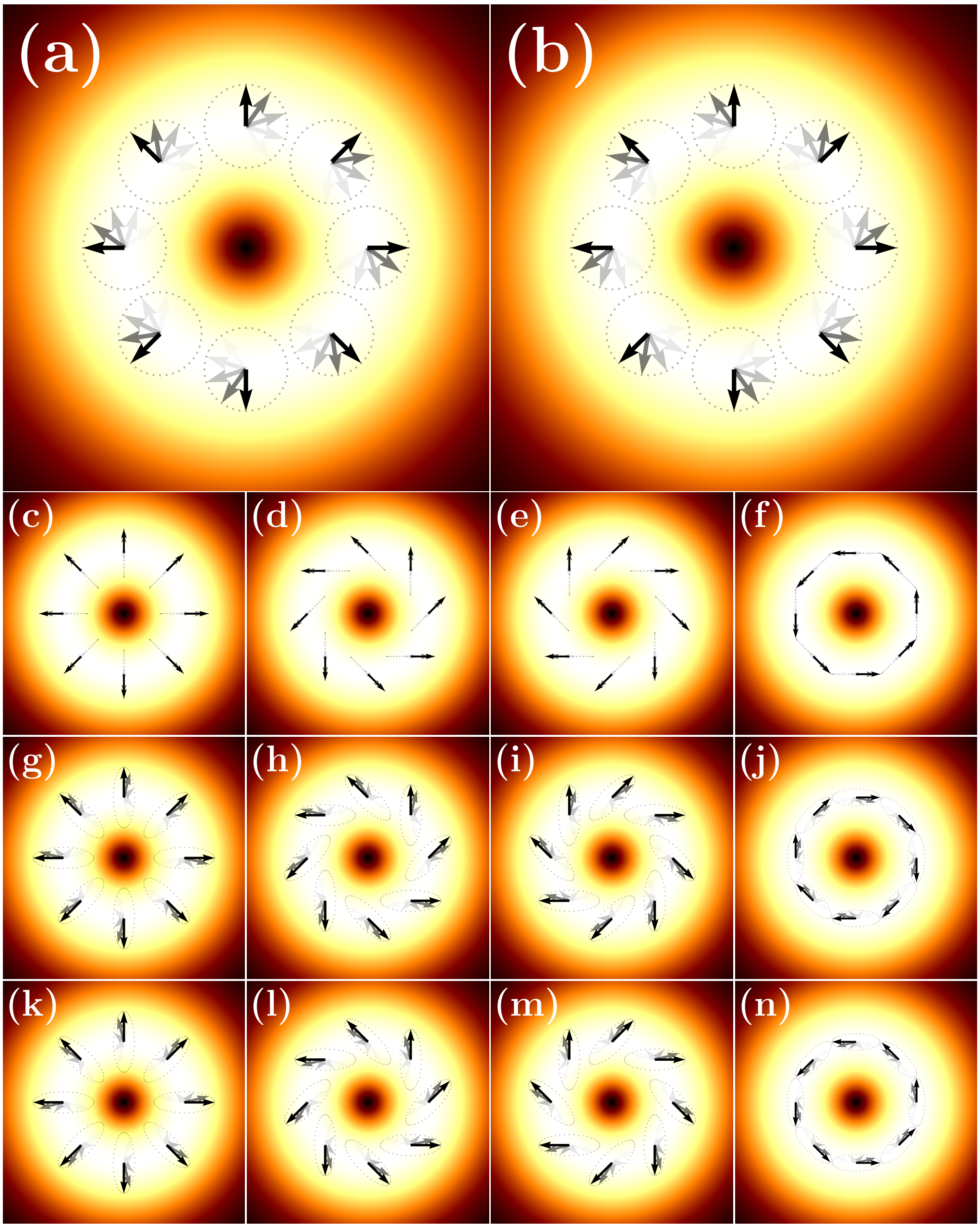

Figure 4.1: Illustration of different paraxial polarization states, comprised of the transverse intensity profile (background) and the real part of the polarization vector evolving in time. The time evolution can be understood by inspection of panels (a) and (b), corresponding to left and right-circular polarized vortex beams $|\ell = -1, \sigma = 1\rangle$ and $|\ell = 1, \sigma = -1\rangle$, respectively. Therefore, the polarization vector in panels (a) and (b) rotates in the counter-clockwise and clockwise senses, respectively. The smaller panels (c)-(k) are linear combinations of the states in panels (a) and (b).

circularly polarized ($\sigma = 1$) vortex beam is $\ell = -1$. This yields a family of paraxial modes called cylindrical vector beams (cVBs). We can represent their state in the 'ket' notation as: $|\psi\rangle = (1/\sqrt{2})(\, e^{i\zeta}\; |\ell = -1,\, \sigma = 1\rangle + |\ell = 1,\, \sigma = -1\rangle\,)$. The cVB modes are locally linearly polarized, exhibiting a polarization orientation that varies across the transverse plane with a relative orientation (being radially or azimuthally polarized, for example) parametrized by the phase ζ.

Now, we can consider the case where the circular polarization components are not equal, leading to a beam with local elliptical polarization with a polarization axis that varies across the transverse plane. Now, the state in the 'ket' notation reads: $|\psi\rangle = (\, \psi_+ \, e^{i\zeta}\; |\ell = -1,\, \sigma = 1\rangle + \psi_- \; |\ell = 1,\, \sigma = -1\rangle\,)$, where $\psi_\pm$ are the circular polarization projection components.

It is worth noting that the states depicted in Fig. 4.1 can also be characterized by the entanglement between each of their polarization components. This description can be useful in the discussions regarding the tightly focused fields resulting from those states. The degree of classical entanglement can be quantified by the concurrence[76, 77]:

$$C = 2\,(\psi_+ \psi_-)\,. \tag{4.17}$$

The concurrence is maximum ($C = 1$) when $\psi_+ = \psi_-$, corresponding to the cVB family of modes, which are the maximally entangled or non-separable states. On the other hand, the concurrence is minimum ($C = 0$) when $\psi_\pm = 1$, leading to the two circular polarized vortex beam modes, which are separable states.

In Fig. 4.1, we plot a few examples of the possible paraxial hcVVB modes arising from different combinations of $\psi_\pm$ and ζ. If we set $\psi_+ = \psi_-$, we obtain the states in panels (c-f) (second row) of Fig. 4.1. When $\psi_+ > \psi_-$, we obtain the states in panels (g-j) (third row); while the states in panels (k-n) (fourth row) correspond to the relation $\psi_+ < \psi_-$. Regarding the relative phase ζ between the basis components (states in panels (a) and (b)), we depict 4 different examples of possible values: $\zeta = 0$ yields panels (c), (g), and

(k) (first column); $\zeta = \frac{1}{2}\pi$ yields panels (d), (h), and (l) (second column); $\zeta = \pi$ yields panels (f), (j), and (n) (fourth column); and $\zeta = \frac{3}{2}\pi$ yields panels (e), (i), and (n) (third column).

Finally, we begin the next sub-section by presenting the paraxial parametrization of the paraxial hcVVBs and the Richard-Wolf theory expressions for the tightly focused electromagnetic fields. Then, we present the resulting field intensity and chirality density distributions in the focal region. Next, we present the MDSA expressions for the tightly focused hcVVBs and a scattering chiral sphere, which present a few differences when compared to other MDSA force models with mixed-polarization states (for example, the case of linearly polarized Gaussian beams, present in ref. [44]), as the chiral scattering coefficients depends on the polarization state σ.

4.2.1 Intensity and Chirality of tightly focused hcVBBs

We begin the construction of the expressions for a tightly focused hybrid cylindrical vector vortex beam with the definition and parametrization of the paraxial state. As we showed in the introduction, the paraxial mode consists of a superposition of vortex beams with opposite polarization handednesses and topological charges. Following the 'ket' notation, the corresponding electric field of the paraxial beam reads:

$$\mathbf{E}_{\mathrm{p}}(\rho, \phi, z) = E_0 \left(\frac{\sqrt{2}\rho}{w_0} \right)^{|\ell|} e^{ik_0 z} e^{-\frac{\rho^2}{w_0^2}} \times \left(\tilde{\psi}_+ \, e^{-i\ell\phi} \hat{\boldsymbol{\epsilon}}_+ \, + \, \psi_- \, e^{i\ell\phi} \hat{\boldsymbol{\epsilon}}_- \right), \tag{4.18}$$

where $\tilde{\psi}_+$ and ψ_- are the left- and right-handed circular polarization state components, respectively, and the subscript $\pm$ is a short-hand notation for the sign of $\sigma = \pm 1$. We defined $\tilde{\psi}_+$ as a complex number, denoted by the $\sim$ symbol above it, while ψ_- is set as a non-negative real number. Therefore, any relative phase ζ between the two components is contained in the $\sigma = +1$ component, allowing us to write the latter as $\tilde{\psi}_+ \; = \; e^{i\zeta} \, \psi_+$ where ψ_+ is a non-negative real amplitude. Since the components are normalized by the condition

$$|\tilde{\psi}_+|^2 + \psi_-^2 = 1, \tag{4.19}$$

we can describe the state in eq. 4.18 using only ψ_+, ζ and the topological charge ℓ of the $\sigma = -1$ component.

The tightly focused electric field can be obtained by linearity, using the paraxial field expression from eq. 4.18 as the input field for the Richards-Wolf model. The resulting expression in Cartesian coordinates in terms of the function $I_m^{(\ell)}$ defined in eq. 2.12 reads:

$$\mathbf{E}^{(\ell)}(\mathbf{r}) = \begin{pmatrix} \tilde{\psi}_+ E_x^{(+1,-\ell)} + \psi_- E_x^{(-1,\ell)} \\ \tilde{\psi}_+ E_y^{(+1,-\ell)} + \psi_- E_y^{(-1,\ell)} \\ \tilde{\psi}_+ E_z^{(+1,-\ell)} + \psi_- E_z^{(-1,\ell)} \end{pmatrix} = \left(\frac{k\,\gamma\,w_0\,E_0}{2}\right) \times \tag{4.20}$$

$$\begin{pmatrix} \tilde{\psi}_+ (-i)^{-\ell+1}\big(e^{-i\ell\phi}\, I_0^{(-\ell)} + e^{-i(\ell-2)\phi}\, I_2^{(-\ell)}\big) + \psi_- (-i)^{\ell+1}\big(e^{i\ell\phi}\, I_0^{(\ell)} + e^{i(\ell-2)\phi}\, I_{-2}^{(\ell)}\big) \\ \tilde{\psi}_+ (-i)^{-\ell}\big(e^{-i\ell\phi}\, I_0^{(-\ell)} - e^{-i(\ell-2)\phi}\, I_2^{(-\ell)}\big) - \psi_- (-i)^{\ell}\big(e^{i\ell\phi}\, I_0^{(\ell)} - e^{i(\ell-2)\phi}\, I_{-2}^{(\ell)}\big) \\ -2\,\tilde{\psi}_+ (-i)^{-\ell}\big(e^{-i(\ell-1)\phi}\, I_1^{(-\ell)}\big) + 2\,\psi_- (-i)^{\ell}\big(e^{i(\ell-1)\phi}\, I_{-1}^{(\ell)}\big) \end{pmatrix}.$$

As each circular polarization component obeys the relation given by eq. 2.2 independently, the magnetic field is given by:

$$\mathbf{H}^{(\ell)}(\mathbf{r}) = \left(-\,i\sqrt{\frac{\epsilon}{\mu_0}}\right)\left(\frac{k\,\gamma\,w_0\,E_0}{2}\right) \times \tag{4.21}$$

$$\begin{pmatrix} \tilde{\psi}_+ (-i)^{-\ell+1}\big(e^{-i\ell\phi}\, I_0^{(-\ell)} + e^{-i(\ell-2)\phi}\, I_2^{(-\ell)}\big) - \psi_- (-i)^{\ell+1}\big(e^{i\ell\phi}\, I_0^{(\ell)} + e^{i(\ell-2)\phi}\, I_{-2}^{(\ell)}\big) \\ \tilde{\psi}_+ (-i)^{-\ell}\big(e^{-i\ell\phi}\, I_0^{(-\ell)} - e^{-i(\ell-2)\phi}\, I_2^{(-\ell)}\big) + \psi_- (-i)^{\ell}\big(e^{i\ell\phi}\, I_0^{(\ell)} - e^{i(\ell-2)\phi}\, I_{-2}^{(\ell)}\big) \\ -2\,\tilde{\psi}_+ (-i)^{-\ell}\big(e^{-i(\ell-1)\phi}\, I_1^{(-\ell)}\big) - 2\,\psi_- (-i)^{\ell}\big(e^{i(\ell-1)\phi}\, I_{-1}^{(\ell)}\big) \end{pmatrix}.$$

Before proceeding to the calculation of the electric energy density W_E, it is convenient to define an important symmetry relation [7]: $I_{-m}^{(-\ell)} = (-1)^{\ell+m}\, I_m^{(\ell)}$. This property allows us to write W_E in terms of $I_0^{(-\ell)}$, $I_1^{(-\ell)}$ and $I_2^{(-\ell)}$ only:

$$W_E(\mathbf{r}) = \left(\frac{k\,\gamma\,w_0\,E_0}{2}\right)^2 \left(\frac{\epsilon_1}{2}\right)\Bigg(|I_0^{(-\ell)}|^2 + 2|I_1^{(-\ell)}|^2 + |I_2^{(-\ell)}|^2 + \\ +4\,\mathrm{Re}\Big[\big(\Psi^{(+)}\big)\,(-1)^{\ell}\Big(|I_1^{(-\ell)}|^2 + \mathrm{Re}\big\{I_2^{(-\ell)} I_0^{(-\ell)\,*}\big\}\Big)\Big]\Bigg), \tag{4.22}$$

where $\Psi^{(+)}$ is the left-handed polarization (+) cross-term coefficient (more generally $\Psi^{(\sigma)}$), defined as:

$$\Psi^{(\sigma)}(\zeta\,,\,\phi) = (\psi_+\psi_-)\,(-1)^\ell\,e^{i\sigma\zeta}\,e^{-i2\sigma(\ell-1)\phi}\,, \tag{4.23}$$

which carries the dependence on the azimuthal coordinate ϕ. Note that the presence of the factor $(-1)^\ell$ in eq. 4.23 is not without reason, as this definition greatly simplifies the expressions for the optical force. Also, we assume the dependence on ℓ is contextually implied (assuming the value relative to the $\sigma = -1$ state) and therefore $(\Psi^{(\pm)})^* = \Psi^{(\mp)}$ is true for any ℓ.

It becomes clear from eq. 4.23 that the case $\ell = 1$ is the only configuration to exhibit azimuthal symmetry, as no other value of ℓ leads to a null value for the last term exponent for any value of ϕ. This expression also implies that any tightly focused pure circular polarized beam, given by eq. 2.15, will exhibit the same focal energy density distribution as a beam with opposite polarization and topological charge signs, *i.e.* $W_E^{(\sigma,\,\ell)} = W_E^{(-\sigma,\,-\ell)}$. We can substitute the expression for the field intensity distribution of a pure circular polarized $W_E^{(+,\,-\ell)}$ into eq. 4.22 and identify the remaining terms as the cross-polarization contribution $W_E^{(\text{cross},\,-\ell)}$, obtaining:

$$\begin{aligned} W_E(\mathbf{r}) \;&=\; W_E^{(+,\,-\ell)} \;+\; 4\left(\frac{k\,\gamma\,w_0\,E_0}{2}\right)^2\left(\frac{\epsilon_1}{2}\right)\times \\ &\times\;\mathrm{Re}\Big[\big(\Psi^{(+)}\big)\,(-1)^\ell\Big(|I_1^{(-\ell)}|^2 + \mathrm{Re}\big\{I_2^{(-\ell)}I_0^{(-\ell)\,*}\big\}\Big)\Big] \;= \\ &=\; W_E^{(+,\,-\ell)} \;+\; 2\,(-1)^\ell\,\mathrm{Re}\big(\Psi^{(+)}\big)\times W_E^{(\text{cross},\,-\ell)}\,. \end{aligned} \tag{4.24}$$

In a similar way, we can obtain an expression for the chirality density K that is just as simple as the one for W_E. By decomposing any electromagnetic wave in the circular polarization basis, we can write the field as $\mathbf{E} = (\,\tilde{\psi}_+\mathbf{E}_+ \,+\, \psi_-\mathbf{E}_-)$. Using this decomposition and eq. 4.8, we obtain the chirality density K for an arbitrary field, which is given by:

$$K(\mathbf{r}) = \left(\frac{k^2}{2\omega}\right)\left(\sqrt{\frac{\epsilon_1}{\mu_0}}\right)\mathrm{Im}\big[\big(\,\tilde{\psi}_+\mathbf{E}_+ \,+\, \psi_-\mathbf{E}_-\,\big)\cdot(i)\big(\,\tilde{\psi}_+^*\mathbf{E}_+^* \,-\, \psi_-\mathbf{E}_-^*\,\big)\big] \;=$$

$$= \left(\frac{k^2}{2\omega}\right)\left(\sqrt{\frac{\epsilon_1}{\mu_0}}\right)\left[\,\psi_+^2\,|\mathbf{E}_+|^2 \,-\, \psi_-^2\,|\mathbf{E}_-|^2\,\right]. \tag{4.25}$$

From eqs. 4.25 and 2.15, and using the fact that $W_E^{(\sigma,\,\ell)} = W_E^{(-\sigma,\,-\ell)}$, we can compute the chirality density for a tightly focused hcVVB:

$$K(\mathbf{r}) \;=\; 2\,k\left(\,\psi_+^2 - \psi_-^2\,\right)W_E^{(+,\,-\ell)}\,. \tag{4.26}$$

As we can see, K is always proportional to $W_E^{(\sigma,\,\ell)}$, and its amplitude is determined by the difference of the squared polarization components $(\psi_+^2 - \psi_-^2)$.

4.2.2 MDSA expressions for a chiral sphere

We now present the expressions for the radial force component of the efficiency factor Q_ρ. Similarly to the discussion presented in sec. 2.2.2, we can identify two contributions to the optical force, which are the extinction and scattering components. The extinction force components originate from the product between the incident and the scattered fields, while the scattering components are related to the product between scattered fields. In the present section, we can identify two additional labels on the force terms, now related to the polarization state of the incident field.

While the incident field is separated into two orthogonal circular polarization contributions, the Mie scattering process does not conserve polarization[2], as is illustrated in Fig. 4.2. This implies that cross-polarization terms arise in the force calculations. Instead of having two terms (extinction and scattering) for a purely circular polarized trapping beam, there will be six extra terms: two 'direct' (for the opposite circular polarizations) and four 'cross' polarization terms. Therefore, two extinction and two scattering new

[2]This is true for both the chiral and achiral sphere cases.

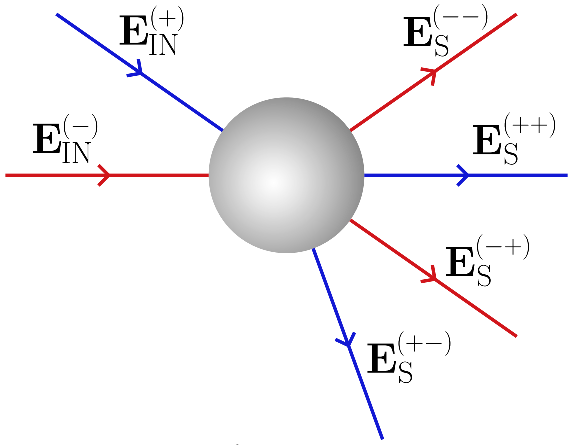

Figure 4.2: Schematic representation of Mie scattering channels. Circularly polarized incident fields ($\mathbf{E}_{\mathrm{IN}}^{(+)}$ and $\mathbf{E}_{\mathrm{IN}}^{(-)}$) will produce scattered fields with both the same ($\mathbf{E}_{\mathrm{IN}}^{(+)} \to \mathbf{E}_{\mathrm{S}}^{(++)}$ and $\mathbf{E}_{\mathrm{IN}}^{(-)} \to \mathbf{E}_{\mathrm{S}}^{(--)}$) and opposite polarization state ($\mathbf{E}_{\mathrm{IN}}^{(+)} \to \mathbf{E}_{\mathrm{S}}^{(+-)}$ and $\mathbf{E}_{\mathrm{IN}}^{(-)} \to \mathbf{E}_{\mathrm{S}}^{(-+)}$).

components have to be calculated (for each incident polarization state), where the extinction terms are proportional to $\mathbf{E}_{\mathrm{IN}}^{(\pm)} \cdot \mathbf{E}_{\mathrm{S}}^{(\mp\pm)*}$ and scattering terms are proportional to $(\mathbf{E}_{\mathrm{S}}^{(\pm\pm)}+\mathbf{E}_{\mathrm{S}}^{(\pm\mp)}) \cdot (\mathbf{E}_{\mathrm{S}}^{(\mp\mp)}+\mathbf{E}_{\mathrm{S}}^{(\mp\pm)})^*$.

The scattering component of the efficiency factor is given by:

$$\begin{aligned}
Q_{s\rho}^{(\ell)}(\rho,\phi,z) = {} & \frac{2(2\gamma^2)^{|\ell|+1}}{|\ell|!\,A_\ell N_a} \sum_{jm\sigma} \Bigg\{ \Bigg[\frac{\sqrt{j(j+2)(j+m+1)(j+m+2)}}{j+1} \times \\
& \times \mathrm{Im}\Big(\big(a_j^{(\sigma)} a_{j+1}^{(\sigma)*} + b_j^{(\sigma)} b_{j+1}^{(\sigma)*}\big) \big[G_{j,m}^{(\sigma,\ell)} G_{j+1,m+1}^{(\sigma,\ell)*} + G_{j,-m}^{(\sigma,\ell)} G_{j+1,-(m+1)}^{(\sigma,\ell)*}\big] \big(\psi_\sigma^2\big) + \\
& + \big(a_j^{(\sigma)} a_{j+1}^{(-\sigma)*} - b_j^{(\sigma)} b_{j+1}^{(-\sigma)*}\big) \big[G_{j,m}^{(\sigma,\ell)} G_{j+1,m+1}^{(-\sigma,\ell)*} + G_{j,-m}^{(\sigma,\ell)} G_{j+1,-(m+1)}^{(-\sigma,\ell)*}\big] \big(\Psi^{(\sigma)}\big) \Big) \Bigg] - \\
& - \Bigg[\sigma \frac{(2j+1)}{j(j+1)} \sqrt{(j-m)(j+m+1)} \times \Big(2\,\mathrm{Re}\big(a_j^{(\sigma)} b_j^{(\sigma)*}\big)\, \mathrm{Im}\big[G_{j,m}^{(\sigma,\ell)} G_{j,m+1}^{(\sigma,\ell)*}\big] \big(\psi_\sigma^2\big) + \\
& + \mathrm{Im}\Big[\big(a_j^{(\sigma)} b_j^{(-\sigma)*}\big) \big(G_{j,m}^{(\sigma,\ell)} G_{j,m+1}^{(-\sigma,\ell)*} - G_{j,m+1}^{(\sigma,\ell)} G_{j,m}^{(-\sigma,\ell)*}\big) \big(\Psi^{(\sigma)}\big) \Big] \Big) \Bigg] \Bigg\},
\end{aligned} \tag{4.27}$$

and the extinction component is:

$$Q_{e\rho}^{(\ell)}(\rho,\phi,z) = \frac{(2\gamma^2)^{|\ell|+1}}{|\ell|!\,A_\ell N_a} \sum_{jm\sigma} (2j+1)\, \mathrm{Im}\Big\{ \Big(G_{j,m}^{(\sigma,\ell)}\Big) \times \tag{4.28}$$

$$\times \Big[\big(a_j^{(\sigma)} + b_j^{(\sigma)}\big) \big[G_{j,m+1}^{(-)(\sigma,\ell)} - G_{j,m-1}^{(+)(\sigma,\ell)}\big]^* \big(\psi_\sigma^2\big) + \big(a_j^{(\sigma)} - b_j^{(\sigma)}\big) \big[G_{j,m+1}^{(-)(-\sigma,\ell)} - G_{j,m-1}^{(+)(-\sigma,\ell)}\big]^* \big(\Psi^{(\sigma)}\big) \Big] \Big\}.$$

Here, we identify the 'direct-polarization' terms as the ones proportional to (ψ_σ^2) and the 'cross-polarization' terms as the ones proportional to $(\Psi^{(\sigma)})$, defined in eq. 4.23. Also, the multipole coefficients $G_{j,m}^{(\sigma,\ell)}$, $G_{j,m}^{\prime(\sigma,\ell)}$ and $G_{j,m}^{(\pm)(\sigma,\ell)}$ were redefined to simplify the notation, considering that ℓ have opposite signs for each polarization component, and that the value of the index (ℓ) used in the above equations refer to the one of the $\sigma = -1$ state (meaning that the sign of ℓ relative to each polarization state is given by $-\sigma\,\mathrm{sgn}(\ell)$). The multipole coefficient $G_{j,m}^{(\sigma,\ell)}$ is defined as:

$$\begin{aligned} G_{j,m}^{(\sigma,\ell)} = & \int_0^{\theta_0} d\theta (\sin\theta)^{1+|\ell|} \sqrt{\cos\theta}\, T(\theta) \\ & e^{-\gamma^2 \sin^2\theta}\, e^{i\Phi(\theta,z)}\, d_{m,\sigma}^{j}(\theta_1)\, J_{m+\sigma(\ell-1)}(k_1 \rho \sin\theta_1)\,, \end{aligned} \tag{4.29}$$

where the term $\Phi(\theta, z)$ differs from the one defined in eq. 2.4.

Similar calculations were already conducted in previous works [44, 78], where the input paraxial beam is linearly polarized, and thus cross-polarization terms also arise. However, when considering a theory employing chiral Mie coefficients [55, 79, 80], the expressions present in the aforementioned works are not recovered. The expressions for the azimuthal and axial optical force components, for the remaining multipole coefficient, and for the phase function $\Phi(\theta, z)$ are given in appendix B.

In the next section, we show some numerical calculations using the optical force theory presented above. Our results are also based on the discussions of sec. 4.1, where the dipole limit serves as an intuitive guide for the behavior of the optical force. However, the results we are about to present are not limited to the dipole limit length scale, as the MDSA model enables us to explore a broader range of systems and scenarios resulting from the presence of higher-order multipoles.

4.3 Scheme for optical chiral sorting

In this section, we present the numerical results obtained from the MDSA theory presented in the previous chapter. To assess the validity of the MDSA expressions presented in the last section, we first assert that the resulting force landscape is in qualitative agreement with the well-established dipole limit. Indeed, besides providing this simple and reliable test for the MDSA theory, the dipole limit for the optical forces also helps us to build intuition on how the chiral and achiral optical forces behave in this novel scenario, just like the achiral case presented in all of the previous chapters.

In order to connect the Mie scattering theory with the force expressions in the dipole limit, we must relate the chiral and achiral polarizabilities in eq. 4.3 with the refractive indices $n_{\pm}$, as the chiral Mie coefficients, presented at the end of sec. 4.1.2, are a function of the latter. Following the procedure in ref. [70], we stipulate a maximum κ value within the optical force field simulations using a fixed ratio between the chiral and achiral polarizabilities from eq. 4.3. We assume that the particle is made of polystyrene with an additional chirality parameter κ, and we use the relation between its mean refraction index and relative permittivity $n_2 = \sqrt{\epsilon_r}$ to calculate the resulting polarizability ratio $\xi = \chi/\alpha$. Finally, we can solve for κ to obtain its upper bound as a function of ξ:

$$\kappa = \frac{(-3/\xi) + \sqrt{(3/\xi)^2 + 12(\epsilon_r - 1)}}{2}. \tag{4.30}$$

Using the same value for the polarizability ratio as in ref. [70] $\xi = 0.05$, and the refraction index of polystyrene $n_2 = 1.576$ (for $\lambda = 1.064\mu$m), we obtain the following upper bound for the chirality parameter $\kappa \approx 0.021$.

It is relevant to emphasize something upfront: from the tests in the dipole regime alone, we already harnessed a unique and promising result. The force exerted by tightly focused hcVVBs exhibits an interesting property, which is the topic of the first subsection.

4.3.1 Comparison with dipole limit

The present section contains the discussion regarding how the expressions for W_E and K presented in sec. 4.2.1 and the optical force exerted by this optical field in a chiral dipole are related to each other. We shall address the family of fields with $\ell = 1$, taking advantage of their azimuthal symmetry for W_E, K, and the optical forces.

Firstly, we rewrite the expression for the pre-factor of the cross-polarization contribution to the intensity $W_E^{(\mathrm{cross},\,-1)}$ in eq. 4.24 (taking $\ell = 1$ in eq. 4.23):

$$\mathcal{C}_1(\zeta\,,\,\psi_+)\;\equiv\;(\psi_+\psi_-)(-1)^2\mathrm{Re}\big(e^{i\zeta}e^{-i2(1-1)\phi}\big)\;=\;(\psi_+\psi_-)\cos\zeta\,. \tag{4.31}$$

Here, we defined the function $\mathcal{C}_1$ to emphasize that different values of ψ_+ and ζ can lead to the same value of the cross-polarization contribution and, therefore, to the same electric field intensity distribution W_E. Additionally, the function $\mathcal{C}_1$ can be written in terms of the concurrence C defined in eq. 4.17:

$$\mathcal{C}_1\;=\;\frac{C}{2}\,\cos\zeta\;,$$

from which we can conclude that the range of possible values for $\mathcal{C}_1$ is bounded by the concurrence C. In other words, states with higher degrees of entanglement have larger concurrence C values and therefore broader ranges of possible values for $\mathcal{C}_1$.

According to eq. 4.26, the chirality distribution K will be proportional to $W_E^{(+,\,-1)}$ and the pre-factor $(\psi_+^2 - \psi_-^2)$, which is proportional to the S_3 Stokes parameter [49]. For practical notation reasons, we define a function for this pre-factor:

$$\mathcal{D}(\psi_+) = (2\,\psi_+^2 - 1)\,. \tag{4.32}$$

The straightforward consequence is that this configuration enables independent control of W_E and K by using $\mathcal{C}_1(\zeta\,,\,\psi_+)$ and $\mathcal{D}(\psi_+)$, respectively. Additionally, the quantity $\mathcal{D}(\psi_+)$ is complementary to the concurrence C, as it can be shown that they obey the following relation:

$$\big(\,\mathcal{D}(\psi_+)\,\big)^2\;+\;\big(\,C\,\big)^2\;=\;1\,. \tag{4.33}$$

Indeed, this is in accordance with the proportionality between $\mathcal{D}(\psi_+)$ and the S_3 Stokes parameter, as eq. 4.33 indicates that $\mathcal{D}(\psi_+)$ quantifies the relative intensity of each circular polarization state component, which correspond to unentangled states with $C = 0$.

Before proceeding with the analysis, it is useful to define the dimensionless chirality density and electrical intensity distributions, which will be denoted with a bar over each symbol. The dimensionless electric intensity distribution $\overline{W}_E$ as well as the two corresponding polarization contributions $\overline{W}_E^{(+,-1)}$ and $\overline{W}_E^{(\mathrm{cross},-1)}$ (pure circular and cross-polarization terms, respectively) are defined as follows:

$$\begin{aligned}\overline{W}_E\,(\mathbf{r}) &= \left(\frac{2}{k\,\gamma\,w_0\,E_0}\right)^2\left(\frac{2}{\epsilon_1}\right)\left(W_E^{(+,-1)} + 2\,\mathcal{C}_1(\zeta\,,\,\psi_+)\,W_E^{(\mathrm{cross},-1)}\right) = \\ &= \left(\overline{W}_E^{(+,-1)}\right) + 2\,\mathcal{C}_1(\zeta\,,\,\psi_+)\left(\overline{W}_E^{(\mathrm{cross},-1)}\right). \end{aligned} \tag{4.34}$$

Using eqs. 4.22, 4.24 and 4.31, the expressions for $\overline{W}_E^{(+,-1)}$ and $\overline{W}_E^{(\mathrm{cross},-1)}$ in terms of the $I_m^{(-1)}$ functions can be easily obtained. In a similar fashion, eq. 4.26 can be used to define the dimensionless chirality density $\overline{K}$ as:

$$\overline{K}(\mathbf{r}) = \left(\frac{2}{k\,\gamma\,w_0\,E_0}\right)^2\left(\frac{2}{\epsilon_1}\right)\left(\frac{1}{2\,k}\right)K(\mathbf{r}) = \mathcal{D}(\psi_+)\,\overline{W}_E^{(+,-1)}\,. \tag{4.35}$$

The dimensionless quantities we have just defined are crucial for the following qualitative analyses and comparisons between the optical force evaluated using the MDSA theory and the expected behavior from the dipole limit. We illustrate the behavior of $\overline{W}_E^{(+,-1)}$ and $\overline{W}_E^{(\mathrm{cross},-1)}$ in Fig. 4.3(a). A few different intensity distribution configurations resulting from different values of $\mathcal{C}_1$ are shown in Fig. 4.3(b). We have set $\psi_+ = \psi_-$ in Fig. 4.3(b) for two reasons: the first is that the chiral force component vanishes as $\mathcal{D} = 0$ and the second is that this corresponds to the scenario where $\mathcal{C}_1$ can assume the widest possible range of values $\mathcal{C}_1 \in [-0.5,\,0.5]$.

We shall use this configuration to analyze the isolated achiral component of the optical force. By symmetry, the (first) derivative of $\overline{W}_E$ with respect to ρ on the axis is always zero for aberration-free fields. By evaluating the second derivative of $\overline{W}_E$ with respect to ρ, denoted by $\partial_\rho^2\overline{W}_E$, we obtain a quantity that is directly related to the achiral transverse trap stiffness κ_ρ. Each $\overline{W}_E$ represented in Fig. 4.3(b) will provide a different achiral force on a dipole, whether the dipole is chiral or not. The values of $\mathcal{C}_1$ used in the figure present three interesting cases. In the cases where $\mathcal{C}_1 = (0.5)$ and $\mathcal{C}_1 = (0.309)$, the achiral gradient force is expected to trap a dipolar particle on top of the optical axis $\rho = 0$,

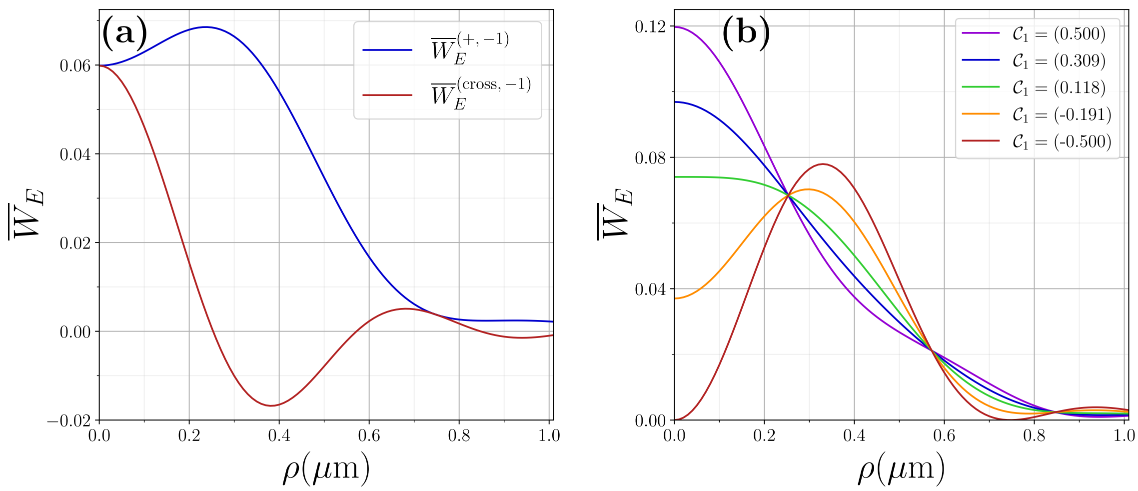

Figure 4.3: Behavior of $\overline{W}_E$ for various combinations of $\overline{W}_E^{(+,-1)}$ and $\overline{W}_E^{(\mathrm{cross},-1)}$. Panel (a) depicts the behavior of $W_E^{(+,-1)}$ and $W_E^{(\mathrm{cross},-1)}$ as a function of the radial coordinate ρ. As both components are independent of ϕ when $\ell = 1$, the field in the xy-plane can be obtained by revolving the plotted functions around the $\rho = 0$ axis. Panel (b) shows 5 different configurations for different values of $\mathcal{C}_1$, with each of the respective values indicated in the legend (rounded to 3 decimal places).

which means that κ_ρ is positive and $\partial_\rho^2 \overline{W}_E$ is negative. On the other hand, both the cases $\mathcal{C}_1 = (-0.191)$ and $\mathcal{C}_1 = (-0.5)$ exhibit an off-axis intensity maximum, each at a different ρ coordinate, which leads to a positive $\partial_\rho^2 \overline{W}_E$ value as well as an off-axis trapping scenario.

The intermediate value of $\mathcal{C}_1 = (0.118)$ generates a field with a rare characteristic: the gradient force is zero for a large section of the radial coordinate. $\overline{W}_E$ forms an intensity plateau near the optical axis, meaning that $\partial_\rho^2 \overline{W}_E \sim 0$ on the vicinity of $\rho = 0$. In other words, the achiral reactive force will be approximately zero for a range of ρ values near the axis. However, the chiral reactive force in this region will not necessarily be zero, as it depends on the energy distribution $W_E^{(+,-1)}$. This means that, in addition to being able to control the chiral and achiral components of the optical force separately, the hybrid beams we are discussing also allow us to isolate the chiral force, or even have a radial force component that is exclusively chiral. The variation of $\partial_\rho^2 \overline{W}_E$ as a function of $\mathcal{C}_1$ is depicted in Fig. 4.4(a) for the case $\psi_+ = \psi_-$.

Since $\mathcal{D}(\psi_+)$ is the quantity that controls the chiral interaction strength, setting

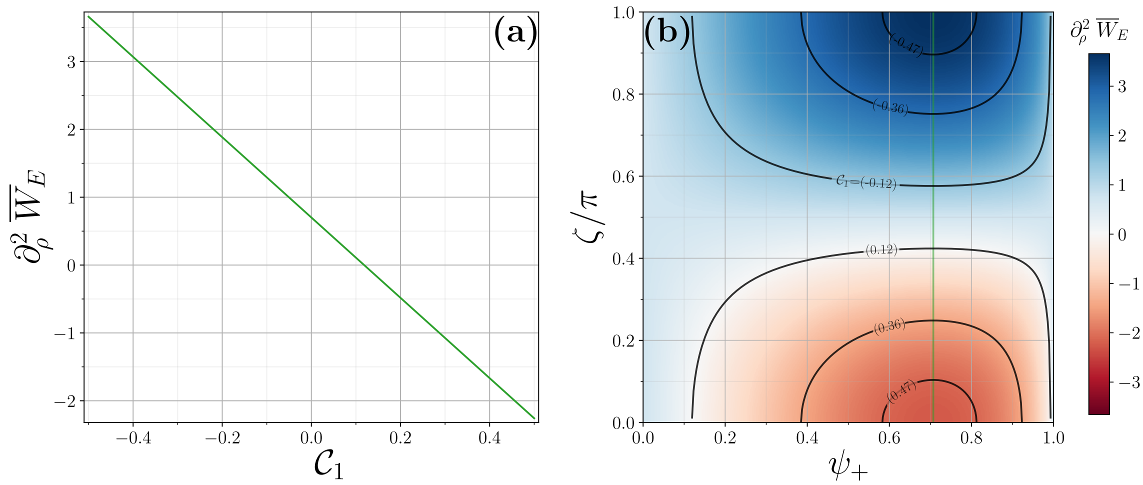

Figure 4.4: Behavior of $\partial_\rho^2\overline{W}_E$ as a function of $\mathcal{C}_1$, ζ/π and ψ_+. Panel (a) illustrates the "achiral" case $\psi_+ = \psi_-$, where the range of possible values of $\mathcal{C}_1$ is maximal. Panel (b) is a density plot of $\partial_\rho^2\overline{W}_E$ evaluated in the $(\psi_+\,,\,\zeta)$ parameter space. The relation between color and value is given by the color bar on the right. The numerical value of $\partial_\rho^2\overline{W}_E$ has the dimension of $(\mu\mathrm{m})^{-1}$ (omitted) on both panels. The green curve on Panel (b) corresponds to the achiral case ($\psi_+ = \sqrt{0.5}$) depicted in Panel (a), while the black curves represent the lines where $\mathcal{C}_1$ is constant (depicted values are rounded to 2 decimal places).

$\psi_+ \neq \psi_-$ makes the chiral force contribution reappear. Additionally, the range of possible $\mathcal{C}_1$ values becomes slightly narrower. Therefore, in the context of optical chiral forces, it is more meaningful to obtain the range of possible values for ψ_+ for a given value of $\mathcal{C}_1$ instead of the other way around. The maximum value of ψ_+ as a function of $\mathcal{C}_1$ can be obtained by solving eq. 4.31 for ψ_+ with $\zeta = 0$ (when $\mathcal{C}_1 > 0$) or $\zeta = \pi$ (when $\mathcal{C}_1 < 0$), yielding:

$$\psi_+^{(\max)} = \sqrt{\frac{1 + \sqrt{1 - 4\,\mathcal{C}_1^2}}{2}}\,. \tag{4.36}$$

The minimum value of ψ_+ should correspond to the maximum value of the associated ψ_- component. In other words, it is true that $\left(\psi_+^{(\min)}\right)^2 = 1 - \left(\psi_+^{(\max)}\right)^2$, since $\psi_-^{(\max)} = \psi_+^{(\max)}$ by symmetry. The phase ζ that provides the desired $\mathcal{C}_1$ for a given ψ_+ (bounded by eq. 4.36) is also straightforward to compute:

$$\zeta\,(\mathcal{C}_1\,,\,\psi_+) = \arccos\left(\mathcal{C}_1 \Big/ \sqrt{\psi_+^2 - \psi_+^4}\right). \tag{4.37}$$

The values of $\partial_\rho^2\overline{W}_E$ in the $(\psi_+\,,\,\zeta)$ parameter space are depicted in Fig. 4.4(b). The black lines over the color map (density plot) are calculated using eq. 4.37 within the range delimited by eq.4.36 and indicate the regions for which $\mathcal{C}_1$ is constant (and therefore $\overline{W}_E$ and all its derivatives are also unchanged). The green line in Fig. 4.4(b) represents the "achiral" configuration $\psi_+ = \psi_- = \sqrt{0.5}$. From this plot, it becomes clear that the $\psi_+ = \psi_-$ case is indeed the one with the wider interval of possible values for $\mathcal{C}_1$. The special case $\mathcal{C}_1 \simeq (0.11843)$ for which $\partial_\rho^2 \overline{W}_E = 0$ (represented as $\mathcal{C}_1 = (0.12)$ in Fig. 4.4(b) and as $\mathcal{C}_1 = (0.118)$ in Fig. 4.3(b), both due to rounding) admits a maximum ψ_+ value of $\psi_+^{(\max)} \simeq 0.9929$, which is quite close to one and therefore optimal if we desire to maximize the chiral force in the absence of the achiral component.

In Fig. 4.5(a) we compare $\overline{W}_E$ and $\overline{K}$ side-by-side, together with their respective derivatives with respect to ρ (which is proportional to the radial reactive force component), in order to illustrate how the chiral force will dominate over the achiral contribution within the radial $\overline{W}_E$ plateau range. Using the MDSA theory, we computed Q_ρ as a function of ρ and plotted it for different values of the parameter κ in Fig. 4.5(b). As expected, particles with positive values of κ were attracted to the off-axis chirality density maximum shown in Panel (a). If the values of ψ_+ and ψ_- were swapped, the chiral density $\overline{K}$ would flip its sign and particles with negative values of κ would be pulled off-axis instead. The inset in Panel (b) zooms in the region from $\rho = 0$ to $\rho = 0.1\mu$m, where we can see that different positive values of κ lead to different radial equilibrium positions $\rho_{\text{eq.}}$, whereas $\kappa \leq 0$ always leads to $\rho_{\text{eq.}} = 0$. In other words, chiral dipoles with different handedness (κ sign) will be separated by this chiral force and will exhibit distinct axial equilibrium positions depending on the magnitude and relative sign of both κ and $\overline{K}$. We call this effect enantioseparation, which is a topic of great interest in the fields of optical chirality (chiral light-chiral matter interactions), nano-sciences, and other sectors such as the chemical and pharmaceutical industries.

In order to obtain an optical force behavior that is consistent with the electric intensity and chiral density distributions, the sphere radius used in Fig. 4.5(b) was chosen in

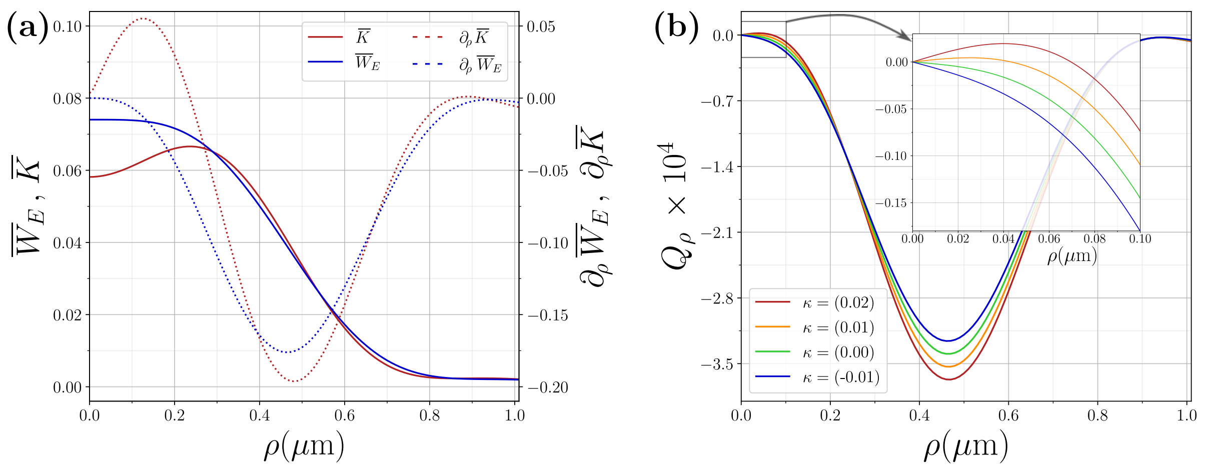

Figure 4.5: Optical forces for a system with $\mathcal{C}_1 = (0.11843)$ and $\psi_+ = \psi_+^{(\max)}(\mathcal{C}_1 = 0.11843) \simeq 0.9929$. Panel (a) shows $\overline{W}_E$ and $\overline{K}$ (solid lines) as well as their derivatives with respect to ρ (dotted lines). Panel (b) shows the radial component of the efficiency factor Q_ρ as a function of ρ for 4 distinct values of κ and radius $a = 0.05\mu$m.

accordance with the dipole approximation: $a = 0.05\,\mu\mathrm{m} \ll \lambda_0 = 1.064\,\mu\mathrm{m}$. This was useful for both testing the numerical implementation for consistency with a well-known limit as well as predicting the optical force landscape from intuitive guesses based on the evaluation of $\overline{W}_E$ and $\overline{K}$.

A natural question that may arise from the results contained in Fig. 4.5 is whether the enantioseparation effect remains for larger radii. If it does, how does the radial equilibrium position $\rho_{\mathrm{eq.}}$ depend on κ for each radius value, or how does it depend on the radius a for a given fixed κ? In Fig. 4.6 we show how the radial equilibrium position $\rho_{\mathrm{eq.}}$ varies with κ for 5 different sphere radii. Indeed, the enantioseparation effect does remain for larger radii, but only for increasingly larger values for κ. For each of the curves, there is a different κ threshold above which the sphere ceases to be trapped on-axis. As κ increases, so does $\rho_{\mathrm{eq.}}$, and as the radius a increases, so does the κ threshold.

In order to circumvent this limitation, we can repeat the procedure to minimize the achiral force component using the MDSA theory instead of the dipole limit picture. In Fig. 4.7, we plot the behavior of the transverse trap stiffness κ_ρ as a function of the sphere radius a and the parameter $\mathcal{C}_1$, taking $\psi_+ = \psi_-$ (or alternatively $\kappa = 0$). To

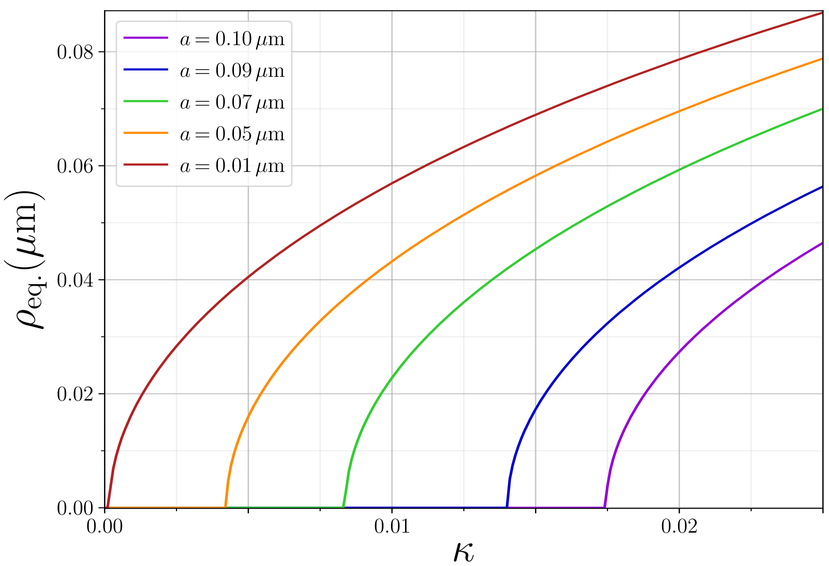

Figure 4.6: Radial equilibrium position $\rho_{\text{eq.}}$ as a function of the chirality parameter κ for different sphere sizes and a fixed value for $\mathcal{C}_1$. As the sphere radius value a increases, the minimum value (threshold) of κ for which off-axis trapping onsets also grows.

illustrate the validity range of the dipole limit, we plot κ_ρ and κ_ρ/a^3 in panels (a) and (b), respectively. In the dipole limit, κ_ρ/a^3 remains a constant for any a, which can only be seen in the region of very small radii ($a \ll 0.1\,\mu$m) in Fig. 4.7(b). The green curve on both panels corresponds to the values of the parameter space that render $\kappa_\rho = 0$. This curve corresponds to the function $\mathcal{C}_1(a)$ defined as the value for $\mathcal{C}_1$ required to have $\kappa_\rho = 0$ for each values of the radius a. For very small values of a, we find $\mathcal{C}_1(a) \approx 0.12$ in agreement with the dipole limit discussed earlier (see also panel (b) of Fig. 4.8). As the radius grows, the function $\mathcal{C}_1(a)$ starts to deviate from the initial dipolar value, indicating that the dipole limit is no longer valid.

Using the function $\mathcal{C}_1(a)$ and the maximum allowed value for ψ_+ as given by eq. 4.36 so as to maximize the chiral component of the force, we can proceed to calculate the new values of ρ_{eq} as a function of κ for the same radii of Fig. 4.6. This novel optimized configuration renders radial equilibrium positions with no threshold values for κ, as depicted in panel (a) of Fig. 4.8. In panel (b) of Fig. 4.8, we plot the green curve contained in both panels of Fig. 4.7, but for the shorter range of radius values used in Fig. 4.8(a).

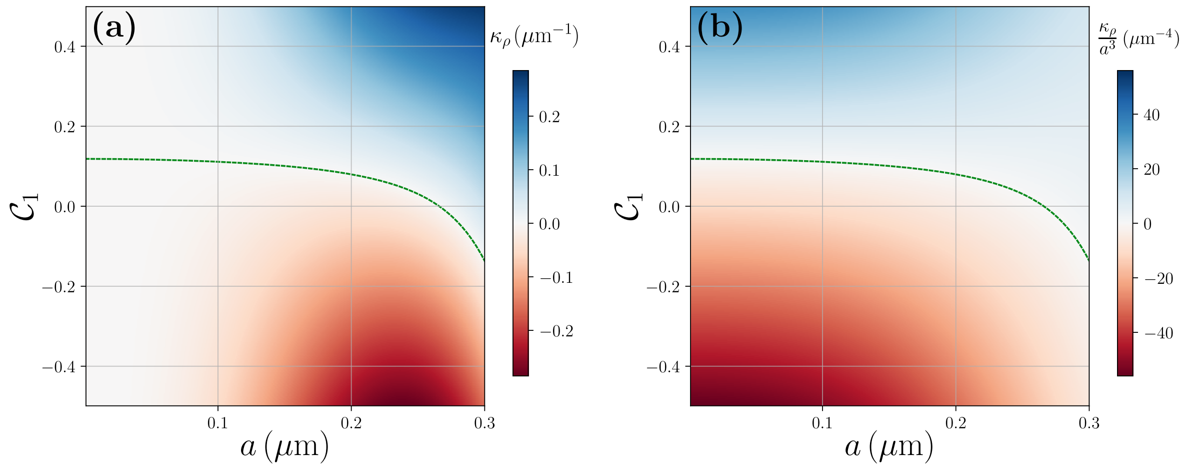

Figure 4.7: Density plots of the transverse trap stiffness κ_ρ as a function of $\mathcal{C}_1$ and the sphere radius a. In panel (a), we plot $\kappa_\rho(\mu\mathrm{m}^{-1})$, while in panel (b) we plot $\frac{\kappa_\rho}{a^3}(\mu\mathrm{m}^{-4})$ to illustrate the deviation from the dipole approximation validity region. The green line in both panels is the set of values of $\mathcal{C}_1$ as a function of a for which $\kappa_\rho = 0$. Additionally, we set $\psi_+ = \psi_- = \sqrt{0.5}$ (or equivalently $\kappa = 0$) so that the graph corresponds to the achiral part of the optical force.

In the inset of Fig. 4.8, we repeat the main plot in a log-log graph, which exhibits a linear behavior for all radii shown in the figure, indicating a power law dependency between the axial equilibrium position ρ_{eq} and the chirality parameter κ:

$$\rho_{\mathrm{eq.}} \approx (B)\,\kappa^{(A)}\,. \tag{4.38}$$

By fitting the data, we find that the power law in eq. 4.38 is the same for all radii we have considered: $A \approx (0.482)$, whilst the linear coefficient varied in the range $(-0.70) < B < (-0.64)$.

As an endnote for this chapter, it is worth noting that the possibilities of enantioseparation of nano- and micro-particles and the characterization of other aspects of the system were not totally explored for the optical trapping system presented here. For example, we didn't consider configurations that would present only off-axis trapping states, which can be easily done by choosing a proper value of $\mathcal{C}_1$, like $\mathcal{C}_1 = (-0.191)$ in Fig. 4.3(b). A natural candidate for this kind of off-axis trapping system would be $\mathcal{C}_1 = (0.0)$, which yields the same spatial distribution configuration for both the electric field intensity W_E and

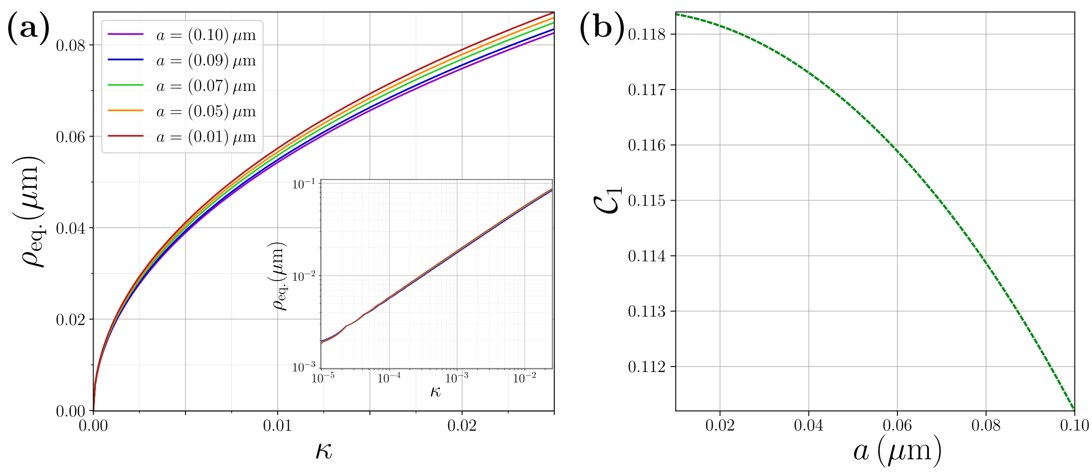

Figure 4.8: Radial equilibrium position $\rho_{\text{eq.}}$ as a function of the chirality parameter κ for different sphere sizes using optimized values of $\mathcal{C}_1(a)$. Panel (a) shows the radial equilibrium position $\rho_{\text{eq.}}$ for the same radii as Fig. 4.6, while using the $\mathcal{C}_1$ values of Fig. 4.7. The inset of panel (a) repeats the plot in a log-log graph, indicating that of $\rho_{\text{eq.}}(\kappa)$ follows a power law. Panel (b) shows the same function $\mathcal{C}_1(a)$ presented in Fig. 4.7, but for the radius range used in panel (a).

the chirality density K, according to eq. 4.34. Additionally, this is the system in which we can achieve the maximum absolute value of the chirality density (*i.e.* the cases where $\psi_{\pm}^{(\text{max})} = 1$ in eq. 4.36), corresponding to purely circular polarized input vortex beams. In other words, this configuration presents the possibility of a trapping system with exclusive off-axis trapping states and continuous control of the chirality density that does not disturb or change the achiral part of the field. The two main observables would be the rotation period and the rotation orientation. Both of them depend on the azimuthal optical force component, as discussed in sec. A.2 of appendix A, and are expected to exhibit a great dependence on the particle's chirality parameter κ. In Fig. 4.9, we show how the azimuthal component of the optical force varies as a function of ψ_+^2 for a sphere radius of $a = 0.05\mu$m and various values of κ. We set the relative phase as $\zeta = (\pi/2)$ so that $\mathcal{C}_1 = 0$, rendering an intensity distribution identical to the pure circular polarization state case. We can see that even when $\mathcal{D} = 0$ (or $\psi_+^2 = 0.5$), spheres with different κ behave differently, probably due to the properties of the dissipative chiral force components. Indeed, the sign of Q_ϕ is the opposite of the chirality parameter κ, which is an

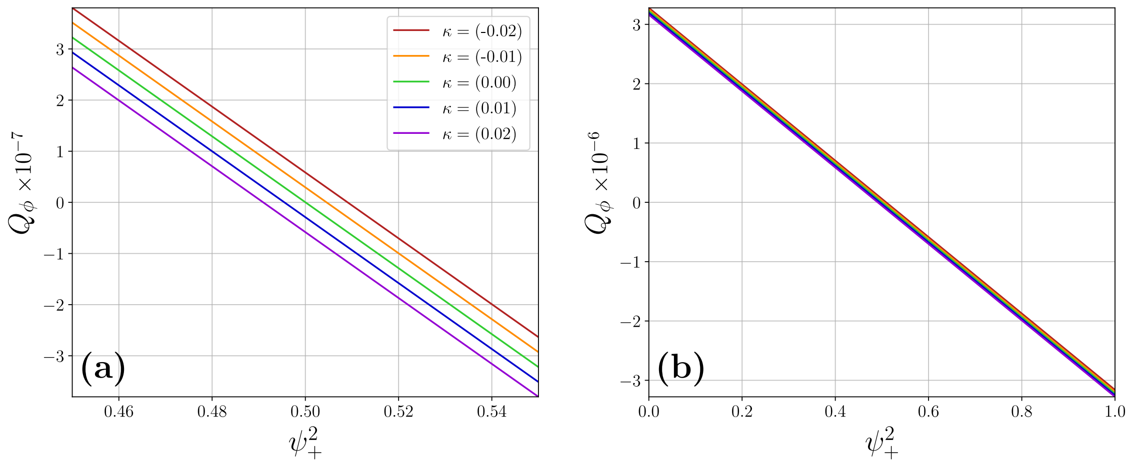

Figure 4.9: Behavior of the azimuthal component of the efficiency factor Q_ϕ as a function of ψ_+^2, for various values of κ and $\mathcal{C}_1 = 0$. We consider a sphere radius of $a = 0.05\mu$m, and we take $\zeta = (\pi/2)$. Panel (a) depicts values of ψ_+^2 ranging from 0.45 to 0.55, while ψ_+^2 in panel (b) ranges from 0.0 to 1.0 .

unexpected behavior if we analyze the chirality density alone. Also, this behavior was not observed in the simulations of optical forces with tightly focused circularly polarized vortex beams, which are discussed in sec. A.2.

A second example is to use the characterization of κ_ρ as a function of $\mathcal{C}_1$ and a, presented in Fig. 4.7(a), to estimate the radius of a nano- or micro-sphere (with radius values $a < 0.3\mu$m). This characterization method would be independent of the chirality parameter of the particle, as we can always set $\psi_+ = \psi_- = \sqrt{0.5}$, rendering a radial force component which is insensitive to chirality.

A last and broader example is to employ larger spheres (compared to the ones presented above) and additional topological charge values (*i.e.* $\ell \neq 1$) in this trapping system. The behavior of larger spheres in vortex beams is treated in both projects described in appendix A, which serves as examples and inspirations to future applications using the hcVVBs trapping system presented above. When considering any $\ell \neq 1$, the symmetry of rotation around the optical axis would be lost, rendering a much more complex trapping system that would require a completely different approach from the one presented in this chapter.

Chapter 5

Conclusion and final remarks

In this final Chapter, we take a few steps back and contemplate how the works within this thesis fit in the present scientific and technological big picture. In today's world, fields of knowledge such as nano-optics, photonics, and optomechanics are closely intertwined with the most advanced technologies in the semiconductor, nanotechnology, and pharmaceutical industries. Silicon-based microchips are produced using lithography with beams focused beyond the paraxial limit, and defects caused by optical aberrations are a source of multimillion-dollar losses. Research in nanotechnology and nanoscience seeks new materials that increase energy production efficiency. In the pharmaceutical industry, the production process of chiral molecules can yield the enantiomer of the desired drug as a byproduct, necessitating an additional and typically quite expensive process of enantiomeric separation from the racemic mixture. In this thesis, we presented various uses and applications of optical tweezers while addressing topics crucial to the aforementioned fields, such as the modeling and characterization of complex non-paraxial beams, the description of light scattering by micro- and nano-scale objects, and light-matter interaction in several distinct scenarios. We believe that the advances and results contained in this thesis will contribute to the scientific community and technological progress with new tools and resources for characterization, modeling, simulation, and validation of physical systems.

In Chapter 2, we introduced quantitative guidelines for implementing optical tweezers using vortex beams and characterized the possible trapping configurations. Additionally, we provided an introductory discussion of the Langevin equation, which governs the stochastic dynamics of the systems we addressed in this work. Throughout the thesis, we employ the concepts discussed in this chapter, such as the filling condition for ring-shaped beams and predictions of the trapping configuration based on the relationships between the trapping beam's ring size and the size of the trapped object.

In Chapter 3, we explored the novel bistable trapping configuration, presenting experimental and theoretical results that point to a deep understanding of the physical system. This was the first and perhaps most important result of my thesis, as it was the product of experimental, theoretical, and numerical work, leading to a unique understanding of the system we modeled and implemented in the laboratory. Beyond being a significant source of learning, this system is potentially important in the study of single-particle thermodynamics, also referred to as stochastic thermodynamics. In this context, the orbital trapping state present in the bistable system is a canonical example of NESS, where the system produces entropy by constantly dissipating energy to the environment in the form of the so-called housekeeping heat. The landscape of the optical force field in the bistable system presents two stable positions in which the microsphere alternates. This image of a particle hopping between two trapping states recalls Kramers' reaction rate (or passage time) problem for a bistable potential. Kramers' passage time theory was derived assuming a stochastic system in a one-dimensional potential obeying a Fokker-Planck equation. Although its objective was to model chemical reactions, this theory is also valid for any colloidal system following the same initial assumptions. However, the transition time provided by Kramers' theory for the effective potential we calculated for our bistable system shows a significant disagreement. One possibility for future work involving this system is to explore in more detail the reasons for the discrepancy between Kramers' theory and our experimental results. Additionally, we can investigate connections between this disagreement and the energy dissipation through other internal degrees of freedom by the

NESS, or due to the force field not being completely conservative and being immersed in 3 dimensions.

In Chapter 4, we presented a novel theory for the force of an exotic beam on a chiral spherical particle. With this theory, we proposed a new method for the enantioseparation of particles at sub-micrometer scales. We demonstrated that we can independently and very flexibly control different characteristics of this field, such as the distributions of energy and chirality of light. It's worth mentioning three paths we didn't explore, as well as their implications: the optical force behavior for a broader range of $\mathcal{D}$ and $\mathcal{C}_1$ configurations, for larger radii values, and for ℓ values different from 1. We can analyze the behavior of spheres trapped in the axial regime within the parameter space of Fig.4.3(b) using Brownian dynamics simulations of the torque experiment. This can be especially useful for addressing the case of microspheres with large radii, which will inevitably be trapped along the axis and from which we expect a stronger chiroptical response compared to smaller microspheres. Additionally, the different torque data in the parameter space of Fig.4.3(b) can be used to characterize other optical parameters (other than the matter chirality) of the microsphere. This discussion extends to cases where $\ell \neq 1$ and the field's azimuthal symmetry is broken. Beyond characterization applications, fields that break azimuthal symmetry can be used in the context of stochastic thermodynamics to produce NESS superimposed with a potential having periodic minima (see ref. [34]), which demonstrates the great versatility that this family of exotic beams provides.

In Appendix A, we present the works on which I collaborated, involving members of the LPO group and international colleagues. We presented two methods for the quantitative characterization of experimental system parameters. Additionally, we discussed a system that demonstrates the operation of finite-time thermal protocols for single particles using an optical tweezers experiment. Finally, in Appendix B, we present details on the derivation of the MDSA theory, and present the expressions for the model describing three distinct optical trapping systems. The first system employs circularly polarized vortex beams, and was used in Chapters 2 and 3, and also in Sec. A.1. The second trapping system model employs the hcVVBs, discussed in Chapter 4. The last model discussed in this appendix employs circularly polarized vortex beams possessing astigmatism aberration, which was also used in Sec. A.1. Additionally, we discussed the convergence criteria required by the MDSA model accounting for the beam astigmatism.

Bibliography

[1] B. Richards and E. Wolf. Electromagnetic diffraction in optical systems, II. structure of the image field in an aplanatic system. Proceedings of the Royal Society of London. Series A. Mathematical and Physical Sciences, 253(1274):358–379, dec 1959. 5, 9

[2] C. F. Bohren and D. R. Huffman. Absorption and Scattering of Light by Small Particles. Wiley, 1998. 6, 22

[3] Ioannis Karatzas and Steven E. Shreve. Brownian motion and stochastic calculus. Springer study edition. Springer, New York, NY, corr. softcover 2. ed., [nachdr.] edition, 2009. 6

[4] N. G. Kampen. Stochastic Processes in Physics and Chemistry. North-Holland Personal Library. Elsevier Science & Technology, Amsterdam, 3rd ed. edition, 2011. Description based on publisher supplied metadata and other sources. 6, 59

[5] Rémi Goerlich, Minghao Li, Samuel Albert, Giovanni Manfredi, Paul-Antoine Hervieux, and Cyriaque Genet. Noise and ergodic properties of brownian motion in an optical tweezer: Looking at regime crossovers in an ornstein-uhlenbeck process. Physical Review E, 103(3):032132, March 2021. 6

[6] Lukas Novotny and Bert Hecht. Principles of Nano-Optics. Cambridge University Press, 2 edition, 2012. 9, 11, 45

[7] Paula B. Monteiro, Paulo A. Maia Neto, and H. Moysés Nussenzveig. Angular momentum of focused beams: Beyond the paraxial approximation. Physical Review A, 79:033830, Mar 2009. 9, 15, 28, 73

[8] N. B. Viana, M. S. Rocha, O. N. Mesquita, A. Mazolli, P. A. Maia Neto, and H. M. Nussenzveig. Towards absolute calibration of optical tweezers. Physical Review E, 75(2), feb 2007. 10, 52

[9] R. S. Dutra, P. A. Maia Neto, H. M. Nussenzveig, and H. Flyvbjerg. Theory of optical-tweezers forces near a plane interface. Physical Review A, 94(5):053848, 2016. 11

[10] Paula Borges Monteiro. Feixes de Luz não-paraxiais com momento angular orbital e aplicações às pinças ópticas. PhD thesis, Universidade Federal do Rio de Janeiro, 2009. 12

[11] Joseph W. Goodman. Introduction to Fourier optics. Roberts & Company, Englewood, Colorado, third edition edition, 2005. Includes bibliographical references (p. 465 - 479) and index. 14

[12] P. A. Maia Neto and H. M Nussenzveig. Theory of optical tweezers. Europhysics Letters (EPL), 50(5):702–708, jun 2000. 19, 23

[13] A. Mazolli, P. A. Maia Neto, and H. M. Nussenzveig. Theory of trapping forces in optical tweezers. Proceedings of the Royal Society of London. Series A: Mathematical, Physical and Engineering Sciences, 459(2040):3021–3041, dec 2003. 19, 23, 124

[14] Arthur Ashkin, editor. Optical trapping and manipulation of neutral particles using lasers. World Scientific, Hackensack, NJ, 2006. Includes bibliographical references. 19

[15] D A Varshalovich, A N Moskalev, and V K Khersonskii. Quantum Theory of Angular Momentum. WORLD SCIENTIFIC, October 1988. 19

[16] A. Mazolli. Teoria das Pinças Óticas. PhD thesis, Universidade Federal do Rio de Janeiro, 2003. 21, 22, 23, 24

[17] H. C. van de Hulst. Light Scattering by Small Particles. Dover Publications Inc., 1981. 22

[18] Rafael de Sousa Dutra. Parametrizando uma Pinça Ótica: Efeitos de Aberrações e Absorção. PhD thesis, Universidade Federal do Rio de Janeiro, 2011. 22, 120

[19] A. Ashkin. Forces of a single-beam gradient laser trap on a dielectric sphere in the ray optics regime. Biophysical Journal, 61(2):569–582, feb 1992. 24

[20] NIST Digital Library of Mathematical Functions. http://dlmf.nist.gov/10, release 1.1.7 of 2022-10-15, edited by F. W. J. Olver, A. B. Olde Daalhuis, D. W. Lozier, B. I. Schneider, R. F. Boisvert, C. W. Clark, B. R. Miller, B. V. Saunders, H. S. Cohl, and M. A. McClain, 2022. 25, 121, 124

[21] Jack Ng, Zhifang Lin, and C. T. Chan. Theory of optical trapping by an optical vortex beam. Physical Review Letters, 104:103601, Mar 2010. 26

[22] Lei-Ming Zhou, Ke-Wen Xiao, Jun Chen, and Nan Zhao. Optical levitation of nanodiamonds by doughnut beams in vacuum. Laser & Photonics Reviews, 11(2):1600284, 2017. 26

[23] Yuanjie Yang, Yu-Xuan Ren, Mingzhou Chen, Yoshihiko Arita, and Carmelo Rosales-Guzmán. Optical trapping with structured light: a review. Advanced Photonics, 3(03), may 2021. 26

[24] K Volke-Sepulveda, V Garcés-Chávez, S Chávez-Cerda, J Arlt, and K Dholakia. Orbital angular momentum of a high-order Bessel light beam. Journal of Optics B: Quantum and Semiclassical Optics, 4(2):S82, mar 2002. 26

[25] Jennifer E. Curtis and David G. Grier. Structure of optical vortices. Physical Review Letters, 90:133901, Apr 2003. 26, 28, 51

[26] Yohai Roichman, Bo Sun, Allan Stolarski, and David G. Grier. Influence of nonconservative optical forces on the dynamics of optically trapped colloidal spheres: The fountain of probability. Physical Review Letters, 101:128301, Sep 2008. 26

[27] Yohai Roichman, Bo Sun, Yael Roichman, Jesse Amato-Grill, and David G. Grier. Optical forces arising from phase gradients. Phys. Rev. Lett., 100:013602, Jan 2008. 26

[28] M. I. M. Feitosa and O. N. Mesquita. Wall-drag effect on diffusion of colloidal particles near surfaces: A photon correlation study. Physical Review A, 44(10):6677–6685, nov 1991. 32, 110

[29] E. Schäffer, S. F. Nørrelykke, and J. Howard. Surface forces and drag coefficients of microspheres near a plane surface measured with optical tweezers. Langmuir, 23:3654, 2007. 32, 110

[30] Edward Nelson. Dynamical theories of Brownian motion, volume 101. Princeton University Press, 2020. 33

[31] Christopher Chatfield. The analysis of time series. Texts in statistical science. Chapman & Hall, London [u.a.], 4. ed., repr edition, 1995. 35

[32] Peter E. Kloeden and Eckhard Platen. Numerical solution of stochastic differential equations. Number 23 in Applications of mathematics. Springer, Berlin, corrected third printing edition, 2010. 38

[33] Albert Einstein. Investigations on the theory of the Brownian movement. Dover Publ., New York, repr. of methuen ed. 1926 edition, 1967. Hier auch später erschienene, unveränderte Nachdrucke. 38

[34] Udo Seifert. Stochastic thermodynamics, fluctuation theorems and molecular machines. Reports on Progress in Physics, 75(12):126001, nov 2012. 40, 91

[35] S. Ciliberto. Experiments in stochastic thermodynamics: Short history and perspectives. Physical Review X, 7:021051, Jun 2017. 40

[36] Luís Barbosa Pires, Rémi Goerlich, Arthur Luna da Fonseca, Maxime Debiossac, Paul-Antoine Hervieux, Giovanni Manfredi, and Cyriaque Genet. Optimal time-entropy bounds and speed limits for brownian thermal shortcuts. Physical Review Letters, 131(9):097101, Sep 2023. 40

[37] Carmelo Rosales-Guzmán and Andrew Forbes. How to shape light with spatial light modulators. SPIE Press, 2017. 41

[38] Kainã Diniz, Tanja Schoger, Guilherme T. Moura, Arthur L. Fonseca, Diney S. Ether, Rafael S. Dutra, Gert-Ludwig Ingold, Nathan B. Viana, and Paulo A. Maia Neto. Precise in situ radius measurement of individual optically trapped microspheres using negative optical torque exerted by focused vortex beams. Physical Review A, 110:013513, Jul 2024. 45, 104, 106

[39] Paolo Polimeno, Alessandro Magazzù, Maria Antonia Iatì, Francesco Patti, Rosalba Saija, Cristian Degli Esposti Boschi, Maria Grazia Donato, Pietro G. Gucciardi, Philip H. Jones, Giovanni Volpe, and Onofrio M. Maragò. Optical tweezers and their applications. Journal of Quantitative Spectroscopy and Radiative Transfer, 218:131–150, oct 2018. 45

[40] Lukas Novotny, Robert D. Grober, and Khaled Karrai. Reflected image of a strongly focused spot. Optics Letters, 26(11):789, jun 2001. 45

[41] Arthur L. da Fonseca, Kainã Diniz, Paula B. Monteiro, Luís B. Pires, Guilherme T. Moura, Mateus Borges, Rafael S. Dutra, Diney S. Ether, Nathan B. Viana, and Paulo A. Maia Neto. Tailoring bistability in optical tweezers with vortex beams and spherical aberration. Physical Review Research, 6(2):023226, June 2024. 46, 54, 56

[42] F. Gómez, R.S. Dutra, L.B. Pires, Glauber R. de S. Araújo, B. Pontes, P.A. Maia Neto, H.M. Nussenzveig, and N.B. Viana. Nonparaxial mie theory of image formation in optical microscopes and characterization of colloidal particles. Physical Review Applied, 15:064012, Jun 2021. 47

[43] Yang Li, Lei-Ming Zhou, and Nan Zhao. Anomalous motion of a particle levitated by Laguerre–Gaussian beams. Opt. Lett., 46(1):106–109, Jan 2021. 51

[44] K. Diniz, R. S. Dutra, L. B. Pires, N. B. Viana, H. M. Nussenzveig, and P. A. Maia Neto. Negative optical torque on a microsphere in optical tweezers. Opt. Express, 27(5):5905–5917, Mar 2019. 51, 72, 77, 104, 106

[45] Aristide C. Dogariu and Raj Rajagopalan. Optical traps as force transducers: The effects of focusing the trapping beam through a dielectric interface. Langmuir, 16(6):2770–2778, 03 2000. 52

[46] Max Born and Emil Wolf. Principles of Optics. Cambridge University Press, 2019. 54, 108

[47] Y. Roichman, A. Waldron, E. Gardel, and D. G Grier. Optical traps with geometric aberrations. Applied Optics, 45(15):3425–3429, 2006. 57

[48] R. S. Dutra, N. B. Viana, P. A. Maia Neto, and H. M. Nussenzveig. Absolute calibration of forces in optical tweezers. Physical Review A, 90(1):013825, jul 2014. 57

[49] Giovanni Milione, H. I. Sztul, D. A. Nolan, and R. R. Alfano. Higher-order poincaré sphere, stokes parameters, and the angular momentum of light. Physical Review Letters, 107(5):053601, July 2011. 60, 79

[50] R. Fickler, L. Kopf, and M. Ornigotti. Higher-order poincaré spheres and spatiospectral poincaré beams. Physical Review Research, 6(3):033298, September 2024. 61

[51] Chao Chen, Yu Zhang, Li Ma, Yuqin Zhang, Zhenhua Li, Ruirui Zhang, Xiangyu Zeng, Zijun Zhan, Changwei He, Xiaorong Ren, Chuanfu Cheng, and Chunxiang Liu. Flexible generation of higher-order poincaré beams with high efficiency by manipulating the two eigenstates of polarized optical vortices. Optics Express, 28(7):10618, March 2020. 61

[52] L. J. Pereira, A. Z. Khoury, and K. Dechoum. Quantum and classical separability of spin-orbit laser modes. Physical Review A, 90(5):053842, November 2014. 61

[53] L. Marrucci, C. Manzo, and D. Paparo. Optical spin-to-orbital angular momentum conversion in inhomogeneous anisotropic media. Physical Review Letters, 96(16):163905, April 2006. 61

[54] Jörg S. Eismann, Martin Neugebauer, and Peter Banzer. Exciting a chiral dipole moment in an achiral nanostructure. Optica, 5(8):954, August 2018. 61

[55] Kainã Diniz, Tanja Schoger, Arthur L. da Fonseca, Rafael S. Dutra, Diney S. Ether Jr, Gert-Ludwig Ingold, Felipe A. Pinheiro, Nathan B. Viana, and Paulo A. Maia Neto. Probing the chirality of a single microsphere trapped by a focused vortex beam through its orbital period. Nanophotonics, 14(2):209–217, 2025. 62, 63, 77, 109

[56] Cyriaque Genet. Chiral light–chiral matter interactions: an optical force perspective. ACS Photonics, 9(2):319–332, 2022. 63

[57] Ismo V. Lindell, editor. Electromagnetic waves in chiral and bi-isotropic media. The Artech House antenna library. Artech House, Boston [u.a.], 1994. Literaturangaben. 63

[58] Ari H. Sihvola and Ismo V. Lindell. Bi-isotropic constitutive relations. Microwave and Optical Technology Letters, 4(8):295–297, July 1991. 63

[59] Ivan Fernandez-Corbaton, Xavier Zambrana-Puyalto, and Gabriel Molina-Terriza. Helicity and angular momentum: A symmetry-based framework for the study of light-matter interactions. Physical Review A, 86(4):042103, October 2012. 63

[60] Ivan Fernandez-Corbaton, Xavier Zambrana-Puyalto, Nora Tischler, Xavier Vidal, Mathieu L. Juan, and Gabriel Molina-Terriza. Electromagnetic duality symmetry and helicity conservation for the macroscopic maxwell's equations. Physical Review Letters, 111(6):060401, August 2013. 63, 64

[61] X. Zambrana-Puyalto, I. Fernandez-Corbaton, M. L. Juan, X. Vidal, and G. Molina-Terriza. Duality symmetry and kerker conditions. Optics Letters, 38(11):1857, May 2013. 63

[62] Ivan Fernandez-Corbaton, Martin Fruhnert, and Carsten Rockstuhl. Objects of maximum electromagnetic chirality. Physical Review X, 6(3):031013, July 2016. 63

[63] L. D. Barron. Symmetry and molecular chirality. Chemical Society Reviews, 15(2):189, 1986. 64

[64] Yiqiao Tang and Adam E. Cohen. Optical chirality and its interaction with matter. Physical Review Letters, 104(16):163901, April 2010. 64

[65] Konstantin Y Bliokh, Aleksandr Y Bekshaev, and Franco Nori. Corrigendum: Dual electromagnetism: helicity, spin, momentum, and angular momentum (2013new j. phys.15033026). New Journal of Physics, 18(8):089503, August 2016. 64

[66] Jorge Olmos-Trigo, Manuel Nieto-Vesperinas, and Gabriel Molina-Terriza. Spheres of maximum electromagnetic chirality. Physical Review Research, 6(4):043192, November 2024. 64

[67] Andrew Zangwill. Modern Electrodynamics. Cambridge University Pr., 2013. 558-560. 64

[68] Onofrio Maragó Jones, Philip and Giovanni Volpe. Optical Tweezers. Cambridge University Press, Cambridge, 1st ed. edition, 2015. 64

[69] Antoine Canaguier-Durand and Cyriaque Genet. Chiral route to pulling optical forces and left-handed optical torques. Physical Review A, 92(4):043823, October 2015. 64, 65

[70] Gabriel Schnoering, Samuel Albert, Antoine Canaguier-Durand, and Cyriaque Genet. Chiral thermodynamics in tailored chiral optical environments. Physical Review X, 11(4):041022, November 2021. 65, 78

[71] Antoine Canaguier-Durand, James A Hutchison, Cyriaque Genet, and Thomas W Ebbesen. Mechanical separation of chiral dipoles by chiral light. New Journal of Physics, 15(12):123037, December 2013. 65

[72] Konstantin Y. Bliokh and Franco Nori. Characterizing optical chirality. Physical Review A, 83(2):021803, February 2011. 65

[73] Lisa Poulikakos, Jennifer Dionne, and Aitzol García-Etxarri. Optical helicity and optical chirality in free space and in the presence of matter. Symmetry, 11(9):1113, September 2019. 65

[74] Lisa V. Poulikakos, Philipp Gutsche, Kevin M. McPeak, Sven Burger, Jens Niegemann, Christian Hafner, and David J. Norris. Optical chirality flux as a useful far-field probe of chiral near fields. ACS Photonics, 3(9):1619–1625, August 2016. 67

[75] Gabriel Schnoering, Lisa V. Poulikakos, Yoseline Rosales-Cabara, Antoine Canaguier-Durand, David J. Norris, and Cyriaque Genet. Three-dimensional enantiomeric recognition of optically trapped single chiral nanoparticles. Physical Review Letters, 121(2):023902, July 2018. 67

[76] Adam Selyem, Carmelo Rosales-Guzmán, Sarah Croke, Andrew Forbes, and Sonja Franke-Arnold. Basis-independent tomography and nonseparability witnesses of pure complex vectorial light fields by stokes projections. Physical Review A, 100(6):063842, December 2019. 71

[77] C. E. R. Souza, J. A. O. Huguenin, P. Milman, and A. Z. Khoury. Topological phase for spin-orbit transformations on a laser beam. Physical Review Letters, 99(16):160401, October 2007. 71

[78] Rafael de Sousa Dutra. Efeitos de polarização nas pinças Óticas. Master's thesis, Universidade Federal do Rio de Janeiro, 2007. 77

[79] Rfaqat Ali, Felipe A. Pinheiro, Rafael S. Dutra, Felipe S. S. Rosa, and Paulo A. Maia Neto. Enantioselective manipulation of single chiral nanoparticles using optical tweezers. Nanoscale, 12(8):5031–5037, 2020. 77

[80] Rfaqat Ali, R. S. Dutra, F. A. Pinheiro, and P. A. Maia Neto. Enantioselection and chiral sorting of single microspheres using optical pulling forces. Optics Letters, 46(7):1640, March 2021. 77

[81] Kainã Gonçalves Diniz. Momento angular de spin em pinças Óticas. Master's thesis, Universidade Federal do Rio de Janeiro, 2018. 104

[82] Arthur Luna da Fonseca. Aplicando a Teoria Mie-Debye para Caracterização de Parâmetros Físicos em Pinças Óticas. Master's thesis, Universidade Federal do Rio de Janeiro, 2019. 105

[83] F. Zernike and F.J.M. Stratton. Diffraction theory of the knife-edge test and its improved form, the phase-contrast method. Mon. Not. R. Astron. Soc., 94(5):377–384, 03 1934. 108

Appendix A

Collaboration projects

This appendix explains some results of projects in which I participated as a co-author, but that have important relations to the main works presented in the thesis. The first project uses the MDSA+ theory for vortex beams (with astigmatism) to characterize experimental parameters of the optical system. The MDSA+ theory used in this project is presented in appendix B, and the method described in the respective publication is of great importance to show the viability of the employment of *ab-initio* theoretical models (like the MDSA+) in the characterization and description of physical systems.

The second project proposes a method to measure the chirality parameter of particles through the orbital period. The optical trap employs a circularly polarized $LG_{0\ell}$ mode, with a choice of ℓ that leads to orbital trapping. This project discusses the sensitivity of the method, as well as the particle size ranges in which it might be used to its full potential, providing a symbiotic discussion with the contents of Chapter 4.

A.1 Optical torque with VB OT

In this project, we developed a method to indirectly measure the radius of micron-sized dielectric spheres trapped in an OT setup employing VBs [38]. The method is based on the optical torque experiment, which was first introduced in the Master's thesis of Kainã Diniz [81] and is further detailed in the related publication [44]. The original torque experiment exploits the harmonic approximation of the optical force to produce a very stable and reproducible experiment. The main result contained in this work is the measurement of a negative optical torque, which is an unusual scattering phenomenon involving spin-orbit coupling of the trapping field and non-trivial exchange of angular momentum with the microsphere. This topic was also discussed in my Master's thesis [82], where I examined the viability of the characterization of experimental parameters, like the astigmatism of the beam, by fitting the data with the MDSA+ theory. Our starting point will be the earlier work, from where we proceed with a description of the employment of VB in this experiment and the benefits it brings.

The early optical torque experiment employed a fundamental Gaussian mode TEM_{00} with a controllable polarization state (starting with a x-polarized state and converting to a range of elliptical polarizations) on an oil-immersion objective. The trapped polystyrene microsphere was embedded in an aqueous medium with a Stokes drag coefficient β. The experimental procedure can be summarized as follows: the sphere height is set to a value that can be recovered in the numerical simulation (employing the MDSA theory) and proceeded to move the whole sample in the x direction using the PI nano-positioning stage (described in Fig. 3.1 of Sec. 3.1). By moving the sample with a constant velocity $\vec{v}_s$, the aqueous medium exerts a Stokes drag force $\vec{F}_S = \beta\vec{v}_s$, which displaces the microsphere from its axial equilibrium position.

In a general way, the torque angle α between the x-axis and the displaced microsphere equilibrium position will be $\alpha = \arctan(F_\phi/F_\rho)$ and will be non-zero if $F_\phi \neq 0$. As the optical force $\vec{F}$ is proportional to the power P that reaches the sample, we can quickly note that both F_ϕ/F_ρ and α do not depend on the laser power, effectively removing a possible source of error in the experiment.

Circular polarized beams are azimuthally symmetric, which means that the optical force will have no dependence on the azimuthal coordinate ϕ in this case. On the other hand, general elliptical polarized states and beams carrying azimuthally asymmetric aber-

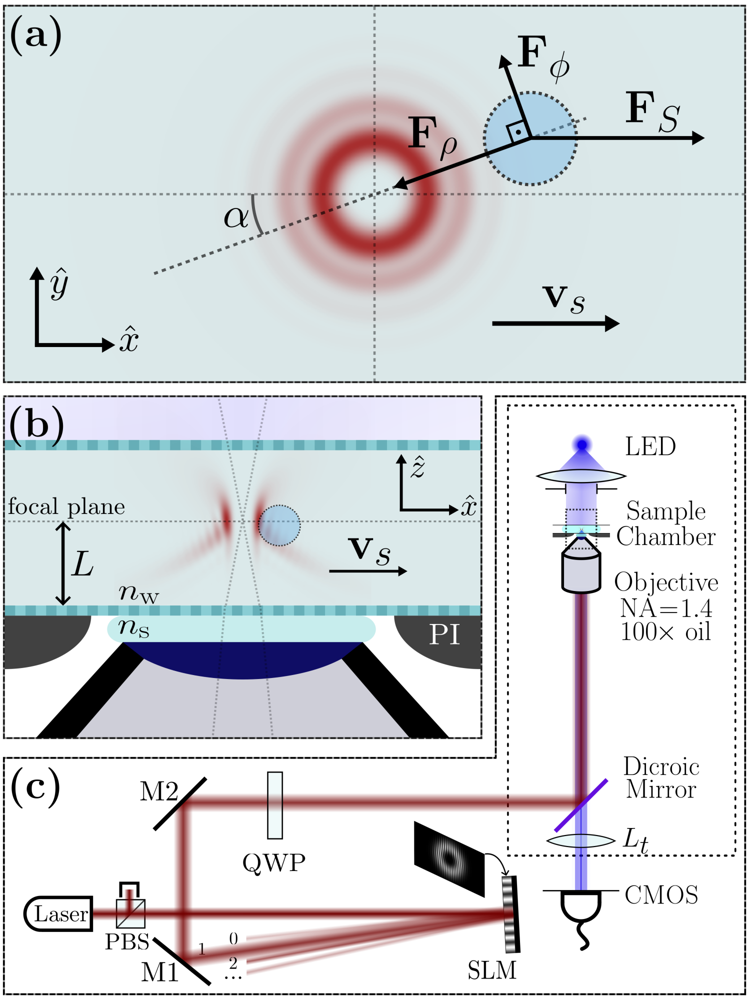

Figure A.1: Experimental setup for the torque experiment with VB OT. This image was extracted from reference [38].

rations, like astigmatism and coma, will break the above symmetry, which deeply affects the resulting non-paraxial tightly focused field. However, the optical force dependence with the ϕ coordinate can be made explicit for the case of elliptical polarizations (see eq.6 on ref. [44]).

The fact that a TEM_{00} mode was used in this earlier project caused the resulting torque angle α to be small (of up to $3° \approx 0.05\,\mathrm{rad}$) and the optical force to be harmonic within a relatively large range, allowing a few approximations to be made. The optical force will be approximated as $\vec{F} = -\kappa_\rho \rho + \kappa_\phi \rho$ (assuming equilibrium in the axial direction, *i.e.* $z = z_{\text{eq}}$), where κ_ρ is the transverse trap stiffness defined in eq. 2.37 and $\kappa_\phi = (\partial F_\phi / \partial \rho)|_{\rho=0}$ is the torsion constant. Therefore, the experiment can employ a few different velocities $\vec{v}_s$, each producing a different equilibrium position forming a line with angular coefficient α and centered at the axial equilibrium position. This angle can be easily evaluated numerically as $\alpha \approx \kappa_\phi/\kappa_\rho$ and compared to experimental data. The astigmatism of the trapping beam can be experimentally characterized and accounted for in the MDSA theory, yielding straightforward improvements in the data analysis and consequent interpretation.

In the present torque experiment, instead of using the polarization as a control parameter, we employed a range of Laguerre-Gaussian modes $\text{LG}_{0,\ell}$ with different values of ℓ and a fixed left circular polarized state $\sigma = 1$. Using the results described in Chapter 2, the range of ℓ values is chosen so we have only on-axis trapping scenarios, *i.e.* we chose values of ℓ for which the set of parameters is located above the blue line in the phase diagram depicted in Fig. 2.4.

When employing $\text{LG}_{0,\ell}$ modes on the torque experiment, we noted that the distance range for which the optical force can be considered linear is smaller than in the previous case. Additionally, astigmatism present in the trapping beams appears to play a big role in this system while also being more difficult to properly characterize, as many different beams with different ℓs are being used. On the other hand, the measured torque angles for each ℓ reach much higher values (up to tens of degrees), providing a much bigger signal-to-noise ratio.

While the first problem is easily fixed by employing smaller sample displacement velocities $\vec{v}_s$ or higher laser powers P, the issues brought by astigmatism have to be treated differently. In the earlier system, characterization of the astigmatism of the trapping beam was conducted (yielding the amplitude A_{ast} and principal meridian angle ϕ_{ast} of the phase aberration) and together with the experimental observation of overall small torque angles, allowed κ_ϕ and κ_ρ to be evaluated at $\phi = 0$ during the numerical analysis. Now, the torque angle α of each data point is evaluated by solving the following transcendental equation:

$$\alpha = \arctan\left(\frac{F_\phi(z_{\mathrm{eq}},\, \delta\rho,\, (\alpha - \phi_{\mathrm{ast}}),\, A_{\mathrm{ast}})}{F_\rho(z_{\mathrm{eq}},\, \delta\rho,\, (\alpha - \phi_{\mathrm{ast}}),\, A_{\mathrm{ast}})}\right), \tag{A.1}$$

where F_ϕ is the optical force expression, given by the MDSA+ theory, and $\delta\rho$ is a small radial displacement within the harmonic range. In order to account for the astigmatism aberration (introduced by the optical elements, including the objective lens and the laser fiber), we include an additional Zernike phase [83, 46] in the Richards-Wolf and Debye potentials formulation:

$$\Phi_{\mathrm{ast}}(\theta, \varphi) = 2\pi\, A_{\mathrm{ast}}\left(\frac{\sin\theta}{\sin\theta_0}\right)^2 \cos\Big(2(\varphi - \phi_{\mathrm{ast}})\Big)\,, \tag{A.2}$$

which is given in terms of the amplitude A_{ast} and the astigmatism axis angle ϕ_{ast}. The formulation of the Richards-Wolf model and MDSA+ theory for circularly polarized vortex beams carrying an astigmatism aberration phase is discussed in appendix B.4.

Finally, the resulting experimental data consists of α values as a function of topological charges ℓ for a single polystyrene microsphere. The microspheres used in the experiments had a nominal radius $a = \bar{a} \pm \sigma_a$ provided by the manufacturer, where $\bar{a}$ is the mean radius of the sample ensemble and σ_a is the uncertainty given by the corresponding standard deviation.

A.2 Chirality characterization through the orbital period on VB OTs

In Chapter 4, we discussed the application of OTs to the characterization of chiral particles, where we used the MDSA theory with modified Mie scattering coefficients for spheres made with a chiral medium. The case of hcVVBs accounts for an arbitrarily polarized incident beam, whereas a particular case is the one of a VB with a pure circular polarization state. In that scenario, we may drop all the cross-polarization terms and recover the MDSA theory presented in Chapter 2, but with the scattering coefficients for a chiral sphere.

In this project, we used the MDSA theory for circularly polarized VBs with different topological charges ℓ to characterize the chirality of a trapped spherical particle through its orbital period [55]. At first sight, the chirality of matter is sensitive only to the spin angular momentum (SAM) of light, given by the helicity of the field. More precisely, the coupling between the electromagnetic field and a chiral dipole depends solely on the circular polarization state of the incident light. However, recent studies have shown that higher-order interactions (beyond the dipole) allow the coupling of light's OAM with the chiral properties of matter. These interactions have been proposed as an alternative way to characterize the chirality of a sample through a technique analogous to circular dichroism but varying the OAM value instead.

In our case, the strong focusing process couples the spin and orbital angular momenta, causing the field intensity distribution to depend on the relative sign between σ and ℓ (see Sec. 2.1.3). A clear advantage of the method proposed in our work is that we can characterize individual particles in a non-invasive (or non-destructive) way and with very high precision, in contrast to conventional methods such as CD, which are limited to measuring the chiroptical properties of a particle ensemble.

The numerical calculations are done following similar procedures as described in 2.3, where we used a left circularly polarized VB with a fixed filling ratio ($r_\ell/R_p = 0.8$ for any VB with $\ell \neq 0$) respecting the overfilling criteria. According to Sec. 2.3.1, orbital trapping occurs when the sphere radius is smaller than the ring of maximum intensity of the tightly focused VB ($\tilde{r}_\ell > a$).

To calculate the orbital period, we begin by numerically evaluating the axial and radial force components (Q_z and Q_ρ) to determine the off-axis equilibrium point in the ρz plane, in the exact same way as in Sec. 3.3.2. The azimuthal force component will drive the particle along the orbital trajectory through the fluid, which exerts a drag force

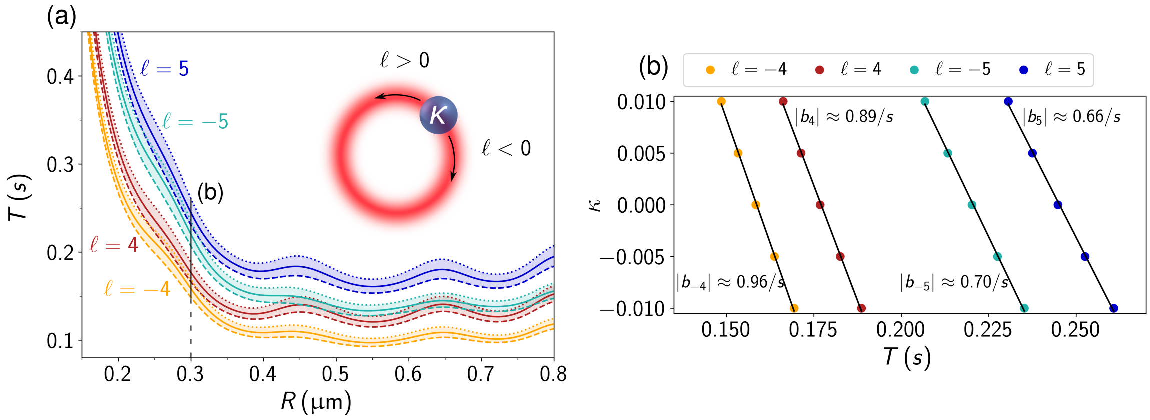

Figure A.2: Rotation period as a function of the radius R for various values of ℓ within a range of the chirality parameter κ. Panel (a) shows the dependence of T(s) with radius and illustrates the sense of rotation, given by the sign of ℓ. Panel (b) depicts the dependence of T(s) with κ, which defines the sensitivity of the method to characterize the particle's chirality.

proportional to the particle velocity [28, 29] as $\vec{F} = \beta\,\vec{v}$. In the overdamped regime of the Brownian motion, we expect that the Stokes drag force and the azimuthal component of the optical force cancel each other, leading to a relation between the velocity v_ϕ and the azimuthal efficiency factor $Q_\phi(\rho_{\rm eq}, z_{\rm eq})$, evaluated at the radial equilibrium position $\rho_{\rm eq}$ defining the circular orbital motion: $\rho_{\rm eq} = (v_\phi/\,\omega)$, where ω is the orbital angular frequency. The relation is also dependent on the axial equilibrium position $z_{\rm eq}$ and the laser power P arriving at the sample chamber:

$$v_\phi = \frac{n_1\,P}{c\,\beta} Q_\phi(\rho_{\rm eq}, z_{\rm eq})\,. \tag{A.3}$$

Finally, to obtain the period of rotation, we need to substitute the relation between the radial equilibrium position and the angular frequency $v_\phi = \rho_{\rm eq}\,\omega = \rho_{\rm eq}\frac{2\pi}{T}$:

$$T = \frac{2\pi\,\rho_{\rm eq}\,\beta}{(n_1 P/c)\;Q_\phi(\rho_{\rm eq}, z_{\rm eq})}\,. \tag{A.4}$$

In Fig. A.2(a), we show how the rotation period depends on the radius of the particle for a certain range of values of κ. In this panel, we also illustrate the sense of rotation of the particle, which depends only on the sign of the topological charge ℓ. Figure A.2(b) depicts how the rotation period depends on the chirality parameter κ, for a few different values of ℓ and a fixed radius value $R = 0.3\mu$m.

It is interesting to note how complementary this method is to the one discussed in Chapter 4. In this project, the highest sensitivity for the measurement of κ lies in the range of $0.15\mu\text{m} < R < 0.35\mu\text{m}$, whereas the method discussed in sec. 4.3 seems to be effective only when considering radii of up to $R \approx 0.2\mu$m (see Fig. 4.4). In conclusion, methods for characterizing experimental parameters (like the micro- or nano-sphere size and chirality parameter, for example) based on optical forces seem like promising rising tools. They present advantages over standard methods like CD (circular dichroism) and DLS (dynamic light scattering), which provide statistical measurements of particle ensembles, whereas the methods based on optical forces allow *in-situ* measurements of single and isolated particles.

Appendix B

Scattering theory in the Debye formalism and MDSA expressions for the optical force.

Throughout the thesis, I omitted some of the content to avoid diverging from the main focus of the discussions. This content includes some components of the efficiency factor and definitions of the multipole coefficients for a few different trapping system setups. In this appendix, I present all of these omitted expressions along with a supplementary discussion about the Debye potentials presented in sec. 2.2.1.

In sec. B.1, we present the discussion on the derivation of the Debye potentials for a left-circular polarized vortex beam. The following sections present the MDSA expressions and definitions for the respective multipole coefficients for three cases. Section B.2 presents the expressions for the same case as in sec. B.1, a left-circular polarized vortex beam. Section B.3 presents the optical force expressions for a tightly focused hybrid cylindrical Vector Vortex beam on a chiral sphere. Lastly, sec. B.4 presents the solution for the focal fields of vortex beams with astigmatism. We show the resulting expressions for the field and the optical force, which was used in the projects described in the previous appendix, in sec. A.1.

B.1 Debye potentials derivation

In this first section, we obtain the Debye potentials for a tightly focused Laguerre-Gaussian beam (following the Richards-Wolf formalism) by rotating and combining the Debye potentials of circularly polarized plane waves, given by eq. 2.27. The resulting Debye potentials will be given in terms of the pre-factors C^{E} and C^{M}, and the multipole expansion coefficient $\Gamma^{\sigma}_{jm\ell}$, following the definition in eqs. 2.28 and 2.29.

We begin by rotating each spherical wave component using the Wigner D-matrix $D^{j}_{m',m}(\alpha,\beta,\gamma)$, where α, β and γ are the Euler angles defining the rotation. The Wigner D-matrix acts only on the angular part of the partial waves, given by the spherical harmonics. Then, a rotated spherical harmonic $Y^{\sigma}_{j}(\theta',\phi')$ is represented as the sum:

$$Y^{m}_{j}(\theta',\phi') \;=\; \sum_{m'=-j}^{j} D^{j}_{m',m}(\alpha,\beta,\gamma) Y^{m'}_{j}(\theta,\phi) \tag{B.1}$$

Using the operator formalism, we can write the Wigner D-matrix $D^{j}_{m',m}(\alpha,\beta,\gamma)$ as:

$$\begin{aligned} D^{j}_{m',m}(\alpha,\beta,\gamma) \;&=\; \langle j,m'|\; e^{-i\alpha J_z}\, e^{-i\beta J_y}\, e^{-i\gamma J_z}\; |j,m\rangle \\ &=\; e^{-i(\alpha\, m'+\gamma\, m)}\; \langle j,m'|\; e^{-i\beta J_y}\; |j,m\rangle \;=\; e^{-i(\alpha\, m'+\gamma\, m)}\, d^{j}_{m',\,m}(\beta). \end{aligned} \tag{B.2}$$

Next, we define the Euler angles of the rotation: the angles $\alpha = \varphi_k$ and $\beta = \theta_k$ correspond to the incidence direction, as in $(\theta,\, \varphi)$ in eq. 2.6, while $\gamma = -\varphi_k$ is chosen as to conserve the helicity of the field, *i.e.* the polarization vector direction. The subscript k refers to the fact that $(\theta_k,\, \varphi_k)$ refers to spherical coordinates in the Fourier space, differing from the $(\theta,\, \phi)$ coordinates on the argument of the spherical harmonics defined in the position space.

Using eqs. B.2, B.1 and 2.27, we can obtain the Debye potentials of a rotated plane wave, which can then be used to construct a cone-shaped superposition of planes waves with half-aperture angle θ_k by integrating the rotated plane waves potentials in the φ_k coordinate. For now, we will only account for the helical phase of the input $\mathrm{LG}_{0\ell}$ mode, whereas the effect of the beam intensity profile will be introduced later. Using the relation between the coordinates $\phi = \varphi_k + \pi$ and the Abbe sine condition $\rho = f \sin\theta$, we obtain:

$$
\begin{aligned}
\Pi^{\mathrm{E}}_{\theta_k} \;&=\; \int_0^{2\pi} \mathrm{d}\varphi_k \, \sqrt{\cos\theta_k}\, e^{i\,\ell\phi} \sum_{j=1}^{\infty} \sum_{m'=-j}^{j} \; e^{-i(m'-\sigma)\varphi_k}\, d^{j}_{m',\sigma}(\theta_k)\, \left(\Pi^{\mathrm{E}}_{\mathrm{pw}}\right)_j \;= \\
&= \left(\frac{\sigma\, E_0\, e^{-i\omega t}}{\sqrt{2}\, k}\right) \sum_{j,\,m'} (i)^{j+1} \sqrt{\frac{4\pi\,(2j+1)}{j(j+1)}}\; j_j(kr)\, \sqrt{\cos\theta_k}(-1)^{\ell}\, d^{j}_{m',\sigma}(\theta_k)\, Y^{\sigma}_{j}(\theta,\phi) \,\times \\
&\times \left(\int_0^{2\pi} \mathrm{d}\varphi_k \, e^{-i(m'-\ell-\sigma)\varphi_k} \right) ,
\end{aligned}
\tag{B.3}
$$

where we used the compact notation for the sum.

In order to describe the relative position between the incident field focus and the sphere center, we should define the origin of the coordinate system. The first option is to describe the scattering of a displaced sphere, which breaks the symmetries that were responsible for making the spherical waves the eigenstate basis of our problem. Therefore, translating the incident field is a much simpler and easier solution to describe the relative displacement between the sphere and the beam focus. We do it by applying the translation operator $e^{-i\mathbf{k}\cdot\mathbf{q}}$ to displace the position of the total field by the vector $\mathbf{q}$. According to the system symmetry, the displacement vector is best expressed in cylindrical coordinates: $\mathbf{q} = (z_q\hat{z} + \rho_q\hat{\rho} + \phi_q\hat{\phi})$, transforming eq. B.3 as:

$$
\begin{aligned}
\Pi^{\mathrm{E}}_{\mathrm{IN}} \;&=\; \int_0^{\theta_0} \sin\theta_k \, \mathrm{d}\theta_k \; \Pi^{\mathrm{E}}_{\theta_k} \;=\; \left(\frac{\sigma\, E_0\, e^{-i\omega t}}{\sqrt{2}\, k}\right) \sum_{j,\,m} \Bigg[(i)^{j+1} \sqrt{\frac{4\pi\,(2j+1)}{j(j+1)}} \int_0^{\theta_0} \sin\theta_k \, \mathrm{d}\theta_k \\
&j_j(kr)\, \sqrt{\cos\theta_k}\, (-1)^{\ell}\, d^{j}_{m,\sigma}(\theta_k)\, Y^{\sigma}_{j}(\theta,\phi) \left(\int_0^{2\pi} \mathrm{d}\varphi_k \; e^{-i\mathbf{k}\cdot\mathbf{q}}\; e^{-i(m-\ell-\sigma)\varphi_k} \right) \Bigg] ,
\end{aligned}
\tag{B.4}
$$

and we can identify the integral between parenthesis as λ_M with $M = m - \ell$, defined as:

$$
\begin{aligned}
\lambda_M \;&=\; \int_0^{2\pi} \mathrm{d}\varphi_k \; e^{-i\mathbf{k}\cdot\mathbf{q}}\; e^{-i(M-\sigma)\varphi_k} \;= \\
&= \left[e^{-i\,k\,z_q\,\cos\theta_k}\, 2\pi\,(-i)^{M-\sigma}\, J_{M-\sigma}(k\rho_q \sin\theta_k)\, e^{-i(M-\sigma)\phi_q} \right]
\end{aligned}
\tag{B.5}
$$

where $J_{M-\sigma}(x)$ is the cylindrical Bessel function of the first kind.

Finally, the last step to obtain the Debye potential for the incident tightly focused field is to weight each plane wave in eq. 2.24 by the input $\mathrm{LG}_{0\ell}$ mode field amplitude, given in eq. 2.1. Using the Abbe sine condition and the definition of $\gamma = f/w_0$, we can express the paraxial field amplitude given in eq. 2.1 as a function of θ_k, and insert it into eq. B.4, yielding:

$$\Pi^{\mathrm{E}}_{\mathrm{IN}} = \left(\frac{\sigma\, E_0\, e^{-i\omega t}}{\sqrt{2}\, k}\right)\left(\frac{f}{\lambda}\right)(\sqrt{2}\,\gamma)^{|\ell|}\,(-1)^{|\ell|}\sum_{j,\,m}\Bigg[\Big(j_j(kr)\,Y^{\sigma}_j(\theta,\phi)\Big)\times$$
$$\sqrt{\frac{4\pi\,(2j+1)}{j(j+1)}}\,(i)^j\,\Big(2\pi\,(-i)^{m-\ell-\sigma}\;e^{-i(m-\ell-\sigma)\phi_q}\Big)\times$$
$$\int_0^{\theta_0}\mathrm{d}\theta_k\,(\sin\theta_k)^{|\ell|+1}\,\sqrt{\cos\theta_k}\,e^{-ikz_q\cos\theta_k}\,e^{-\gamma^2\sin^2\theta_k}\,d^{j}_{m,\,\sigma}(\theta_k)\,J_{(m-\ell-\sigma)}(k\rho\sin\theta_k)\Bigg], \quad \text{(B.6)}$$

which yield the following values for the coefficients $\Gamma^{\sigma}_{jm\ell}$ and C^{E}:

$$\Gamma^{\sigma}_{jm\ell} = \sqrt{\frac{4\pi\,(2j+1)}{j(j+1)}}\,(i)^j\,\Big(2\pi\,(-i)^{m-\ell-\sigma}\;e^{-i(m-\ell-\sigma)\phi_q}\Big)\times$$
$$\left[\int_0^{\theta_0}\mathrm{d}\theta_k\,(\sin\theta_k)^{|\ell|+1}\,\sqrt{\cos\theta_k}\,e^{-ikz_q\cos\theta_k}\,e^{-\gamma^2\sin^2\theta_k}\,d^{j}_{m,\,\sigma}(\theta_k)\,J_{(m-\ell-\sigma)}(k\rho\sin\theta_k)\right], \quad \text{(B.7)}$$

$$C^{\mathrm{E}} = \left(\frac{E_0\, e^{-i\omega t}}{\sqrt{2}\, k}\right)\left(\frac{f}{\lambda}\right)(\sqrt{2}\,\gamma)^{|\ell|}\,(-1)^{|\ell|} = \left(\frac{E_0\,\sqrt{2}\,\pi\,f\,e^{-i\omega t}}{k^2}\right)(-\sqrt{2}\,\gamma)^{|\ell|}\,. \quad \text{(B.8)}$$

From eq. B.8 and the relation $H_0 = E_0\,(n_i/\mu_0 c)$, we can also obtain the value of C^{M}:

$$C^{\mathrm{M}} = \frac{-i\,n_i}{\mu_0\,c}\,C^{\mathrm{E}} = \left(\frac{-i\,H_0\,\sqrt{2}\,\pi\,f\,e^{-i\omega t}}{k^2}\right)(-\sqrt{2}\,\gamma)^{|\ell|}\,. \quad \text{(B.9)}$$

B.2 MDSA expressions and multipole coefficients for a circularly polarized vortex beam

In this section, we present the expressions for the axial ($\sim \hat{z}$) and azimuthal ($\sim \hat{\phi}$) components of the efficiency factor, divided into extinction and scattering terms. The expressions below are for an optical trap employing a left-circular polarized ($\sigma = 1$) vortex beam with topological charge ℓ, which corresponds to the systems discussed in chapters 2 and 3.

We begin with the extinction component of the optical force. The axial extinction force component is:

$$Q_{ez} = \frac{2(2\gamma^2)^{|\ell|+1}}{|\ell|!\, A_\ell\, N_a} \operatorname{Re} \sum_{j=1}^{\infty} \sum_{m=-j}^{j} \Big[(2j+1)(a_j + b_j) \big(G_{j,m}\, G'^{*}_{j,m} \big) \Big] , \tag{B.10}$$

while the azimuthal (extinction) component is:

$$Q_{e\phi} = \frac{-(2\gamma^2)^{|\ell|+1}}{|\ell|!\, A_\ell\, N_a} \operatorname{Re} \sum_{j=1}^{\infty} \sum_{m=-j}^{j} \Big[(2j+1)(a_j + b_j) G_{j,m} \left(G^{(-)}_{j,m+1} + G^{(+)}_{j,m-1} \right)^* \Big] . \tag{B.11}$$

Next, the scattering component of the optical force in the axial direction is:

$$Q_{sz} = \frac{-4(2\gamma^2)^{|\ell|+1}}{|\ell|!\, A_\ell\, N_a} \sum_{jm} \operatorname{Re} \Bigg[\frac{\sqrt{j(j+2)(j-m+1)(j+m+1)}}{(j+1)} \Big((a_j a^*_{j+1} + b_j b^*_{j+1}) \big(G_{j,m} G^*_{j+1,m} \big) \Big) + m\sigma \, \frac{(2j+1)}{j(j+1)} \Big((a_j b^*_j) \big(G_{j,m} G^*_{j,m} \big) \Big) \Bigg], \tag{B.12}$$

while the azimuthal (scattering) component is:

$$Q_{s\phi} = \frac{-2(2\gamma^2)^{|\ell|+1}}{|\ell|!\, A_\ell\, N_a} \sum_{jm} \Bigg[\frac{\sqrt{j(j+2)(j+m+1)(j+m+2)}}{(j+1)} \operatorname{Re}\Big((a_j a^*_{j+1} + b_j b^*_{j+1}) \big(G_{j,m} G^*_{j+1,m+1} - - G_{j,-m} G^*_{j+1,-m-1} \big) \Big) - 2\sigma \, \frac{(2j+1)}{j(j+1)} \sqrt{(j-m)(j+m+1)} \operatorname{Re}(a_j b^*_j) \operatorname{Re}\left(G_{j,m} G^*_{j,m+1} \right) \Bigg]. \tag{B.13}$$

Finally, the expression for the multipole coefficients $G'_{j,m}$ and $G^{(\pm)}_{j,m}$ are:

$$G'_{jm} = \int_0^{\theta_0} d\theta (\sin\theta)^{|\ell|+1} \sqrt{\cos\theta}\, \cos\theta_1\, T(\theta) \times d^j_{m,\sigma}(\theta_1) J_{m-\sigma-\ell}(k_1 \rho \sin\theta_1) e^{i(\Phi(\theta) + k_1 \cos\theta_1 z) - \gamma^2 \sin^2\theta} , \tag{B.14}$$

and

$$G^{\pm}_{jm} = \int_0^{\theta_0} d\theta (\sin\theta)^{|\ell|+1} \sqrt{\cos\theta}\, \sin\theta_1\, T(\theta) \times d^j_{m\pm1,\sigma}(\theta_1) J_{m-\sigma-\ell}(k_1 \rho \sin\theta_1) e^{i(\Phi(\theta) + k_1 \cos\theta_1 z) - \gamma^2 \sin^2\theta} . \tag{B.15}$$

B.3 MDSA expressions for systems employing hcVVBs and chiral spheres

In this section, we present the expressions for the axial ($\sim \hat{z}$) and azimuthal ($\sim \hat{\phi}$) components of the optical force exerted on a chiral sphere by a tightly focused hybrid cylindrical Vector Vortex Beam. The terms are divided into extinction and scattering terms, each containing direct- ($\sim (\psi_\sigma^2)$) and cross-polarization ($\sim (\Psi^{(\sigma)})$) contributions. The expressions below are valid for an optical trapping system employing the hcVVB modes and chiral microspheres discussed in chapter 4. We assume that the topological charge index ℓ on the expressions below corresponds to the topological charge value of the right-circular ($\sigma = -1$) polarized state component, following the convention explained in sec. 4.2.1.

We begin by presenting the extinction component $\mathbf{Q}_e$ of the efficiency factor. The axial extinction force component is:

$$Q_{ez}^{(\ell)}(\rho, \phi, z) = \frac{2(2\gamma^2)^{|\ell|+1}}{|\ell|!\, A_\ell N_a} \sum_{jm\sigma} (2j+1)\, \mathrm{Re}\Big\{ \Big(G_{j,m}^{(\sigma,\ell)} \Big) \times$$
$$\times \Big[\big(a_j^{(\sigma)} + b_j^{(\sigma)}\big) \big[G_{j,m}'^{(\sigma,\ell)}\big]^* \big(\psi_\sigma^2\big) + \big(a_j^{(\sigma)} - b_j^{(\sigma)}\big) \big[G_{j,m}'^{(-\sigma,\ell)}\big]^* \big(\Psi^{(\sigma)}\big) \Big] \Big\}, \tag{B.16}$$

while the azimuthal (extinction) component is:

$$Q_{e\phi}^{(\ell)}(\rho, \phi, z) = \frac{-(2\gamma^2)^{|\ell|+1}}{|\ell|!\, A_\ell N_a} \sum_{jm\sigma} (2j+1)\, \mathrm{Re}\Big\{ \Big(G_{j,m}^{(\sigma,\ell)} \Big) \times$$
$$\times \Big[\big(a_j^{(\sigma)} + b_j^{(\sigma)}\big) \big[G_{j,m+1}^{(-)(\sigma,\ell)} + G_{j,m-1}^{(+)(\sigma,\ell)}\big]^* \big(\psi_\sigma^2\big) + \big(a_j^{(\sigma)} - b_j^{(\sigma)}\big) \big[G_{j,m+1}^{(-)(-\sigma,\ell)} + G_{j,m-1}^{(+)(-\sigma,\ell)}\big]^* \big(\Psi^{(\sigma)}\big) \Big] \Big\}. \tag{B.17}$$

The axial scattering component of the optical force is:

$$Q_{sz}^{(\ell)}(\rho, \phi, z) = \frac{-4(2\gamma^2)^{|\ell|+1}}{|\ell|!\, A_\ell N_a} \sum_{jm\sigma} \mathrm{Re}\Big\{ \Big[\frac{\sqrt{j(j+2)(j+m+1)(j-m+1)}}{j+1} \times$$
$$\times \Big(\big(a_j^{(\sigma)} a_{j+1}^{(\sigma)*} + b_j^{(\sigma)} b_{j+1}^{(\sigma)*}\big) \Big[G_{j,m}^{(\sigma,\ell)} G_{j+1,m}^{(\sigma,\ell)*} \Big] \big(\psi_\sigma^2\big) + \big(a_j^{(\sigma)} a_{j+1}^{(-\sigma)*} - b_j^{(\sigma)} b_{j+1}^{(-\sigma)*}\big) \Big[G_{j,m}^{(\sigma,\ell)} G_{j+1,m}^{(-\sigma,\ell)*} \Big] \big(\Psi^{(\sigma)}\big) \Big) \Big] +$$
$$+ \Big[m\sigma \frac{(2j+1)}{j(j+1)} \Big(\big(a_j^{(\sigma)} b_j^{(\sigma)*}\big) \Big[G_{j,m}^{(\sigma,\ell)} G_{j,m}^{(\sigma,\ell)*} \Big] \big(\psi_\sigma^2\big) - \big(a_j^{(\sigma)} b_j^{(-\sigma)*}\big) \Big[G_{j,m}^{(\sigma,\ell)} G_{j,m}^{(-\sigma,\ell)*} \Big] \big(\Psi^{(\sigma)}\big) \Big) \Big] \Big\}, \tag{B.18}$$

while the azimuthal (scattering) component is:

$$
\begin{aligned}
Q_{s\phi}^{(\ell)}(\rho,\phi,z) = & \frac{-2(2\gamma^2)^{|\ell|+1}}{|\ell|!\,A_\ell N_a}\sum_{jm\sigma}\Bigg\{\Bigg[\frac{\sqrt{j(j+2)(j+m+1)(j+m+2)}}{j+1}\times \\
& \times\mathrm{Re}\Big(\big(a_j^{(\sigma)}a_{j+1}^{(\sigma)*}+b_j^{(\sigma)}b_{j+1}^{(\sigma)*}\big)\big[G_{j,m}^{(\sigma,\ell)}G_{j+1,m+1}^{(\sigma,\ell)*}-G_{j,-m}^{(\sigma,\ell)}G_{j+1,-(m+1)}^{(\sigma,\ell)*}\big]\big(\psi_\sigma^2\big)+ \\
& +\big(a_j^{(\sigma)}a_{j+1}^{(-\sigma)*}-b_j^{(\sigma)}b_{j+1}^{(-\sigma)*}\big)\big[G_{j,m}^{(\sigma,\ell)}G_{j+1,m+1}^{(-\sigma,\ell)*}-G_{j,-m}^{(\sigma,\ell)}G_{j+1,-(m+1)}^{(-\sigma,\ell)*}\big]\big(\Psi^{(\sigma)}\big)\Big)\Bigg]- \\
& -\Bigg[\sigma\,\frac{(2j+1)}{j(j+1)}\sqrt{(j-m)(j+m+1)}\times\Big(2\,\mathrm{Re}\big(a_j^{(\sigma)}b_j^{(\sigma)*}\big)\,\mathrm{Re}\big[G_{j,m}^{(\sigma,\ell)}G_{j,m+1}^{(\sigma,\ell)*}\big]\big(\psi_\sigma^2\big)- \\
& -\mathrm{Re}\Big[\big(a_j^{(\sigma)}b_j^{(-\sigma)*}\big)\big(G_{j,m}^{(\sigma,\ell)}G_{j,m+1}^{(-\sigma,\ell)*}+G_{j,m+1}^{(\sigma,\ell)}G_{j,m}^{(-\sigma,\ell)*}\big)\big(\Psi^{(\sigma)}\big)\Big]\Big)\Bigg]\Bigg\}\,. \qquad \text{(B.19)}
\end{aligned}
$$

As we used the convention of using the value of ℓ relative to the $\sigma = -1$ component as the index of the expressions above (see sec. 4.2.2), we redefined the multipole coefficients $G_{j,m}^{(\sigma,\ell)}$, $G_{j,m}^{\prime\,(\sigma,\ell)}$ and $G_{j,m}^{(\pm)(\sigma,\ell)}$. The first coefficient $G_{j,m}^{(\sigma,\ell)}$ is defined in eq. B.21, while $G_{j,m}^{\prime\,(\sigma,\ell)}$ is defined as:

$$
\begin{aligned}
G_{j,m}^{\prime\,(\sigma,\ell)} = & \int_0^{\theta_0} d\theta\,(\sin\theta)^{1+|\ell|}\sqrt{\cos\theta}\,\cos\theta_1\,T(\theta)\times \\
& e^{-\gamma^2\sin^2\theta}e^{i\Phi(\theta,z)}\,d_{m,\sigma}^{j}(\theta_1)\,J_{m+\sigma(\ell-1)}(k_1\rho\sin\theta_1), \qquad \text{(B.20)}
\end{aligned}
$$

and $G_{j,m}^{(\pm)(\sigma,\ell)}$ is defined as:

$$
\begin{aligned}
G_{j,m}^{(\pm)(\sigma,\ell)} = & \int_0^{\theta_0} d\theta\,(\sin\theta)^{1+|\ell|}\sqrt{\cos\theta}\,\sin\theta_1\,T(\theta)\times \\
& e^{-\gamma^2\sin^2\theta}e^{i\Phi(\theta,z)}\,d_{m\pm1,\sigma}^{j}(\theta_1)J_{m+\sigma(\ell-1)}(k_1\rho\sin\theta_1). \qquad \text{(B.21)}
\end{aligned}
$$

Also, the phase $\Phi(\theta,z)$ above is the sum of the spherical aberration phase and the phase corresponding to a space translation in the z direction, resulting in the following expression:

$$
\Phi(\theta,z) = kL\left(-\frac{\cos\theta}{N_a}+N_a\,\cos\theta_1\right)+k\cos\theta_1 z\,. \qquad \text{(B.22)}
$$

Finally, it is worth mentioning that the definition of the filling fraction does not depend on the polarization state and remains the same for values of ℓ with the same absolute value. Therefore, as long as the topological charge relative to each polarization component of the incident beam has the same absolute value $|\ell|$, the filling fraction is given by eq. 2.22. The expression reads:

$$A_\ell = \frac{8(2\gamma^2)^{|\ell|+1}}{|\ell|!} \int_0^{\sin\theta_0} ds\, s^{2|\ell|+1} \exp\left(-2\gamma^2 s^2\right) \frac{\sqrt{(1-s^2)(N_a^2 - s^2)}}{(\sqrt{1-s^2} + \sqrt{N_a^2 - s^2})^2}.$$

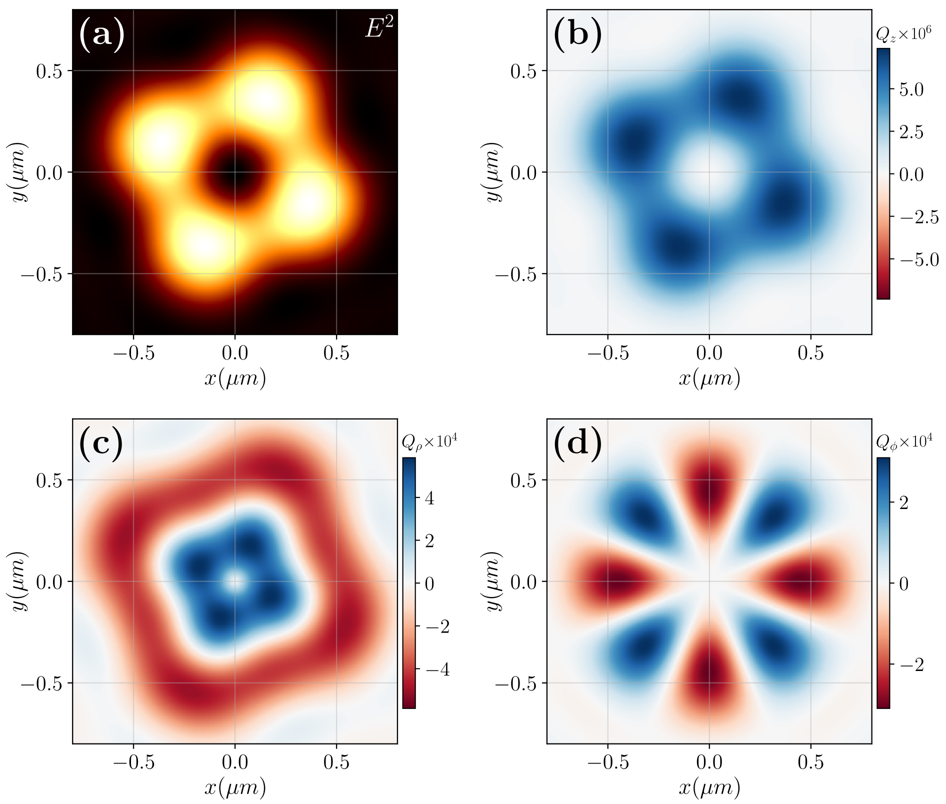

Figure B.1: Density plots of the intensity distribution (panel (a)) and resulting force field (panels (b)-(d)) exerted by a tightly focused Hybrid cylindrical Vector Vortex beam with $\ell = -1$ on a microsphere with radius $a = 0.05\mu$m. The force field is represented in cylindrical coordinates, where panel (b) shows the axial component (Q_z), panel (c) shows the radial component (Q_ρ), and panel (d) shows the azimuthal component (Q_ϕ). In panels (b)-(d), the color blue (red) represents a positive (negative) force sign, which points outwards (inwards) the image plane in panel (b), while in panel (c) it points away from (towards) the origin, and in panel (d) it points in the counter-clockwise (clockwise) direction.

In Fig. B.1 we show the numerical evaluation of the electric field intensity distribution (panel (a)), and the optical force components in cylindrical coordinates (panels (b)-(d)). We consider a microsphere in the dipole regime, with radius $a = 0.05\mu$m, and an input hcVVB with topological charge $\ell = -1$ (associated with the $\sigma = -1$ vortex beam component). We illustrate the symmetry break due to the cross-polarization component, which is seen in both the intensity distribution and the optical force, and happens for every topological charge value $\ell \neq 1$.

B.4 MDSA expressions for vortex beams with astigmatism aberration

The effect of the primary astigmatism aberration can be introduced into the Richards-Wolf model (and therefore into the MDSA model as well) by multiplying each plane-wave component by the astigmatism phase, given in eq. A.2. Note that, unlike the spherical aberration phase (for example), the astigmatism phase has a dependency on the azimuthal angle ϕ. This dependency is responsible for breaking the rotational symmetry of the previous expressions for the optical force and electric intensity distribution of tightly focused pure circularly polarized vortex beams.

Additionally, since the rotational symmetry order of primary astigmatism coincides with the one of first order Hermite-Gaussian modes (HG_{01} and HG_{10}), one can directly employ the techniques and procedures presented in this section to extend the Richards-Wolf and MDSA models for such beam modes. Furthermore, this approach can be extended to describe higher-order geometrical phase aberrations (given by Zernike polynomials $Z_l^n(\rho, \phi)$ with azimuthal order $|l| \geq 2$, see ref. [18] for more details) and higher-order transverse modes (*e.g.*, arbitrary order Hermite-Gaussian modes HG_{nm} or combinations of Laguerre-Gaussian modes $LG_{p\ell}$ with different p and ℓ values) at the cost of increased analytical and computational complexity.

The main difference in the calculations of the Richards-Wolf and MDSA models caused by the presence of any aberration phase that depends on the azimuthal angle ϕ is in the azimuthal integrals, namely eq. 2.11 (related to the focal field intensity) and eq. B.5 (related to the optical force). We begin to address the changes by solving the azimuthal integral of the focal field (eq. 2.10), which will yield a different expression for the function $I_m^{(\ell)}$ in eq. 2.12. Then, we redefine the function λ_M used in the derivation of the MDSA model and present the resulting multipole coefficients $G_{j,m}$, $G'_{j,m}$, and $G^{(\pm)}_{j,m}$.

The method to solve the integrals in eqs. 2.10 and B.5 are similar, and both are based on the generating function of the Bessel functions of the first kind [20]:

$$e^{\frac{z}{2}\left(t-\frac{1}{t}\right)} \;=\; \sum_{n=-\infty}^{\infty} t^n\, J_n(z)\,, \tag{B.23}$$

and on the integral definition of the Kronecker delta function as:

$$\int_0^{2\pi} e^{i\,(n-m)\,\varphi} d\varphi \;=\; 2\pi\,\delta_{n,m}\,. \tag{B.24}$$

The first step in our calculation is to expand the additional astigmatism phase term in the azimuthal integral as a sum of Bessel functions. The phase term can be written as:

$$\begin{aligned}
e^{i\,\Phi_{\text{ast}}(\theta,\varphi)} \;&=\; \exp\left[i\;\underbrace{2\pi\,A_{\text{ast}}\left(\frac{\sin\theta}{\sin\theta_0}\right)^2}_{=\mathcal{A}_{\text{ast}}}\cos\Big(2(\varphi-\phi_{\text{ast}})\Big)\right] \;=\\
&=\; \exp\left[\mathcal{A}_{\text{ast}}\,\frac{i}{2}\Big(e^{-i\,2(\varphi-\phi_{\text{ast}})}+e^{i\,2(\varphi-\phi_{\text{ast}})}\Big)\right] \;=\\
&=\; \exp\left[\frac{\mathcal{A}_{\text{ast}}}{2}\left(i\,e^{-i\,2(\varphi-\phi_{\text{ast}})}-\frac{1}{i\,e^{-i\,2(\varphi-\phi_{\text{ast}})}}\right)\right] \;=\\
&=\; \exp\left[\frac{\mathcal{A}_{\text{ast}}}{2}\left(i\,e^{i\,2(\varphi-\phi_{\text{ast}})}-\frac{1}{i\,e^{i\,2(\varphi-\phi_{\text{ast}})}}\right)\right].
\end{aligned} \tag{B.25}$$

Identifying $\mathcal{A}_{\text{ast}} = 2\pi\,A_{\text{ast}}\left(\frac{\sin\theta}{\sin\theta_0}\right)^2$ as (z) and $(i\,e^{\pm i\,2(\varphi-\phi_{\text{ast}})})$ as (t) in eq. B.23, we can expand eq. B.25 as:

$$e^{i\,\Phi_{\text{ast}}} \;=\; \sum_{p=-\infty}^{\infty}(i)^p\,e^{-i\,2p(\varphi-\phi_{\text{ast}})}J_p(\mathcal{A}_{\text{ast}}) \;=\; \sum_{p=-\infty}^{\infty}(i)^p\,e^{i\,2p(\varphi-\phi_{\text{ast}})}J_p(\mathcal{A}_{\text{ast}})\,. \tag{B.26}$$

Now, the azimuthal integral for the field in eq. 2.10, including the astigmatism phase term, will take the following form (indexed by $M = \{\ell + 2\sigma,\, \ell + \sigma,\, \ell\}$ as in eq. 2.11):

$$
\begin{aligned}
&\int_0^{2\pi} d\varphi\, e^{iM\varphi}\, e^{i\xi\cos(\varphi-\phi)}\, e^{i\,\Phi_{\text{ast}}(\theta,\phi)} = \\
&= \sum_{n=-\infty}^{\infty} (i)^n\, e^{i\,n\phi}\, J_n(\xi) \sum_{p=-\infty}^{\infty} (i)^p\, e^{i\,2p\,\phi_{\text{ast}}}\, J_p(\mathcal{A}_{\text{ast}}) \underbrace{\int_0^{2\pi} d\varphi\, e^{iM\varphi} e^{-in\varphi}\, e^{-i\,2p\,\varphi}}_{=2\pi\,\delta_{n,\,M-2p}} = \\
&= (2\pi)\,(i)^M\, e^{i\,M\phi} \sum_{p=-\infty}^{\infty} (-i)^p\, e^{-i\,2p\,(\phi-\phi_{\text{ast}})}\, J_{M-2p}(\xi)\, J_p(\mathcal{A}_{\text{ast}})\,, \qquad \text{(B.27)}
\end{aligned}
$$

where we used eq. B.23 to expand the term $e^{i\xi\cos(\varphi-\phi)}$, with $\xi = (k_1\,\rho\,\sin\theta_1)$. Now, it is helpful to rearrange the sum in eq. B.27 so that we can analyze the convergence of the series. We isolate the term $p = 0$ and, using the property of the Bessel functions $J_{-n}(z) = (-1)^n J_n(z)$, we write the remaining terms as a sum from $p = 1$ to $p = +\infty$ and define the function $\mathcal{V}_M(\rho,\,\phi\,;\,\theta)$:

$$
\begin{aligned}
\mathcal{V}_M(\rho,\,\phi\,;\,\theta) \;&=\; \sum_{p=-\infty}^{\infty} (-i)^p\, e^{-i\,2p\,(\phi-\phi_{\text{ast}})}\, J_{M-2p}(\xi)\, J_p(\mathcal{A}_{\text{ast}}) \;= \qquad \text{(B.28)} \\
J_M(\xi)\; J_0(\mathcal{A}_{\text{ast}}) &+ \sum_{p=1}^{\infty} J_p(\mathcal{A}_{\text{ast}})\,(-i)^p \Big[e^{-i\,2p\,(\phi-\phi_{\text{ast}})}\, J_{M-2p}(\xi) \;+\; e^{i\,2p\,(\phi-\phi_{\text{ast}})}\, J_{M+2p}(\xi) \Big]\,.
\end{aligned}
$$

Note that when the astigmatism parameter is zero, *i.e.* $A_{\text{ast}} = 0$ (or $\mathcal{A}_{\text{ast}} = 0$ for any θ), the only non-zero term in the expression above is $J_0(\mathcal{A}_{\text{ast}}) = 1$ because $J_p(0) = 0$ for any $p \neq 0$. Therefore, if the optical system is astigmatism-free, the astigmatism parameter A_{ast} is null, and eq. B.27 takes the same form as eq. 2.11.

Finally, we can substitute eq. B.28 into eq. 2.6 (using eq. 2.8) to obtain the modified $I_m^{(\ell)}(\mathbf{r})$ function:

$$
\begin{aligned}
I_m^{(\ell)}(\rho,\phi,z) =\; (\sqrt{2}\,\gamma)^{|\ell|} &\int_0^{\theta_0} d\theta\,(\sin\theta)^{1+|\ell|}\sqrt{\cos\theta}\, e^{-\gamma^2\sin^2\theta}\, T(\theta)\, e^{i\Phi(\theta)} \\
&\times f_{|m|}(\theta)\, e^{i\,k_1 z\cos\theta_1}\, \mathcal{V}_{\ell+m}(\rho,\,\phi\,;\,\theta)\,. \qquad \text{(B.29)}
\end{aligned}
$$

In accordance with the symmetry break associated with the astigmatism aberration, this modified $I_m^{(\ell)}(\mathbf{r})$ function exhibits an additional dependence on the coordinate ϕ which is propagated to the expressions for the electric field intensity (eq. 2.15) and chirality density distribution (eq. 4.26).

In order to account for astigmatism in the MDSA force model, we must redefine the azimuth angle integral in eq. B.5. Thus, the integral with the astigmatism phase becomes:

$$\begin{aligned} \lambda_M(\theta_k) \;&=\; \int_0^{2\pi} \mathrm{d}\varphi_k \; e^{-i\mathbf{k}\cdot\mathbf{q}} \; e^{-i(M-\sigma)\varphi_k} \; e^{i\,\Phi_{\mathrm{ast}}(\theta_k,\,\varphi_k)} \;= \\ &=\; \Big[\, e^{-i\,k\,z_q\,\cos\theta_k}\, 2\pi\,(-i)^{M-\sigma}\, e^{-i(M-\sigma)\phi_q} \,\times \\ &\times \sum_{p=-\infty}^{\infty} (-i)^p \; e^{i\,2p\,(\phi_{\mathrm{ast}}-\phi_q)} \; J_{2p+M}(k_1\rho\sin\theta_1)\; J_p(\mathcal{A}_{\mathrm{ast}}) \,\Big]\,. \end{aligned} \tag{B.30}$$

This new integral only changes the definitions of the multipole coefficients (eqs. 2.36, B.14, and B.15), while leaving the expressions for the optical force (eqs. 2.34, 2.35, B.10, B.11, B.12, and B.13) unchanged (as a function of the new multipole coefficients). The new coefficients are:

$$\begin{aligned} G_{jm} = &\int_0^{\theta_0} d\theta(\sin\theta)^{|\ell|+1}\sqrt{\cos\theta}\; T(\theta)\; d^{j}_{m,\sigma}(\theta_1) e^{i(\Phi(\theta)\,+\,k_1\cos\theta_1 z)\,-\,\gamma^2\sin^2\theta} \times \\ &\mathcal{W}_{m-\sigma-\ell}(\rho,\,\phi\,;\,\theta)\,, \end{aligned} \tag{B.31}$$

$$\begin{aligned} G'_{jm} = &\int_0^{\theta_0} d\theta(\sin\theta)^{|\ell|+1}\sqrt{\cos\theta}\;\cos\theta_1\; T(\theta) d^{j}_{m,\sigma}(\theta_1) e^{i(\Phi(\theta)\,+\,k_1\cos\theta_1 z)\,-\,\gamma^2\sin^2\theta} \times \\ &\mathcal{W}_{m-\sigma-\ell}(\rho,\,\phi\,;\,\theta)\,, \end{aligned} \tag{B.32}$$

and

$$\begin{aligned} G^{\pm}_{jm} = &\int_0^{\theta_0} d\theta(\sin\theta)^{|\ell|+1}\sqrt{\cos\theta}\;\sin\theta_1\; T(\theta) d^{j}_{m\pm1,\sigma}(\theta_1) e^{i(\Phi(\theta)\,+\,k_1\cos\theta_1 z)-\gamma^2\sin^2\theta} \times \\ &\mathcal{W}_{m-\sigma-\ell}(\rho,\,\phi\,;\,\theta)\,, \end{aligned} \tag{B.33}$$

where the function $\mathcal{W}_M(\rho,\,\phi\,;\,\theta)$ is defined as:

$$\begin{aligned} \mathcal{W}_M(\rho,\,\phi\,;\,\theta) \;&=\; \sum_{p=-\infty}^{\infty} (-i)^p\; e^{-i\,2p\,(\phi_{\mathrm{ast}}-\phi)}\; J_{M-2p}(\xi)\, J_p(\mathcal{A}_{\mathrm{ast}}) \;= \\ J_M(\xi)\; J_0(\mathcal{A}_{\mathrm{ast}}) + &\sum_{p=1}^{\infty} J_p(\mathcal{A}_{\mathrm{ast}})\,(-i)^p \Big[\, e^{-i\,2p\,(\phi-\phi_{\mathrm{ast}})}\; J_{2p+M}(\xi) \;+\; e^{i\,2p\,(\phi-\phi_{\mathrm{ast}})}\; J_{-2p+M}(\xi) \,\Big]\,, \end{aligned} \tag{B.34}$$

remembering that $\xi = (k_1\,\rho\,\sin\theta_1)$ and

$$\mathcal{A}_{\text{ast}} = 2\pi\,A_{\text{ast}}\left(\frac{\sin\theta}{\sin\theta_0}\right)^2$$

Note that the difference between eqs. B.34 and B.28 is due to the fact that we are using the passive picture in the Debye potential formulation, *i.e.* we construct the fields so that the scattering sphere is always centered in the origin of the coordinate system [13] (only changing it back in the end of the MDSA theory derivation). This contrasts with the formulation of the Richards-Wolf fields, where the coordinates are the points in which we evaluate the field (which is centered at the origin).

When implementing infinite sums numerically, we must define a convergence criterion so the sum can be done over a finite number of terms. Indeed, as we substitute the Bessel function in the aberration-free expression with the sum in eqs. B.28, the computational cost associated with evaluating the field intensity distribution (and optical force) drastically increases. The arrangement of the series in eq. B.28 allows us to exploit the behavior of the Bessel functions relating their order n and argument z and obtain a truncated sum. First, we note that Bessel functions of increasingly larger order tend to remain close to zero for an increasing range of their argument (starting from zero). This can also be understood by analyzing the asymptotic behavior of Bessel functions for small arguments ($z \to 0$) [20]:

$$J_n(z) \sim \frac{(z/2)^n}{n!} \qquad \text{for } n \geq 0\,.$$

where Bessel functions with increasingly larger orders n will grow as a function of z with decreasing rate, according to the power law above.

However, this argument is not valid for larger arguments, meaning that a general rule must rely on a numerical evaluation of the Bessel functions in the series of eq. B.28. As a first attempt, the last term n_{last} of the truncated sum can be simply obtained by defining a tolerance value V_{tol} for which:

$$J_{n_{\text{last}}-1}(\mathcal{A}_{\text{ast}}) \;\geq\; V_{\text{tol}} \;>\; J_{n_{\text{last}}}(\mathcal{A}_{\text{ast}})\,.$$

Alternatively, we can incorporate the effect of the field amplitude profile and integrate $J_p(\mathcal{A}_{\rm ast})$ over θ along with the integrand of eq. B.29:

$$V_p^{(\ell,\,|m|)}(A_{\rm ast}) = (\sqrt{2}\,\gamma)^{|\ell|}\int_0^{\theta_0} d\theta\,(\sin\theta)^{1+|\ell|}\sqrt{\cos\theta}\,e^{-\gamma^2\sin^2\theta}\,T(\theta)\,e^{i\Phi(\theta)} \times f_{|m|}(\theta)\,J_p\Big(2\pi\,A_{\rm ast}\Big(\frac{\sin\theta}{\sin\theta_0}\Big)^2\Big)\,. \tag{B.35}$$

Finally, we can define a new tolerance using eq. B.35 as the quantity that should be minimized to assert convergence:

$$V_{n_{\rm last}-1}^{(\ell,\,|m|)}(A_{\rm ast}) \geq V_{\rm tol} > V_{n_{\rm last}}^{(\ell,\,|m|)}(A_{\rm ast})\,.$$

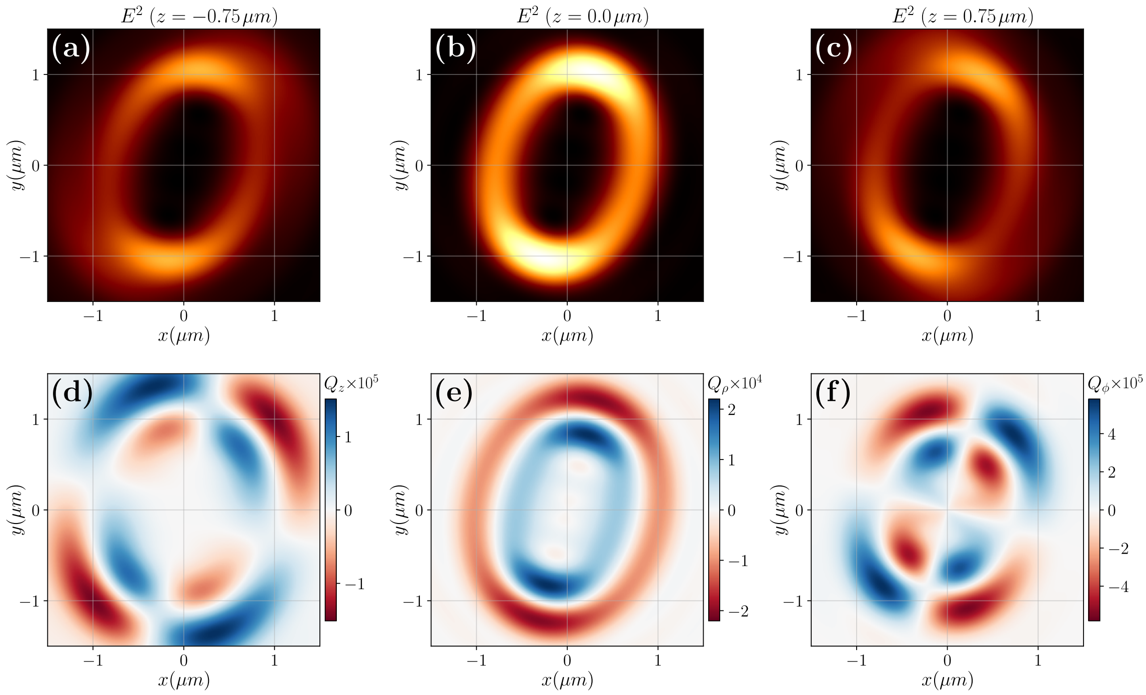

Figure B.2: Density plots of the intensity distribution for different $z-$planes (panels (a)-(c), with z values depicted on top) and the resulting force field exerted by a tightly focused vortex beam with astigmatism aberration (panels (d)-(f)) on a microsphere with radius $a = 0.05\mu$m. We consider a vortex beam with topological charge $\ell = 4$ and circular polarization state $\sigma = +1$, and the optical force is calculated at $z = 0$ in panels (d)-(f). The force field is represented in cylindrical coordinates, and follows the same orientation rules as in Fig. B.1.

In Fig. B.2 we show the numerical evaluation of the electric field intensity distribution (panels (a)-(c)), and the optical force components in cylindrical coordinates (panels (d)-

(f)). We consider a dipolar sphere, with radius $a = 0.05\mu$m, and an input vortex beam with topological charge $\ell = 4$ and left-circularly polarized ($\sigma = +1$). We plot the electric field intensity distribution for three $z-$planes: panel (a) depicts $z = -0.75\mu$m, panel (b) depicts $z = 0$ (corresponding to the circle of least confusion), and panel (c) depicts $z = 0.75\mu$m. The force components are evaluated at $z = 0$. The astigmatism aberration is characterized by two parameters: the aberration phase amplitude A_{ast} and the orientation angle ϕ_{ast}. We set those in Fig. B.2 as $2\pi\, A_{\text{ast}} = 1.0$ and $\phi_{\text{ast}} = 30°$.